DOT/FAA/TC-19/41, P1

Federal Aviation Administration
William J. Hughes Technical Center
Aviation Research Division
Atlantic City International Airport
New Jersey 08405

Aluminum 2024-T351 Input Parameters for *MAT_224 in LS-DYNA

March 2020

Final Report

This document is available to the U.S. public through the National Technical Information Services (NTIS), Springfield, Virginia 22161.

This document is also available from the Federal Aviation Administration William J. Hughes Technical Center at actlibrary.tc.faa.gov.

U.S. Department of Transportation
Federal Aviation Administration

NOTICE

Technical Report Documentation Page

1. Report No. DOT/FAA/TC-19/41, P1	2. Government Accession No.	3. Recipient's Catalog No.

4. Title and Subtitle

Aluminum 2024-T351 Input Parameters for *MAT_224 in LS-DYNA

5. Report Date

March 2020

6. Performing Organization Code

7. Author(s)

Chung-Kyu Park[1], Carney Kelly[1], Paul Du Bois[1], Cordasco Daniel[2], and Cing-Dao Kan[1]

8. Performing Organization Report No.

9. Performing Organization Name and Address

[1] George Mason University
Center for Collision Safety and Analysis
4087 University Drive, Fairfax, VA 22030 USA
[2] Federal Aviation Administration
William J. Hughes Technical Center
Atlantic City International Airport, NJ 08405

10. Work Unit No. (TRAIS)

11. Contract or Grant No.

13-G-020

12. Sponsoring Agency Name and Address

U.S. Department of Transportation
Federal Aviation Administration
Air Traffic Organization Operations Planning
Office of Aviation Research and Development
Washington, DC 20591

13. Type of Report and Period Covered

Final Report

14. Sponsoring Agency Code

AIR-6A1

15. Supplementary Notes

The FAA Aviation William J. Hughes Technical Center Research Division COR was William Emmerling.

16. Abstract

George Mason University, The Ohio State University, NASA Glenn Research Center, and the FAA Aircraft Catastrophic Failure Prevention Research Program have collaborated to develop a new material model in LS-DYNA® to support the FAA initiative of certification by analysis. The research was directed toward improving the numerical modeling of turbine engine blade-out containment tests required for certification of aircraft engines.

In this effort, the *MAT_224 constitutive material model was previously developed and released in LS-DYNA®. *MAT_224 is a general elasto-visco-plastic material model with arbitrary stress-versus-strain curves defining the plasticity, with arbitrary strain rate and temperature dependency. The element erosion criterion is the plastic failure strain, which can be defined as a function of the state of stress, strain rate, temperature, and element size.

The input parameters for a specific Aluminum 2024-T351 alloy sample were also determined and published. However, these *MAT_224 model input parameters did not produce accurate simulations of Al-2024-T351 ballistic impact tests. Subsequently, testing and analytical improvements made in the development of material models for titanium and Inconel® alloys had revealed limitations in the original aluminum mechanical test dataset. Improved measurement techniques in the material property tests have been developed, with new test specimens that provide additional calibration points on the failure surface. Therefore, the *MAT_224 input parameters for Aluminum 2024-T351 alloy have been redeveloped using the data from these enhanced mechanical property tests.

This report documents the updated *MAT_224 material model of the Aluminum 2024-T351 alloy and its validation using the ballistic impact tests and matching simulations. The efficiency of mesh regularization for normalizing results with varying mesh sizes, in ballistic impact simulations, was also investigated. In addition, several theoretical failure strain surfaces were compared with the tabular failure surface developed in this research.

17. Key Words Uncontained engine, Fan blade off, LS-DYNA, Turbine engine, Impact, Material model, Failure, Stress, Strain, Plasticity, Johnson-Cook, MAT_224, Triaxiality, Lode	18. Distribution Statement This document is available to the U.S. public through the National Technical Information Service (NTIS), Springfield, Virginia 22161. This document is also available from the Federal Aviation Administration William J. Hughes Technical Center at actlibrary.tc.faa.gov.

19. Security Classif. (of this report) Unclassified	20. Security Classif. (of this page) Unclassified	21. No. of Pages 92	22. Price

TABLE OF CONTENTS

APPENDICES

LIST OF FIGURES

LIST OF TABLES

LIST OF ACRONYMS

ACFPP	FAA Research Program: Aircraft Catastrophic Failure Prevention Program
AWG	Aerospace Working Group
DIC	Digital image correlation
FD	Force-displacement
GMU	George Mason University
GRC	Glenn Research Center
H-C	Hosford-Coulomb
IR	Infrared
LCK1	Rate dependent stress-strain curves/Table
LCKT	Temperature dependent stress-strain curves/Table
LCF	Triaxiality and lode parameter dependent failure surface/Table
LCH	Temperature scaling of the failure surface/Table
LCG	Strain rate scaling of the failure surface/Table
LCI	Mesh regularization curves/Table
OSU	Ohio State University
SHB	Split-Hopkinson bar
SS	Stress-strain
UCB	University of California at Berkeley

EXECUTIVE SUMMARY

George Mason University, The Ohio State University, NASA Glenn Research Center, and the FAA Aircraft Catastrophic Failure Prevention Research Program have collaborated to develop a new material model in LS-DYNA® to support the FAA initiative of certification by analysis. The research was directed toward improving the numerical modeling of turbine engine blade-out containment tests required for certification of aircraft engines.

In this effort, the *MAT_224 constitutive material model was previously developed and released in LS-DYNA®. *MAT_224 is a general elasto-visco-plastic material model with arbitrary stress versus strain curves defining the plasticity, with arbitrary strain rate and temperature dependency. The element erosion criterion is the plastic failure strain, which can be defined as a function of the state of stress, strain rate, temperature, and element size.

The input parameters for a specific Aluminum 2024-T351 alloy sample were also determined and published. However, these *MAT_224 model input parameters did not produce accurate simulations of Al-2024-T351 ballistic impact tests. Subsequently, testing and analytical improvements made in the development of material models for titanium and Inconel® alloys had revealed limitations in the original aluminum mechanical test dataset. Improved measurement techniques in the material property tests have been developed, with new test specimens that provide additional calibration points on the failure surface. Therefore, the *MAT_224 input parameters for Aluminum 2024-T351 alloy have been redeveloped using the data from these enhanced mechanical property tests.

This report documents the updated *MAT_224 material model of the Aluminum 2024-T351 alloy and its validation using the ballistic impact tests and matching simulations. The efficiency of mesh regularization for normalizing results with varying mesh sizes, in ballistic impact simulations, was also investigated. In addition, several theoretical failure strain surfaces were compared with the tabular failure surface developed in this research.

1. INTRODUCTION

A team consisting of George Mason University (GMU), Ohio State University (OSU), George Washington University, the National Aeronautics and Space Administration (NASA) - Glenn Research Center (GRC), and the FAA Aircraft Catastrophic Failure Prevention Research Program (ACFPP) has collaborated to develop a new material model in LS-DYNA® for an Aluminum 2024-T351 alloy. The research was directed toward improving the numerical modeling of turbine engine blade-out containment tests required for certification of aircraft engines [1].

In 2007, Lawrence Livermore National Laboratory reported an extensive exercise using the popular Johnson-Cook material model (*MAT_015 in LS-DYNA), in which attempts were made to accurately predict multiple failure modes [2]. Multiple failure modes can exist in engine fragment impact events, which can occur depending on the thickness of the impacted structure and the fragment characteristics [3]. It was shown that the *MAT_015 input parameters could be tuned so that the analysis could be made to match the results from a series of ballistic impact tests using the same thickness. This same set of input parameters would produce poor matches for simulations of the other thickness plates. In figure 1, the results from tuning the *MAT_015 input parameters to match the 0.125-inch thickness plate impact results are presented. At that time, the LS-DYNA Aerospace Working Group (AWG) agreed that a new constitutive material model would be required to predict multiple failure modes using a single set of input parameters, and work to develop *MAT_224 began.

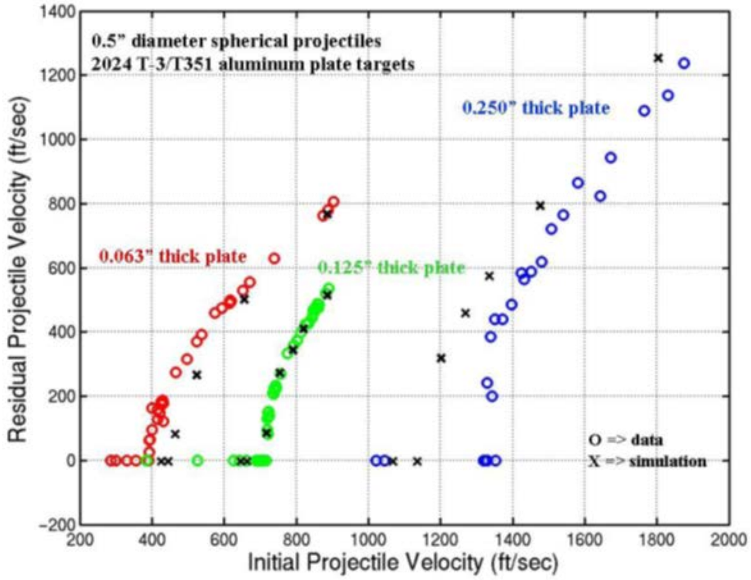

Figure 1. Aluminum 2024 results for *MAT_015 [1]

The LS-DYNA constitutive material model *MAT_TABULATED_JOHNSON_COOK, or simply *MAT_224, was developed and has been previously presented [4, 5]. *MAT_224 is an elasto-visco-plastic material with arbitrary stress versus strain curves defining the plasticity and with arbitrary strain rate and temperature dependency. Adiabatic heating due to plastic work can cause temperatures to increase and the material to soften. Element erosion is included using plastic failure strain as a criterion and can be defined as a function of the state of stress, the strain rate, the temperature, and the element size. This material model resembles the original Johnson-Cook material (*MAT_015) using similar separation of parameter dependencies, but with the possibility of general tabulated input parameters. The tabulated input parameters allow for a much closer match to mechanical property test data than the Johnson-Cook model, which is limited by curve fitting of the test data.

The original Aluminum 2024 alloy *MAT_224 input parameters were developed previously and released to the LS-DYNA AWG. This material model was based on tabulated data from several material tests performed by OSU [4, 6]. However, the original model did not produce simulations that accurately matched the ballistic impact tests. In addition, continuing research to develop material models of titanium and Inconel® alloys has revealed deficiencies in the original aluminum mechanical test data. Improved measurement techniques in material tests have since been developed, with new test methods that provide additional model calibration points on the failure surface [7–13].

Considering the inaccuracy of the original model, and the improvements and new findings from the OSU testing, the Aluminum 2024-T351 *MAT_224 material model has been redeveloped by GMU. This report describes the updated Aluminum 2024 *MAT224 input parameters, the method used to create them, and the validation that used ballistic impact simulations.

This research was conducted under FAA grant 13-G-020 and sponsored by the ACFPP.

2. BACKGROUND

The *MAT_224 is the isotropic elasto-thermo-visco-plastic constitutive material model. Table 1 describes the input parameters of *MAT_224.

Table 1. Input parameters of *MAT_224 and their description [5]

Column	1	2	3	4	5	6	7	8
Card1	MID	RO	E	PR	CP	TR	BETA	
Card2	LCK1	LCKT	LCF	LCG	LCH	LCI		

MID: Material identification
RO: Mass density
E: Young’s modulus
PR: Poisson’s ratio
CP: Specific heat
TR: Room temperature
BETA: Fraction of plastic work converted into heat, Taylor–Quinney coefficient
LCK1: Table ID defines for each plastic strain rate value a load curve ID giving the (isothermal) effective stress versus effective plastic strain for that rate
LCKT: Table ID defining for each temperature value a load curve ID giving the (quasi-static) effective stress versus effective plastic strain for that temperature
LCF: Table ID defines for each Lode parameter a load curve ID giving the plastic failure strain versus triaxiality for that Lode parameter
LCG: Load curve ID defining plastic failure strain (or scale factor) as a function of plastic strain rate. If the first abscissa value in the curve corresponds to a negative strain rate, LS-DYNA assumes that the natural logarithm of the strain rate value is used for all abscissa values
LCH: Load curve ID defining plastic failure strain (or scale factor) as a function of temperature
LCI: Table ID defines for each triaxiality a load curve ID giving the plastic failure strain versus element size for that triaxiality. If a three-dimensional table ID is referred, plastic failure strain can be a function of Lode parameter (TABLE_3D), triaxiality (TABLE), and element size (CURVE)

LCK1 = Rate dependent stress-strain curves/Table, LCKT = Temperature dependent stress-strain curves/Table, LCF = Triaxiality and lode parameter dependent failure surface/Table, LCH = Temperature scaling of the failure surface/Table, LCG = Strain rate scaling of the failure surface/Table, LCI = Mesh regularization curves/Table

A general form of the hypo-elastic relation is given by:

$$\boldsymbol{\sigma}^{\nabla} = \boldsymbol{f}(\boldsymbol{\sigma}, \boldsymbol{D}), \tag{1}$$

where $\boldsymbol{\sigma}^{\nabla}$ represents any objective rate of the Cauchy stress, $\boldsymbol{\sigma}$, and $\boldsymbol{D}$ is the rate of deformation. The stress is expressed as:

$$\boldsymbol{\sigma} = \boldsymbol{s}(\boldsymbol{\varepsilon}, \dot{\boldsymbol{\varepsilon}}, T), \tag{2}$$

where $\boldsymbol{\varepsilon}$ is the strain, $\dot{\boldsymbol{\varepsilon}}$ is the strain rate, T is the temperature. The Jaumann rate of the Cauchy stress is:

$$\boldsymbol{\sigma}^{\nabla \mathrm{J}} = \boldsymbol{C}^{\sigma J} : \boldsymbol{D}, \tag{3}$$

where the Jaumann rate elastic moduli $\boldsymbol{C}^{\sigma J}$ is expressed as:

$$\boldsymbol{C}^{\sigma J} = \lambda \boldsymbol{I} \otimes \boldsymbol{I} + 2\mu \boldsymbol{I}, \qquad (4)0$$

where λ and μ are the Lamé constants, and $\boldsymbol{I}$ is the unit tensor. The Young's modulus E and the Poisson's ratio ν are converted by:

$$E = \frac{\mu(3\lambda+2\mu)}{\lambda+\mu}, \text{ and } \nu = \frac{\lambda}{2(\lambda+\mu)} . \tag{5}$$

The flow stress σ_y in the plastic region is expressed as:

$$\sigma_y = k_1(\varepsilon_p, \dot{\varepsilon}_p) \frac{k_t(\varepsilon_p,T)}{k_t(\varepsilon_p,T_R)} , \tag{6}$$

where $k_1(\varepsilon_p, \dot{\varepsilon}_p)$ is the rate-dependent hardening curves (defined as LCK1 in *MAT_224), $k_t(\varepsilon_p, T)$ is the temperature-dependent hardening curves (defined as LCKT in *MAT_224), ε_p is the plastic strain, $\dot{\varepsilon}_p$ is the plastic strain rate, T is the temperature, and T_R is the room temperature.

The plastic failure strain is defined as:

$$\varepsilon_p^f = f(\sigma^*, L)\; g(\dot{\varepsilon}_p)\; h(T)\; i(l_c, \sigma^*, L), \tag{7}$$

where $f(\sigma^*, L)$ is the plastic failure function (defined as LCF in *MAT_224) in the triaxiality (σ^*) and Lode parameter (L), $g(\dot{\varepsilon}_p)$ is the rate-dependent scale curve (defined as LCG in *MAT_224), $h(T)$ is the temperature-dependent scale curve (defined as LCH in *MAT_224), and $i(l_c, \sigma^*, L)$ is the element size-dependent scale function (defined as LCI in *MAT_224) in the triaxiality (σ^*) and Lode parameter (L) where l_c is the initial element size, so-called characteristic length of an element. The triaxiality (σ^*) is defined as:

$$\sigma^* = \sigma_m/\sigma_{VM}, \tag{8}$$

where σ_m is the hydrostatic stress and σ_{VM} is the Von Mises stress. The Lode parameter (L) is defined as:

$$L = 27J_3/2\sigma_{VM}^3, \tag{9}$$

where J_3 is the third invariant of deviatoric stress. Additional details on the definition and characteristics of the triaxiality and Lode parameter are given in reference [4].

Temperature increase as a result of plastic work is calculated by:

$$T = T_R + \frac{\beta}{C_p\rho} \int \sigma_y\, \dot{\varepsilon}_p dt, \tag{10}$$

where β is the percentage of plastic work converted into heat energy (the Taylor-Quinney coefficient), C_p is the specific heat, and ρ is the density.

The original *MAT_224 Aluminum 2024-T351 alloy material model was developed [1, 4, 6] and released in 2014. Subsequently, it was used to simulate various ballistic impact tests in which its limitations were revealed. For example, the original Al-2024 material model was used to predict the ballistic limit velocity of spherical projectiles impacting Aluminum 2024-T351 plates with varying thicknesses. Figure 2 shows the exit velocities of the spherical projectiles, which impact Al-2024 alloy plates of three different thicknesses. The corresponding simulation results, using the original *MAT_224 input parameters, are also shown in figure 2. The ballistic limit velocities of the spherical projectile were overpredicted in the impact simulations with the 0.063-inch and 0.125-inch thickness aluminum plates, but the simulation underpredicted the ballistic limit of the 0.25-inch thickness aluminum plates. Such simulation results demonstrated that the original *MAT_224 Aluminum 2024-T351 input parameters were limited in their ability to accurately predict ballistic limit velocities over a range of plate thicknesses.

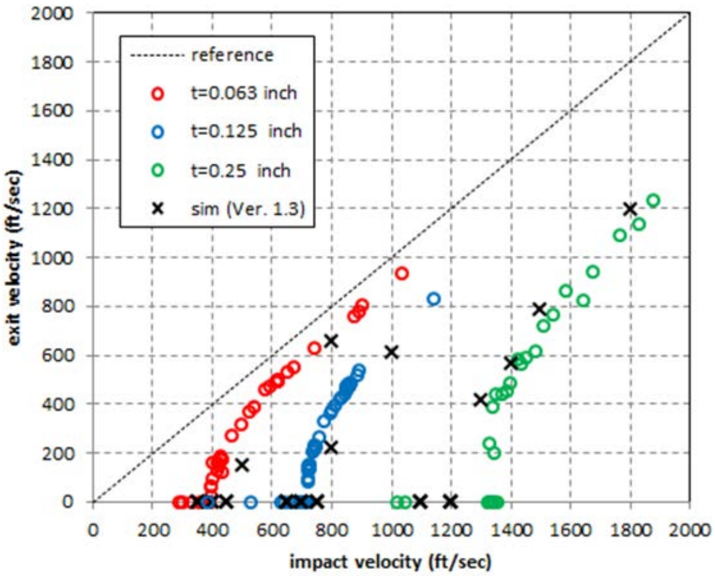

Figure 2. Ballistic impact test exit velocities with a spherical projectile impacting three different thickness plates of Al 2024-T351 and the corresponding simulation results using the original *MAT_224 Aluminum 2024 material model

There have been continuing research projects to develop new material models of a titanium Ti-6Al-4V alloy and an Inconel 718 alloy [7–13]. These research activities revealed sources of the limitations in the original Aluminum 2024-T351 input parameters. The sources of these limitations have been mitigated by advancements in testing, which were developed and implemented at OSU. The improved datasets proved to have a significant advantage over the original data, by providing full-field strains from Digital Image Correlation (DIC) test data. The full-field strains allowed for direct comparisons of the test results to the LS-DYNA simulations. The DIC test data also allowed a precise determination of the strain rate occurring in the necking region of the sample. In addition, the boundary condition assumptions in the high-rate split-Hopkinson bar (SHB) tests proved to be incorrect, and the DIC data were used to correct these boundary conditions, allowing for more accurate force-displacement (FD) comparisons between test and simulation. Testing was further improved by adding infrared (IR) imagery to capture the temperature change during failure. Finally, new test designs were developed to add additional test points to the failure surface in regions where impact failures occur.

The new test designs were needed for accurate ballistic limit-velocity predictions, because the failure surface (LCF) had been approximated from limited material test failure strains. Figure 3 shows the material test failure strains used to develop the LCF of the original material model. In the sphere impact simulations, the initial failure of the plate occurred at a state of stress in which the Lode parameter was negative. In figure 3, it can be seen that there were only three failure strain test points available with negative Lode parameters.

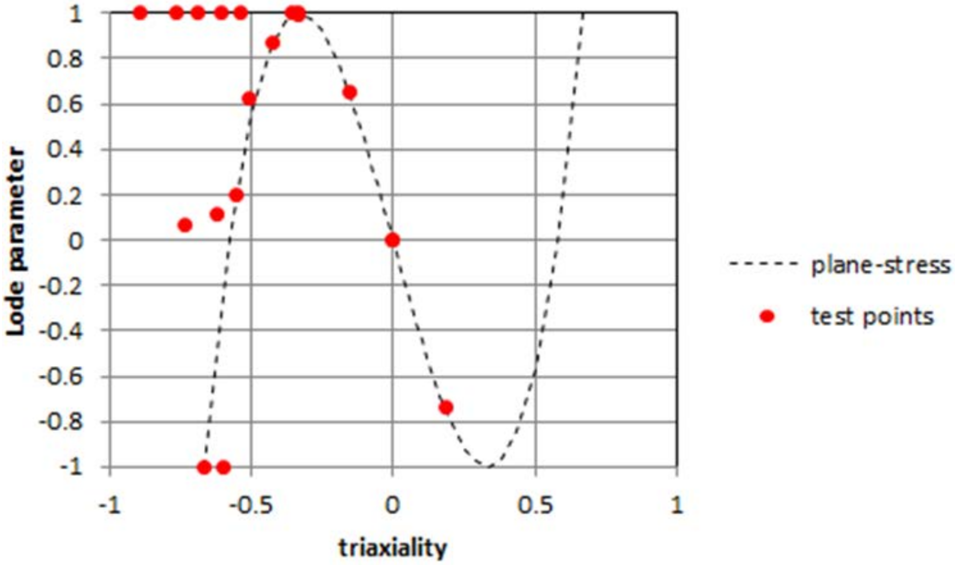

Figure 3. Failure test points for LCF in the original material model of *MAT_224

The two test points with both negative triaxiality and negative Lode parameter were obtained from previous punch test designs. The original punch tests were difficult to simulate accurately because of the grip slipping at the boundary. In addition, the state of stress varied considerably, and so these tests could not provide an accurate failure strain at a particular state of stress. Therefore, three new punch tests were designed by using a smaller punch and attaching a ductile copper backing plate behind the aluminum plate [12]. In addition, a new combined loading material test was conducted to add an additional test point in the area that the Lode parameter is negative and the triaxiality is positive.

The continuing research to develop the titanium and Inconel models also demonstrated that the strain rate was not constant over the specimen, especially in the high-rate tests. Strain rate is not constant because of localization after necking, which increases the strain rate in the necking area. The actual strain rate in the necking area of the specimen is much higher than the nominal overall rate. The actual strain rate must be measured using DIC of the localization area. In addition, ballistic impact analysis showed that the strain rate in a local region of an impacted plate could reach more than 25,000/sec, which is far beyond the highest range of high-strain rate material tests. Therefore, additional higher strain rate tests were conducted and extrapolated to cover the highest rates observed in the impact analysis, resulting in new LCK1 and LCG input curves.

Initially, it was assumed that the plastic deformation at the relatively low rate of 1/sec takes place in a nearly isothermal condition because the generated heat from the plastic deformation would have time to conduct into its surroundings. However, even at this low rate there is some increase in temperature in the necking region. When the strain rate is higher, there is significant increase in temperature because there is not enough time for the created heat to dissipate. Furthermore, plastic heating approaches a near adiabatic condition at sufficiently high strain rates. The temperature increase caused by plastic work is calculated by equation 10, where the Taylor-Quinney coefficient, β, is a material property. The IR imagery was used to accurately measure the temperature increase during material tensile tests [13]. Based on this data, a revised β was calculated.

The list of the work performed in the updating of the original material model is:

- Added two higher strain rate tensile tests (Revised LCK1, LCG)
- Added three new punch tests (Revised LCF)
- Added one combined-loading material test (Revised LCF)
- Recalculated the β coefficient by using the IR camera (Revised LCKT, which interacts with revised LCK1)
- Recalculated the strain rates by using DIC (Revised LCK1)
- Revised regularization based on element size and state of stress (Revised LCI).

3. TEST SERIES OF ALUMINUM 2024 ALLOY

3.1 MATERIAL TESTS

OSU conducted a large number of material tests to develop the Aluminum 2024-T351 alloy material dataset. The material tests were conducted with various strain rates, temperatures, specimen geometries, and loading conditions. The details of all the material tests are described in reference [6]. A brief summary of the material tests is described in this section.

All material test series are summarized in tables 2–9.

The test specimen geometries are shown in figure 4. The detail dimensions of the test specimens and their test conditions are described in the reference [6]. There are newly added tests indicated by the asterisk (*), which were not listed in the reference [6].

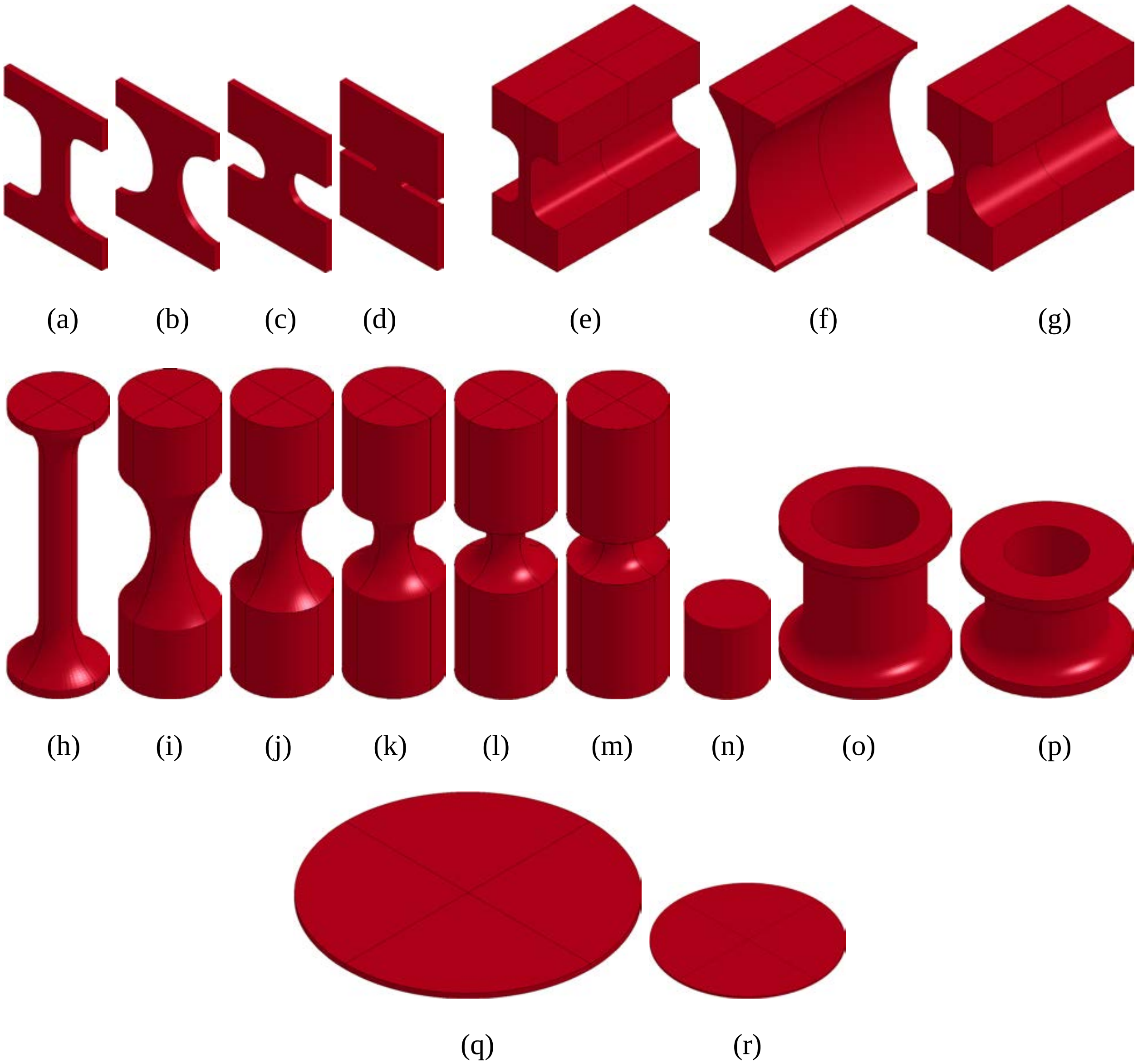

Figure 4. Specimen geometries of material tests: (a) flat dogbone (SG1), (b) 2D large notch (SG2), (c) 2D intermediate notch (SG3), (d) 2D small notch (SG4), (e) thick dogbone (SG11), (f) thick large notch (SG12), (g) thick small notch (SG13), (h) axisymmetric smooth (SG5), (i) axisymmetric notch #1 (SG6), (j) axisymmetric notch #2 (SG7), (k) axisymmetric notch #3 (SG8), (l) axisymmetric notch #4 (SG9), (m) axisymmetric notch #5 (SG10), (n) cylinder, (o) spool #1, (p) spool #2, (q) large circular plate, (r) small circular plate.

Table 2 lists the five temperature tensile tests, which were conducted at five different temperatures:

- T1: Room Temperature (RT)
- T2: 150 ˚C
- T3: 300 ˚C
- T4: 450 ˚C
- T5: -50 ˚C

Those tests were conducted to develop the curves of LCKT and LCH of *MAT_224.

Table 2. Temperature test series

Test #	Test Mode	Apparatus	Specimen Geometry	Strain Rate (1/sec)	Temperature (˚C)
M1-TMT-P3-SG1-O1-SR3-T1-N#	Tension	Instron	Flat Dogbone	SR3:1.0E+0	T1:RT
M1-TMT-P3-SG1-O1-SR3-T2-N#					T2:150
M1-TMT-P3-SG1-O1-SR3-T3-N#					T3:300
M1-TMT-P3-SG1-O1-SR3-T4-N#					T4:450
M1-TMT-P3-SG1-O1-SR3-T5-N#					T5:-50

Tables 3 and 4 list the tension and compression rate tests. The lower rate tests at and below 1.0/sec were conducted by an Instron machine and the higher rate tests over 1.0/sec were conducted using a SHB apparatus. They were conducted at seven different rates in tension and eight different rates in compression:

- SR1: 1.0E-4/sec (tension) | 1.0E-4/sec (compression),
- SR2: 1.0E-2/sec (tension) | 1.0E-2/sec (compression),
- SR3: 1.0E+0/sec (tension) | 1.0E+0/sec (compression),
- SR4: 5.0E+2/sec (tension) | 5.0E+2/sec (compression),
- SR5: 2.0E+3/sec (tension) | 5.0E+3/sec (compression),
- SR6: 5.0E+3/sec (tension) | 7.5E+3/sec (compression),
- SR7: 7.0E+3/sec (tension) | 9.0E+3/sec (compression), and
- SR8: N/A | 1.0E+4/sec (compression).

Recall that in tension, the strain rate is not constant due to localization, and the presented nominal strain rates are used for classification. In the tension rate series, two very high rate tests were added. Those tests were conducted to develop the table and curves of LCK1 and LCG of *MAT_224.

Table 3. Rate test series—tension

Test # (* newly added test)	Test Mode	Apparatus	Specimen Geometry	Strain Rate (1/sec)	Temperature (˚C)
M1-TMT-P3-SG1-O1-SR1-T1-N#	Tension	Instron	Flat Dogbone	SR1:1.0E-4	T1:RT
M1-TMT-P3-SG1-O1-SR2-T1-N#				SR2:1.0E-2	
M1-TMT-P3-SG1-O1-SR3-T1-N#				SR3:1.0E+0	
M1-TMT-P3-SG1-O1-SR4-T1-N#		SHB		SR4:5.0E+2	
M1-TMT-P3-SG1-O1-SR5-T1-N#				SR5:2.0E+3	
*M1-TMT-P3-SG1-O1-SR6-T1-N#				SR6:5.0E+3	
*M1-TMT-P3-SG1-O1-SR7-T1-N#				SR7:7.0E+3	

Table 4. Rate test series—compression

Test #	Test Mode	Apparatus	Specimen Geometry	Strain Rate (1/sec)	Temperature (˚C)
M1-TMC-P3-SG1-O1-SR1-T1-N#	Compression	Instron	Cylinder	SR1:1.0E-4	T1:RT
M1-TMC-P3-SG1-O1-SR2-T1-N#				SR2:1.0E-2	
M1-TMC-P3-SG1-O1-SR3-T1-N#				SR3:1.0E+0	
M1-TMC-P3-SG1-O1-SR4-T1-N#		SHB		SR4:5.0E+2	
M1-TMC-P3-SG1-O1-SR5-T1-N#				SR5:5.0E+3	
M1-TMC-P3-SG1-O1-SR6-T1-N#				SR6:7.5E+3	
M1-TMC-P3-SG1-O1-SR7-T1-N#				SR7:9.0E+3	
M1-TMC-P3-SG1-O1-SR8-T1-N#				SR8:1.0E+4	

Tables 5–9 list the failure tests and their test conditions. There are five failure test series that identify failure strains at different states of stress. The different states of stress are achieved by using different specimen geometries, as shown in figure 4, and differing applied loads. Those tests were used to develop the *MAT_224 LCF table. The five failure test series are:

- Plane stress series
- Axisymmetric series
- Plane strain series
- Combined loading series
- Punch series (new)

The punch series described in table 9 are new designs and different from the punch tests described in the previous study. The previous punch tests were difficult to simulate accurately because the grips slipped at the boundary. Therefore, new punch tests were developed with smaller punches to remove boundary effects. In two of the new punch test configurations, a copper backing plate was placed behind the Al-2024 plate being tested to induce the particular states of stress desired [12]. The new punch test series is described in appendix A.

Table 5. Failure test series—plane stress

Test #	Test Mode	Apparatus	Specimen Geometry	Strain Rate (1/sec)	Temperature (˚C)
M1-TMT-P3-SG1-O1-SR3-T1-N#	Tension	Instron	Flat Dogbone	SR3:1.0E+0	T1:RT
M1-TMT-P3-SG2-O1-SR3-T1-N#			2D Large Notch		
M1-TMT-P3-SG3-O1-SR3-T1-N#			2D Intermediate Notch		
M1-TMT-P3-SG4-O1-SR3-T1-N#			2D Small Notch		

Table 6. Failure test series—axisymmetric

Test #	Test Mode	Apparatus	Specimen Geometry	Strain Rate (1/sec)	Temperature (˚C)
M1-TMT-P3-SG5-O1-SR3-T1-N#	Tension	Instron	Axisymmetric Smooth	SR3:1.0E+0	T1:RT
M1-TMT-P3-SG6-O1-SR3-T1-N#			Axisymmetric Notch #1		
M1-TMT-P3-SG7-O1-SR3-T1-N#			Axisymmetric Notch #2		
M1-TMT-P3-SG8-O1-SR3-T1-N#			Axisymmetric Notch #3		
M1-TMT-P3-SG9-O1-SR3-T1-N#			Axisymmetric Notch #4		
M1-TMT-P3-SG10-O1-SR3-T1-N#			Axisymmetric Notch #5		

Table 7. Failure test series—plane strain

Test #	Test Mode	Apparatus	Specimen Geometry	Strain Rate (1/sec)	Temperature (˚C)
M1-TMT-P3-SG11-O1-SR3-T1-N#	Tension	Instron	Thick Dogbone	SR3:1.0E+0	T1:RT
M1-TMT-P3-SG12-O1-SR3-T1-N#			Thick Large Notch		
M1-TMT-P3-SG13-O1-SR3-T1-N#			Thick Small Notch		

Table 8. Failure test series—combined loading

Test # (* newly added test)	Test Mode	Apparatus	Specimen Geometry	Strain Rate (1/sec)	Temperature (˚C)
M1-TMCL-LR1-P3-SR3-T1-N#	Tension + Torsion	Instron	Spool #1	SR3:1.0E+0	T1:RT
M1-TMCL-LR2-P3-SR3-T1-N#	Tension + Torsion				
M1-TMCL-LR3-P3-SR3-T1-N#	Pure Torsion				
M1-TMCL-LR4-P3-SR3-T1-N#	Compression + Torsion		Spool #2		
*M1-TMCL-LR5-P3-SR3-T1-N#	Compression + Torsion				

Table 9. Failure test series—punch (new)

Test # (* newly added test)	Test Mode	Apparatus	Specimen Geometry	Strain Rate (1/sec)	Temperature (˚C)
*M1-TMP7-P3-SR2-T1-N#	Punch #7 (unbacked)	Instron	Large Circular Plate	SR2:1.0E-2	T1:RT
*M1-TMP8-P3-SR2-T1-N#	Punch #8 (thin-backed)		Small Circular Plate		
*M1-TMP9-P3-SR2-T1-N#	Punch #9 (thick-backed)				

3.1.1 Validation tests

Two separate series of ballistic impact tests using Aluminum 2024 alloy plates were conducted by the University of California at Berkeley (UCB) [14] and the NASA-GRC [15]. Those test results were used for the validation of the updated *MAT_224 Aluminum 2024-T351 input parameters.

*In the ballistic impact tests conducted by UCB [14], 12-by-12-inch square Aluminum 2024 alloy plates with three different thicknesses (0.063 inch, 0.125 inch, and 0.25 inch) were impacted by a 0.5-inch diameter chrome steel sphere projectile with various initial impact speeds. In the ballistic impact tests conducted by NASA-GRC [15], 10-inch diameter circular Aluminum 2024 alloy plates of three different thicknesses (0.125 inch, 0.25 inch, and 0.5 inch) were impacted by 0.5-inch diameter titanium or steel cylinder projectiles with various initial impact speeds. The results of ballistic impact tests are shown in figure 5.

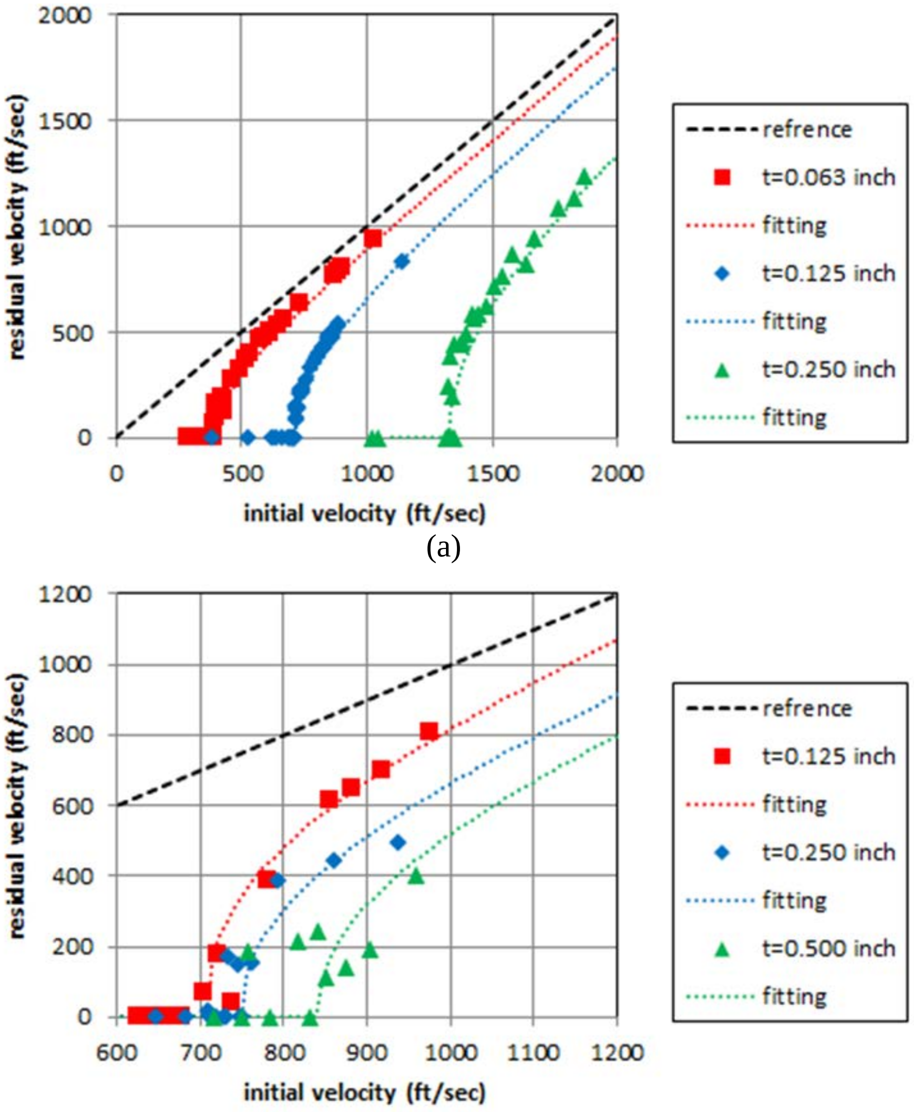

(a)

(b)

Figure 5. Results of ballistic impact tests: (a) sphere impact test [14] and (b) cylinder impact test [15]

The fitting lines through the data points were determined based on a generalization of an analytical model originally proposed by Recht and Ipson [16]. The equation of residual velocities is expressed as:

$$v_r = a({v_i}^p - {v_{bl}}^p)^{1/p}, \tag{11}$$

where v_r is the residual (or exit) velocity, v_i is the initial velocity, v_{bl} is the ballistic limit velocity, and a and p are the empirical constants [17]. With a spherical projectile, the empirical constants are defined as:

$$a = \sqrt{\frac{1}{1+\frac{3\rho_t H}{2\rho_p D}}} \text{ and } p = 2, \quad (12)$$

where ρ_t and ρ_p are the density of the plate and projectile respectively, H is the thickness of the plate, and D is the diameter of the projectile [18]. With a blunt-nosed cylinder projectile, the empirical constants can be obtained from the test data by using the method of least squares. The ballistic limit velocities were identified from the test results. Table 10 summarizes the ballistic limit velocities and fitting parameters of equation 11.

Table 10. Summary of ballistic limit velocities and fitting parameters of equation 11

	Plate thickness (inch)	Ballistic limit velocity (v_{bl}) (ft/sec)	a	p
Sphere impact test	0.063	391.0	0.97	2.00
	0.125	717.0	0.94	2.00
	0.25	1327.0	0.89	2.00
Cylinder impact test	0.125	710.0	1.00	2.60
	0.25	750.0	0.92	2.26
	0.5	840.0	0.89	2.15

4. DEVELOPMENT OF THE UPDATED *MAT_224 ALUMINUM 2024 INPUT PARAMETERS

Table 11 shows the updated *MAT_224 input parameters for the Aluminum 2024 alloy. Its basic input parameters, such as density, Young's modulus, Poisson's ratio, and specific heat, used the same property values as in the original material model. The coefficients are presented in SI units, which are millimeter, second, ton, Newton, and Kelvin. Imperial, or English units, are also included. The other input parameters, such as Beta, and the LCK1, LCKT, LCF, LCG, LCH and LCI tables, have been updated in this research work. The updates will be described in this section. The detailed process on how to develop the *MAT_224 input parameters (especially, the material curves) from material tests using iterative reverse engineering is described in reference [7].

Table 11. Basic input parameters of *MAT_224 of Aluminum 2024 alloy

Parameters	SI units		Imperial units	
RO:	2.6E-9	ton/mm^3	0.0002432	lbf-sec^2/in^4
E:	70,000.0	MPa	10,152,689	Psi
PR:	0.33		0.33	
CP:	9.0E+8	kJoules/ton-Kelvin	776,348	BTU/(lbf-sec^2/in-Rankine)
TR:	300.0	Kelvin	540.0	Rankine
BETA:	0.4 (updated)			
LCK1:	Table (updated)			
LCKT:	Table (updated)			
LCF:	Table (updated)			
LCG:	Curve (updated)			
LCH:	Curve (updated)			
LCI:	Table (updated)			

4.1 UPDATE OF THE QUASI-STATIC STRESS-STRAIN CURVE FOR LCK1

The quasi-static curve in LCK1 was developed from tensile tests of flat dogbone specimens (SG1) at quasi-static strain rates (SR1 and SR2) and room temperature (T1), and are listed in table 3. The process of developing the input curve for *MAT_224 from the tensile tests is described in appendix B.

Figure 6 shows the FD curves of material tensile tests with the SG1 specimen and quasi-static strain rates (SR1 and SR2) and room temperature (T1). The input stress-strain (SS) curve, developed using the iterative reverse-engineering process described in appendix B, is shown in figure 7. Figure 6 shows that the FD curve from the simulation, using the input SS curve, closely matches the test curves.

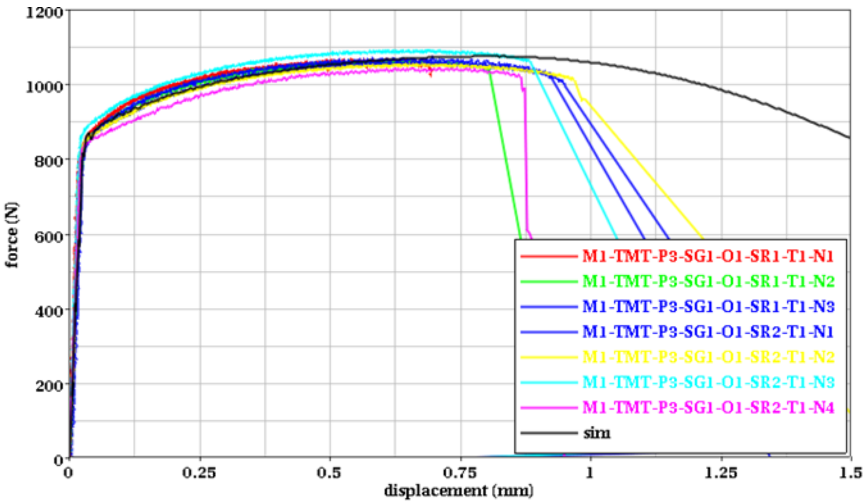

Figure 6. FD plot of material tensile tests with SG1 specimen at quasi-static rate (SR1 and SR2) and room temperature (T1)

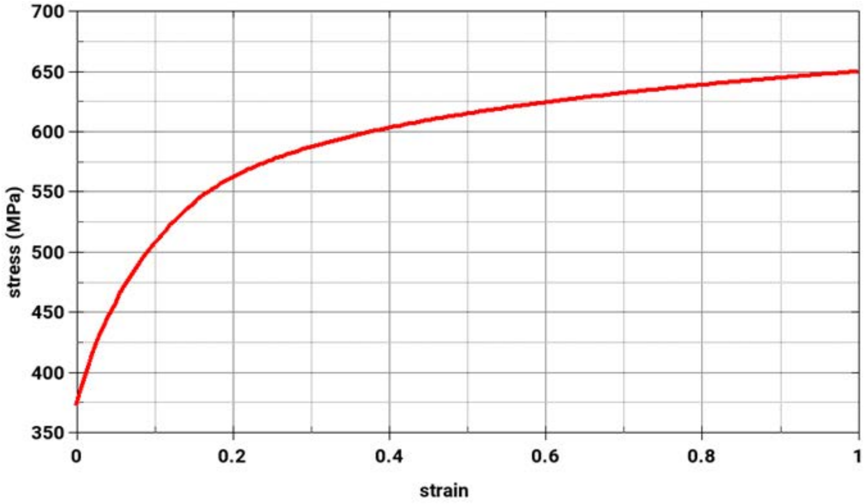

Figure 7. Quasi-static SS curve of LCK1 of *MAT_224

4.2 UPDATE OF TEMPERATURE DEPENDENT SS CURVES (LCKT)

The FD curves of the tensile tests of the temperature series in table 2 are shown in figure 8. The tensile tests were conducted with the flat dogbone specimen (SG1) at the SR3 strain rate using five different temperatures: room temperature (T1), 150˚ C (T2), 300˚ C (T3), 450˚ C (T4), and -50˚ C (T5). The SS input curves were developed by the iterative reverse-engineering described in appendix B. The FD curve results from the tensile simulations, using the developed SS input curves, are also shown in figure 8. The simulation results closely match the test curves.

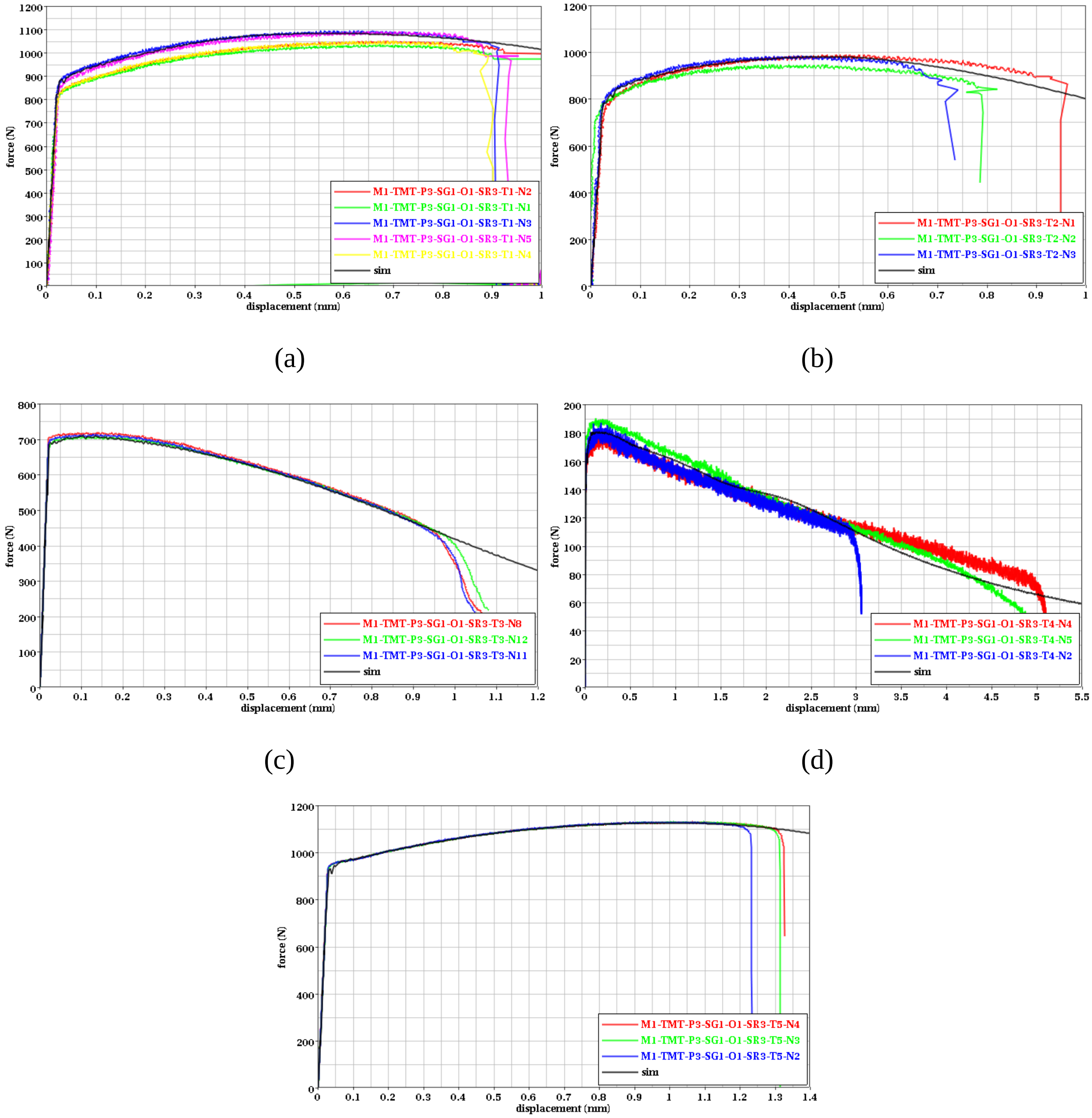

(a)

(b)

(c)

(d)

(e)

Figure 8. FD plots of material tensile tests with SG1 specimen at the SR3 rate and at five different temperatures: (a) T1, (b) T2, (c) T3, (d), T4, and (e) T5

Tensile tests that attempt to establish the behavior of alloys at varying temperatures should be conducted at a slow enough rate that any generated heat from plastic work has a chance to diffuse and so remain isothermal. It had been thought that SR3 (1.0/sec) was slow enough to create an isothermal test, but it was discovered that this was not the case; some temperature localization was occurring. Figure 9 compares the SS input curves developed in the quasi-static condition (shown in figure 7) and in the SR3 rate condition under room temperature. There is a slight difference between the two curves, and this difference is caused by the temperature localization. The difference can be used to quantify the effect of the localization. Therefore, the isothermal SS input curves for the LCKT table were created by scaling, using a function expressed as:

$$\sigma_y^{LCKT}(\varepsilon_p, \mathbf{SR1}, T) = \sigma_y^{LCKT}(\varepsilon_p, \mathbf{SR3}, T)\,\frac{\sigma_y^{LCK1}(\varepsilon_p, \mathbf{SR1}, \mathbf{T1})}{\sigma_y^{LCKT}(\varepsilon_p, \mathbf{SR3}, \mathbf{T1})}. \tag{13}$$

The resulting scaled SS curves of LCKT are shown in figure 10. As the high rate tests are not isothermal, these curves must be completed before the analysis of the high-strain rate tests begins. Otherwise, the behavior due to the temperature increase will not be calculated correctly.

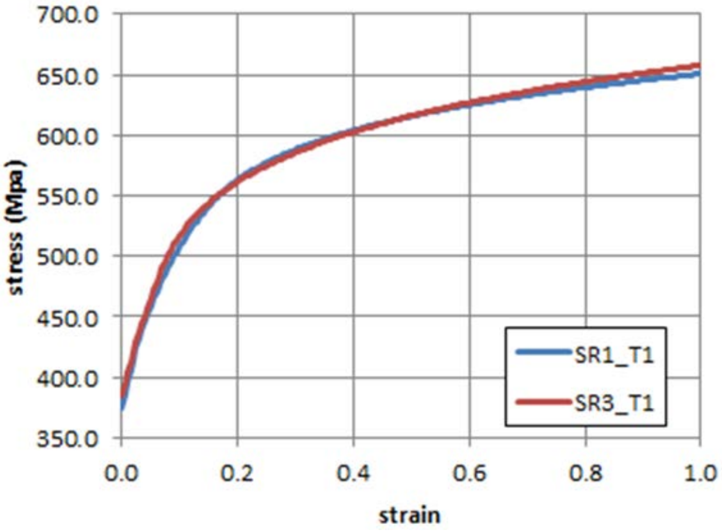

Figure 9. Comparison of quasi-static SS curve (SR1_T1) in LCK1 and SS curve (SR3_T1) in SR3 rate and in room temperature (T1)

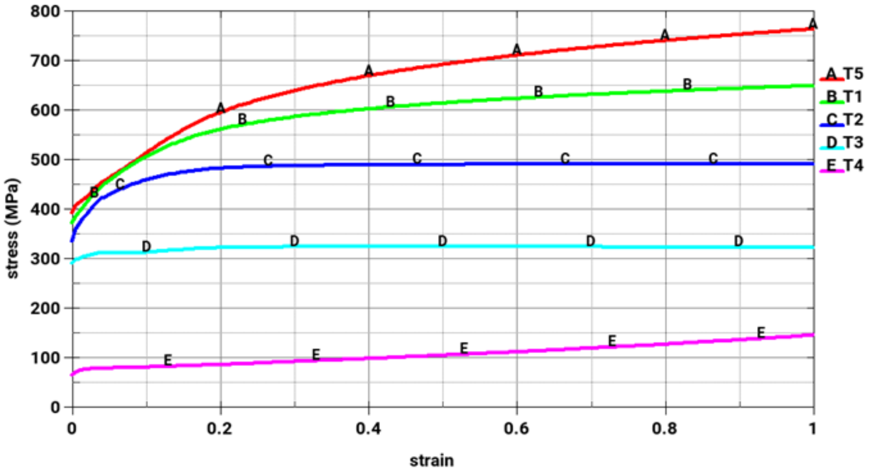

Figure 10. Scaled SS curves of LCKT of *MAT_224

4.3 UPDATE OF THE RATE DEPENDENT SS CURVES (LCK1) AND BETA COEFFICIENT

To develop the strain rate dependent, LCK1 tables, the tension and compression tests at the strain rates listed in tables 3 and 4 were conducted by OSU. The test's stresses versus nominal strain rates, at 5% strain of the specimen, are shown in figure 11. In addition, for the higher rate tension tests, the range of strain rates occurring during each test is also indicated. Note that when localization begins, multiple strain rates occur simultaneously in each tension test.

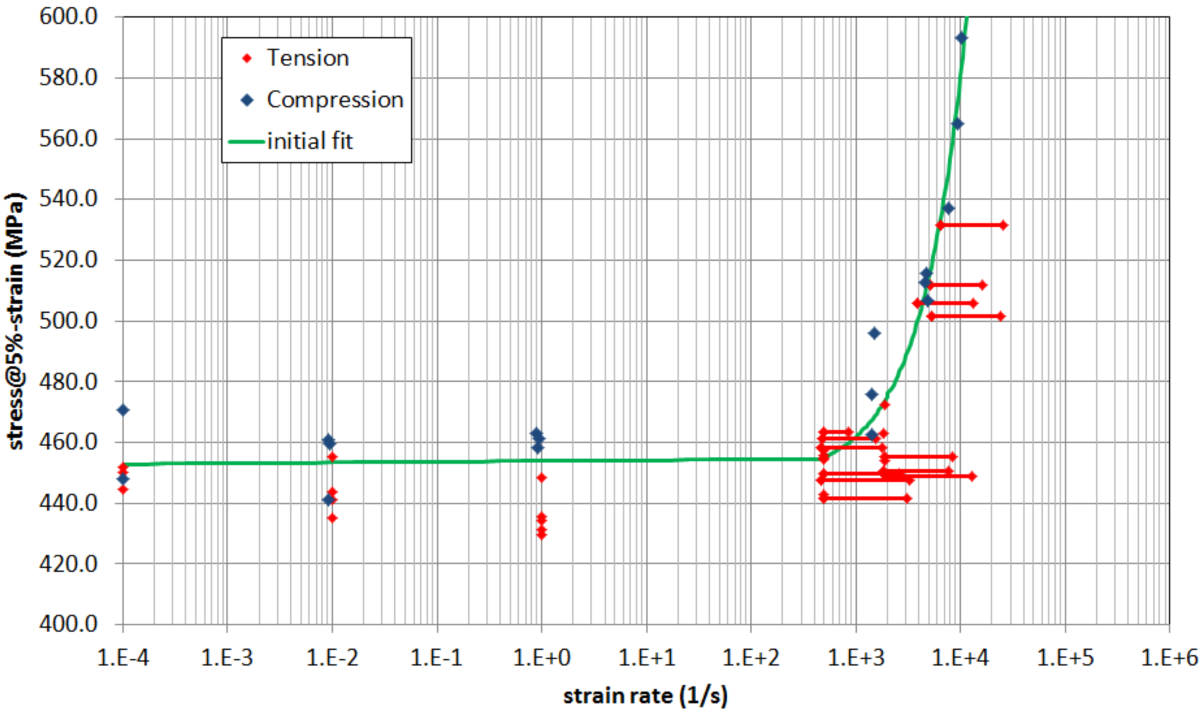

Figure 11. Stress at 5% strain versus strain rates of material rate tests, with higher strains also being indicated by the bars

The data points show that there is abrupt stress increase (at 5% strain) at approximately a strain rate of 10^3/sec. The sharp increase is predicted by theory that states "there was a small increase in strength, proportional to the logarithm of strain rate, at rates below 10^{-1}/sec, greater increase in sensitivity at rates between 10^{-1}/sec and 10^3/sec, and at rates above 10^3/sec even greater sensitivity with the increase being proportional to the strain rate" [19]. The increase in rate sensitivity is caused by a change in the physical processes as the specimen yields. The theory agrees with the strain rate series test results presented here.

The LCK1 input consists of a 3D table with a series of SS curves corresponding to the range of the strain rates from a quasi-static rate (10^{-4}/sec) to very high rate (more than 10^4/sec). The SS curve for the quasi-static strain rate was already developed, as shown in figure 7. An initial stress (at 5% strain) versus strain rate curve can be developed by fitting a curve on the test points, as shown in figure 11. Then, an initial LCK1 table can be developed by copying and shifting up the quasi-static SS curve repeatedly to the interval points of the stress (at 5%) versus strain rate curve fit.

However, as has occurred in previous modeling efforts [7, 8], this initial LCK1 does not provide acceptable test-matching simulations. Mainly, this is because the high rate tests are not iso-rate and are not isothermal. First, the actual strain rate within the localized region of necking in the specimen is much higher than the nominal strain rate, as shown in the bars of figure 11. For each of the test points shown in figure 11, there is a spread of equally applicable strain rates, starting at the shown nominal rate. As a result, the curve shown in figure 11 represents the highest physically possible slope. Second, there is not enough time for all heat generated by plastic deformation to dissipate when the strain rates are high, so the tests are not isothermal. Finally, whereas the difference in behavior between tension and compression in the tested Al-2024-T351 is small [6], there is some asymmetry. Therefore, the actual LCK1 tables need to be established by trial-and-error matching of the rate tensile tests with varying the stress versus strain rate curve and the dissipation factor.

During the analysis of the high rate tests, with their varying temperatures, temperature-dependent curves should be accessed to define the temperature-dependent response. This is why the LCKT table described in the previous section must be created first. The amount of heat generated, and therefore the temperature rise, is governed by the Taylor-Quinney coefficient, β. Figure 12 shows a previously published β range for Aluminum A2024 alloy is between 0.3 and 0.6.

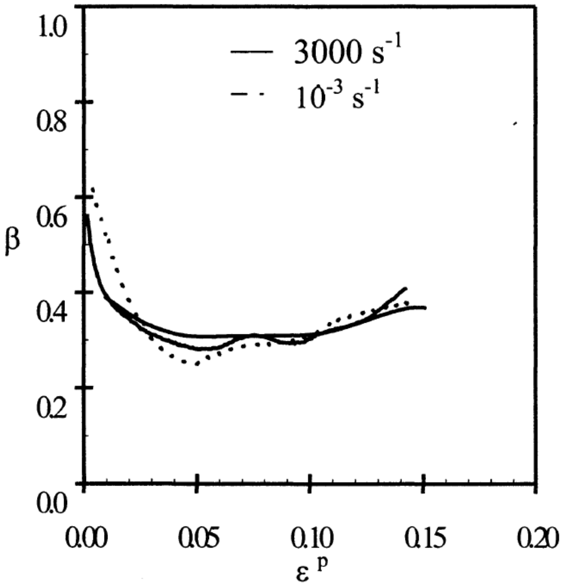

Figure 12. The dissipation factor of Aluminum A2024 alloy [20]

After many repeated trials, the final stress versus strain rate curve was obtained, as shown in figure 13. (The final curve is closer to abscissa values, which would be associated with the maximum strain rate observed in the tests rather than the nominal strain rate abscissa values.) Then, the updated LCK1 was defined as shown in figure 14. The dissipation factor β giving the best match was found to be 0.4. Figures 15–18 show the comparison of results of the rate tensile tests and simulations with using the updated LCK1. Overall, the figures show good matches between tests and simulations.

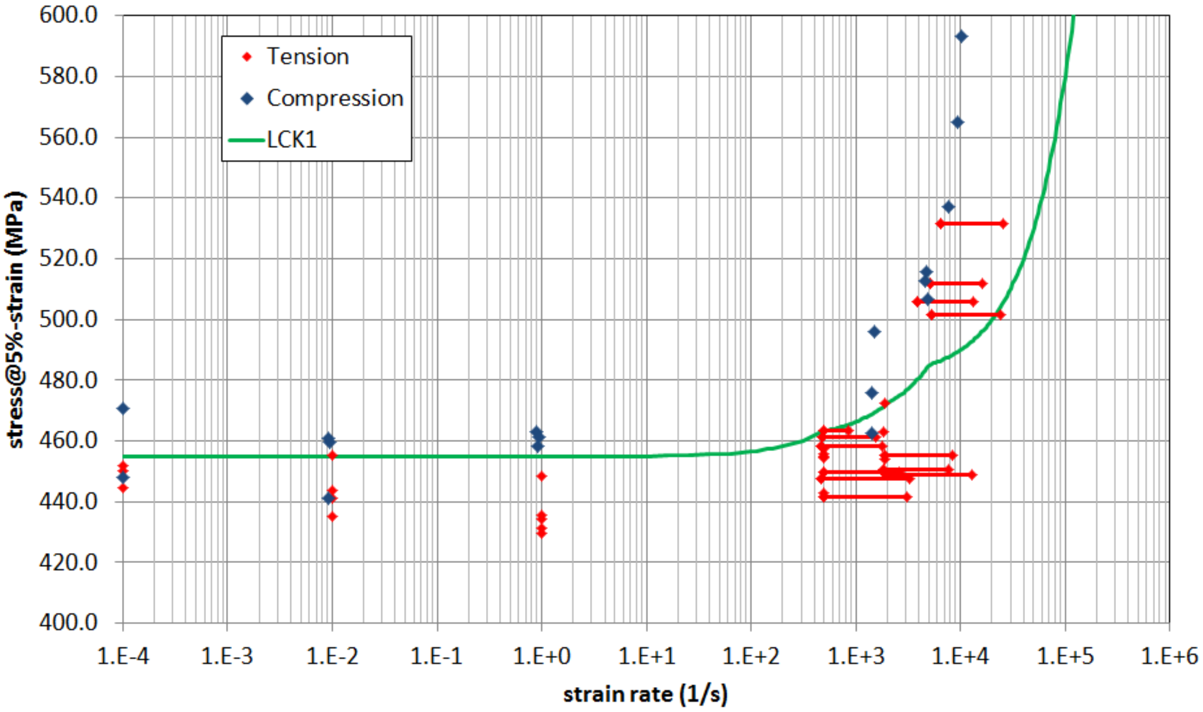

Figure 13. Developed stress at 5% strain versus strain rate curve

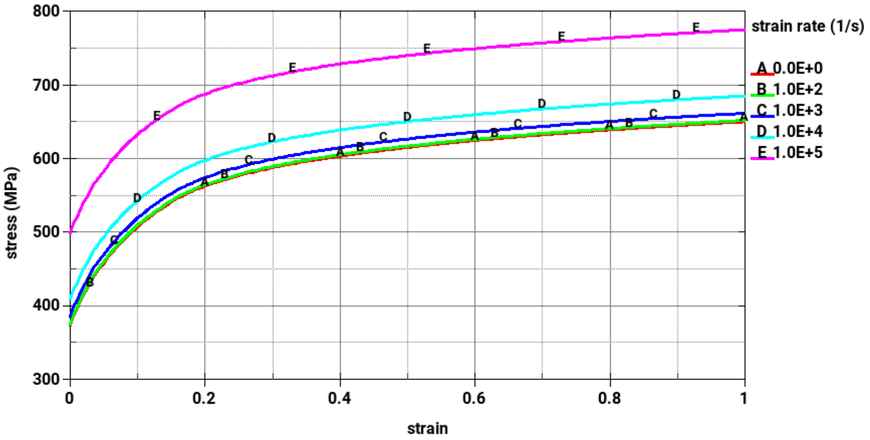

Figure 14. Stress versus strain curves in LCK1 of *MAT_224

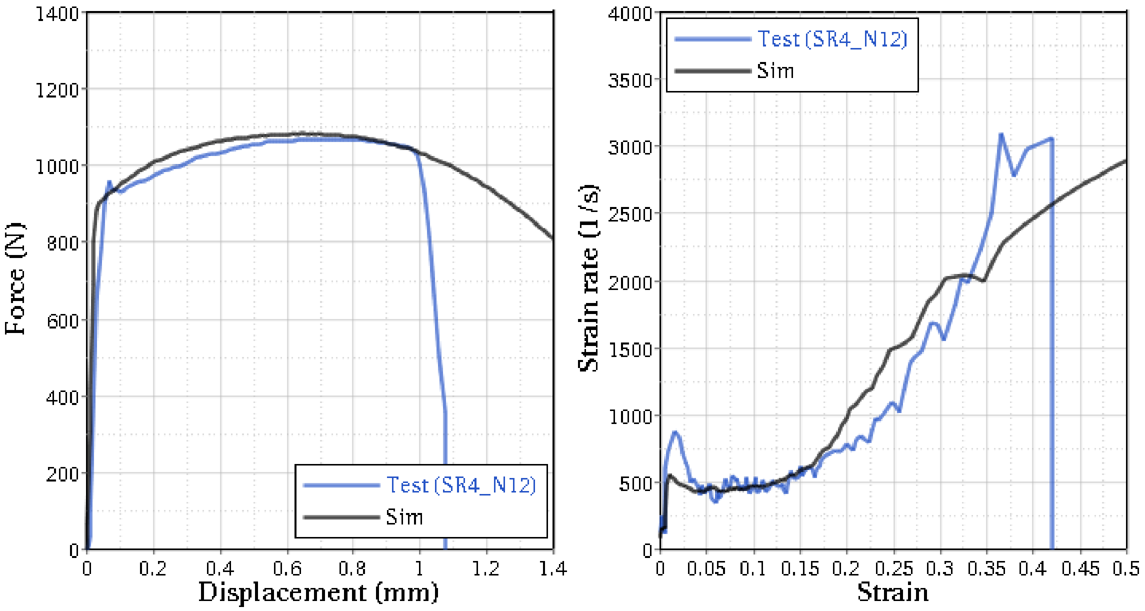

(a) (b)

Figure 15. Comparison of results of test and simulation in SR4 tension rate: (a) force versus displacement and (b) strain rate versus strain

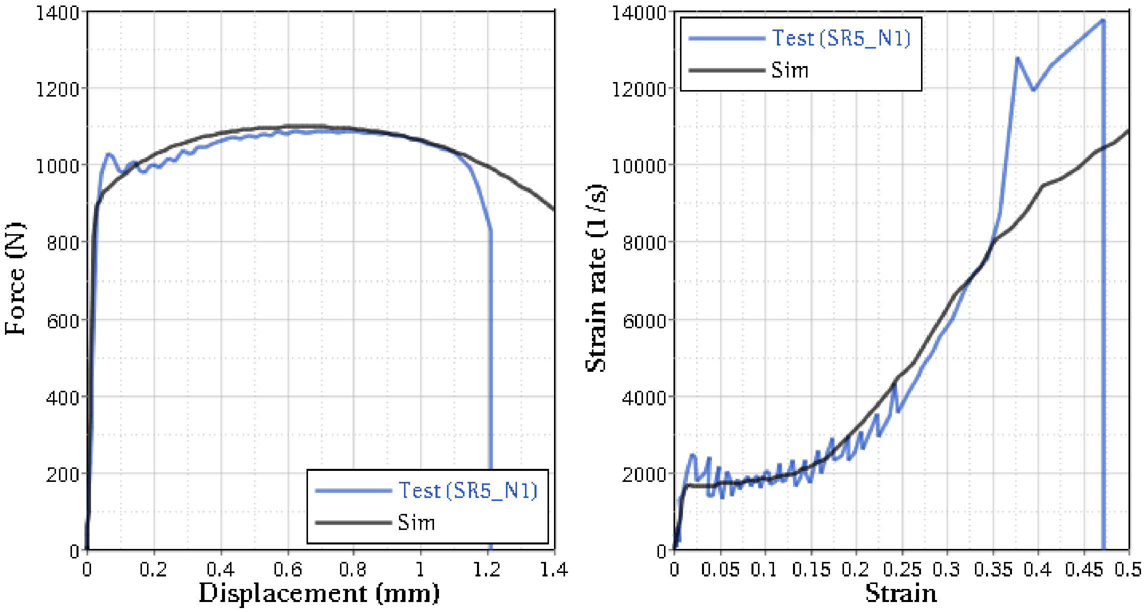

(a) (b)

Figure 16. Comparison of results of test and simulation in SR5 tension rate: (a) force versus displacement and (b) strain rate versus strain

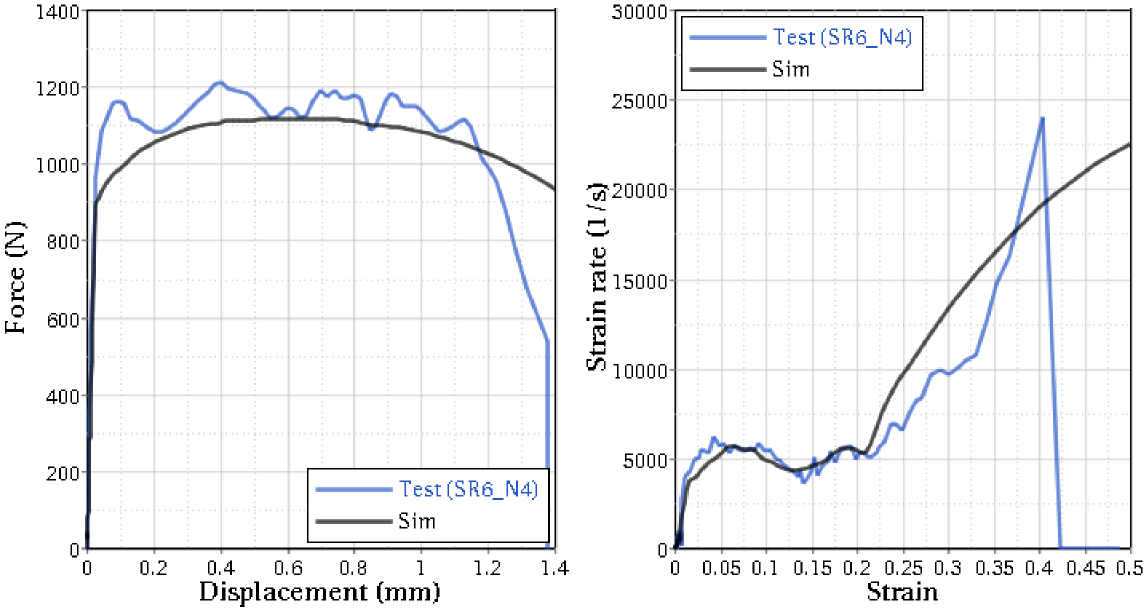

(a) (b)

Figure 17. Comparison of results of test and simulation in SR6 tension rate: (a) force versus displacement and (b) strain rate versus strain

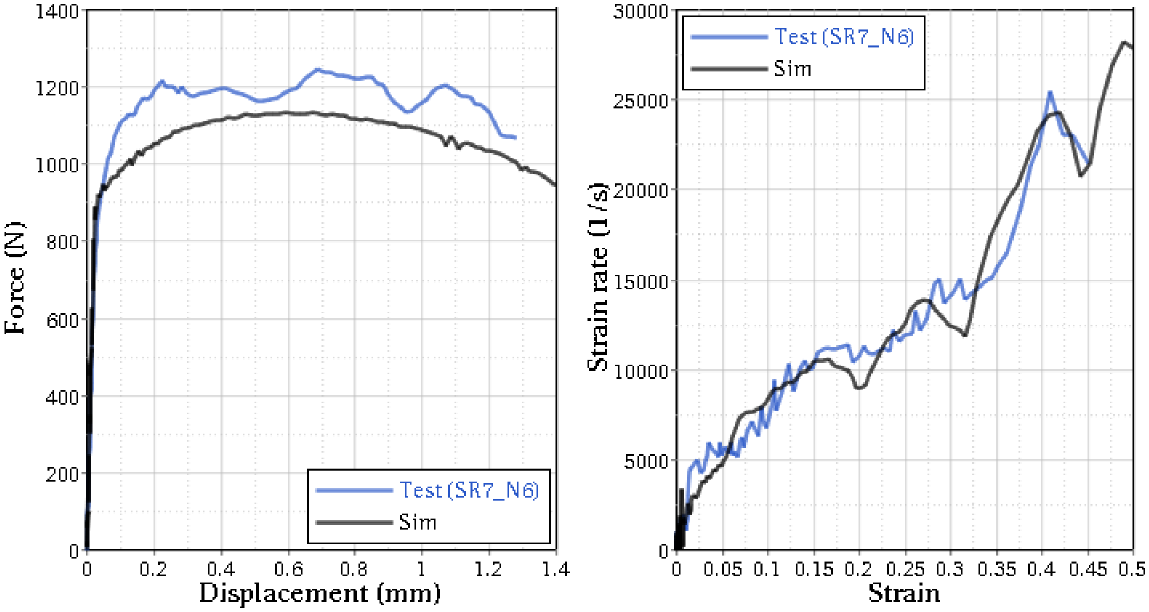

(a) (b)

Figure 18. Comparison of results of test and simulation in SR7 tension rate: (a) force versus displacement and (b) strain rate versus strain

In the FD plots, the matches are very close at the SR4 and SR5 rates, but the force levels of the simulations are a bit lower than the test force levels at SR6 and SR7 rates. (Note that for these tests, the displacements of the FD plots are obtained using DIC.) However, the results are acceptable because both force levels of simulations in SR6 and SR7 rates are within 10% of the test force levels shown in figure 19. In the strain rate versus strain plots, all of the simulations produce a very close match to the tests. It should be noted that the peak rates before failure reach 5–6 times higher than the nominal rates in all strain rate cases. Figures 20–23 compare the strain distributions on the specimen immediately before failure in simulations and tests. The simulations produce a very close match to the tests.

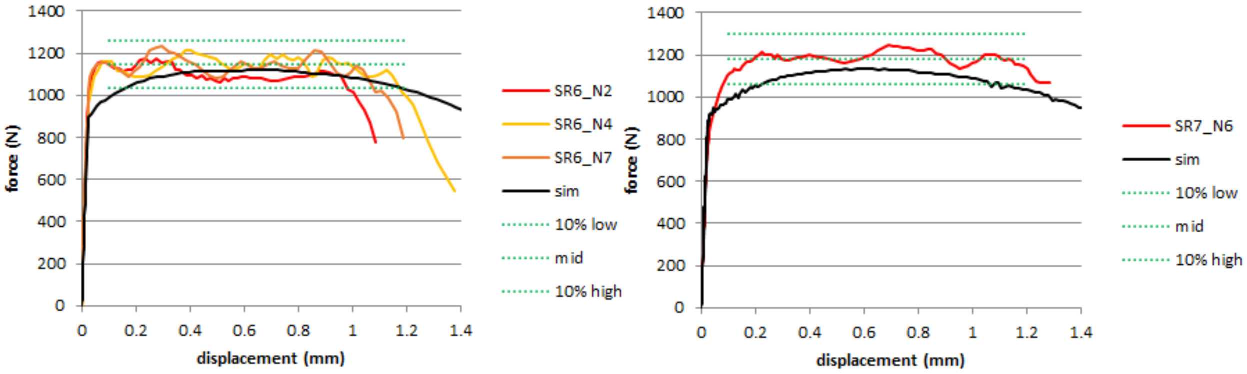

(a) (b)

Figure 19. FD plot of tension rate tests: (a) SR6 and (b) SR7

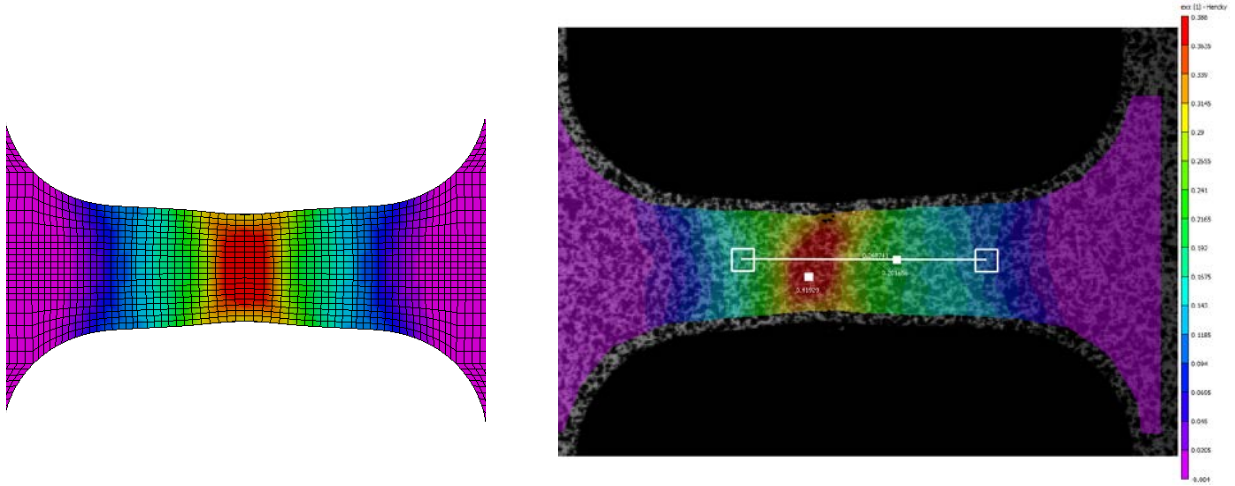

(a) (b)

Figure 20. Comparison of strain distributions of specimens in SR4 tension rate: (a) simulation and (b) test

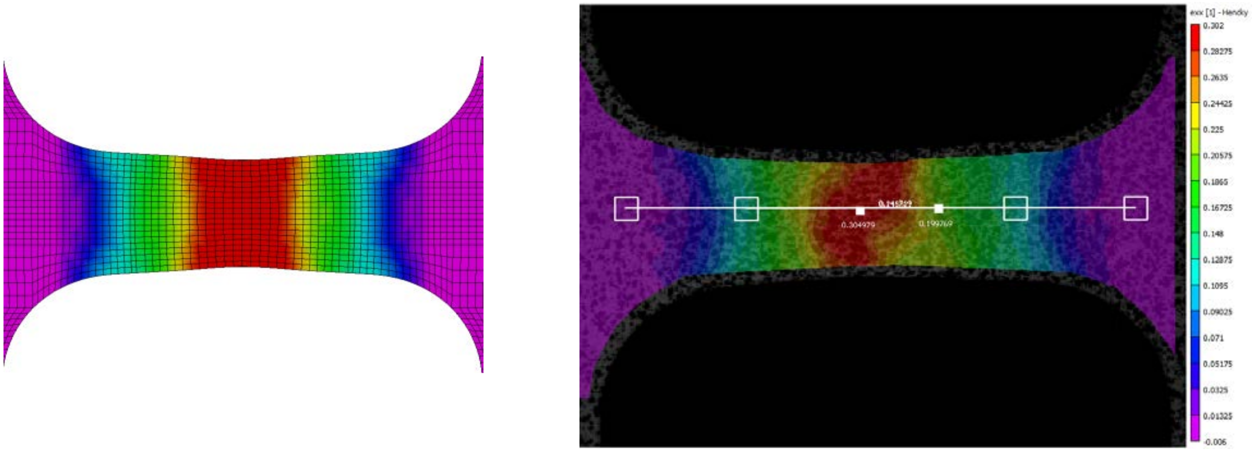

(a) (b)

Figure 21. Comparison of strain distributions of specimens in SR5 tension rate: (a) simulation and (b) test

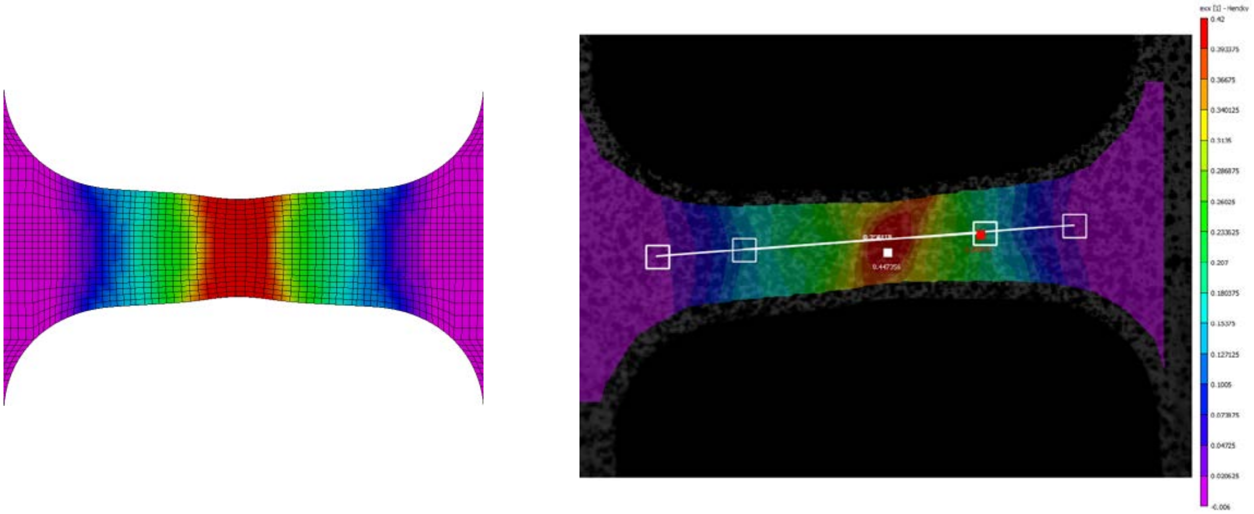

(a) (b)

Figure 22. Comparison of strain distributions of specimens in SR6 tension rate: (a) simulation and (b) test

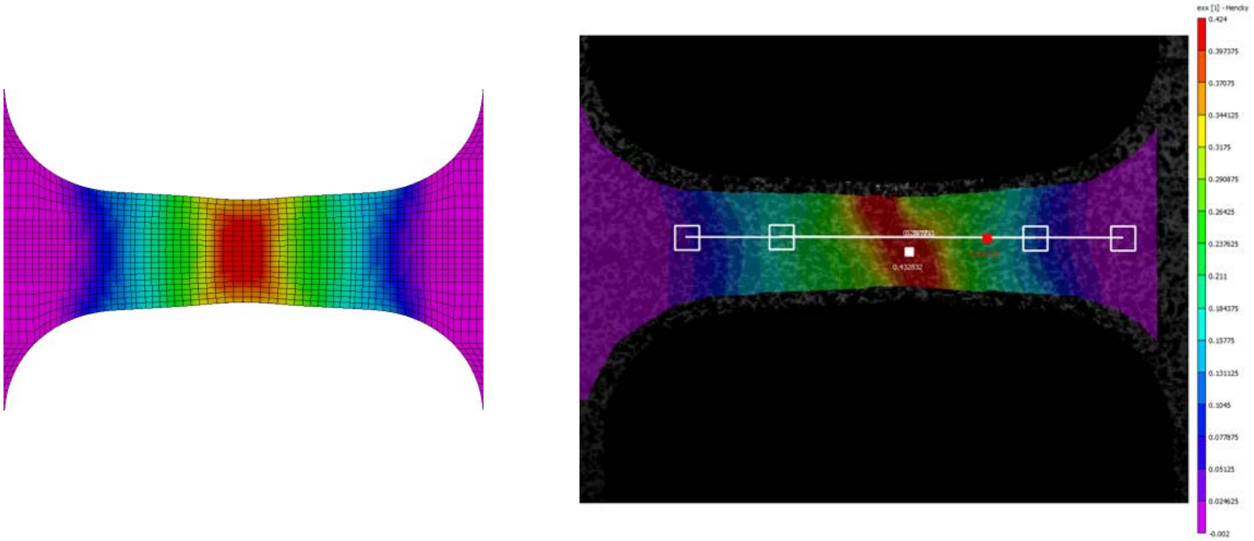

(a) (b)

Figure 23. Comparison of strain distributions of specimens in SR7 tension rate: (a) simulation and (b) test

Figure 24 shows the FD curve comparison of tests and simulations in the compression rate series. They show a good match for SR1, SR2, SR3, SR4, and SR5 compression rates. In the higher strain rate cases, such as SR6, SR7, and SR8, the force curves of simulations are slightly lower than the test force level initially and then the differences increase during the latter part of the tests. The increase in stress in the later part of the compression tests is partially due to friction, and therefore the test results do not represent a true material property. A detailed study of the friction in these tests was not deemed worthwhile.

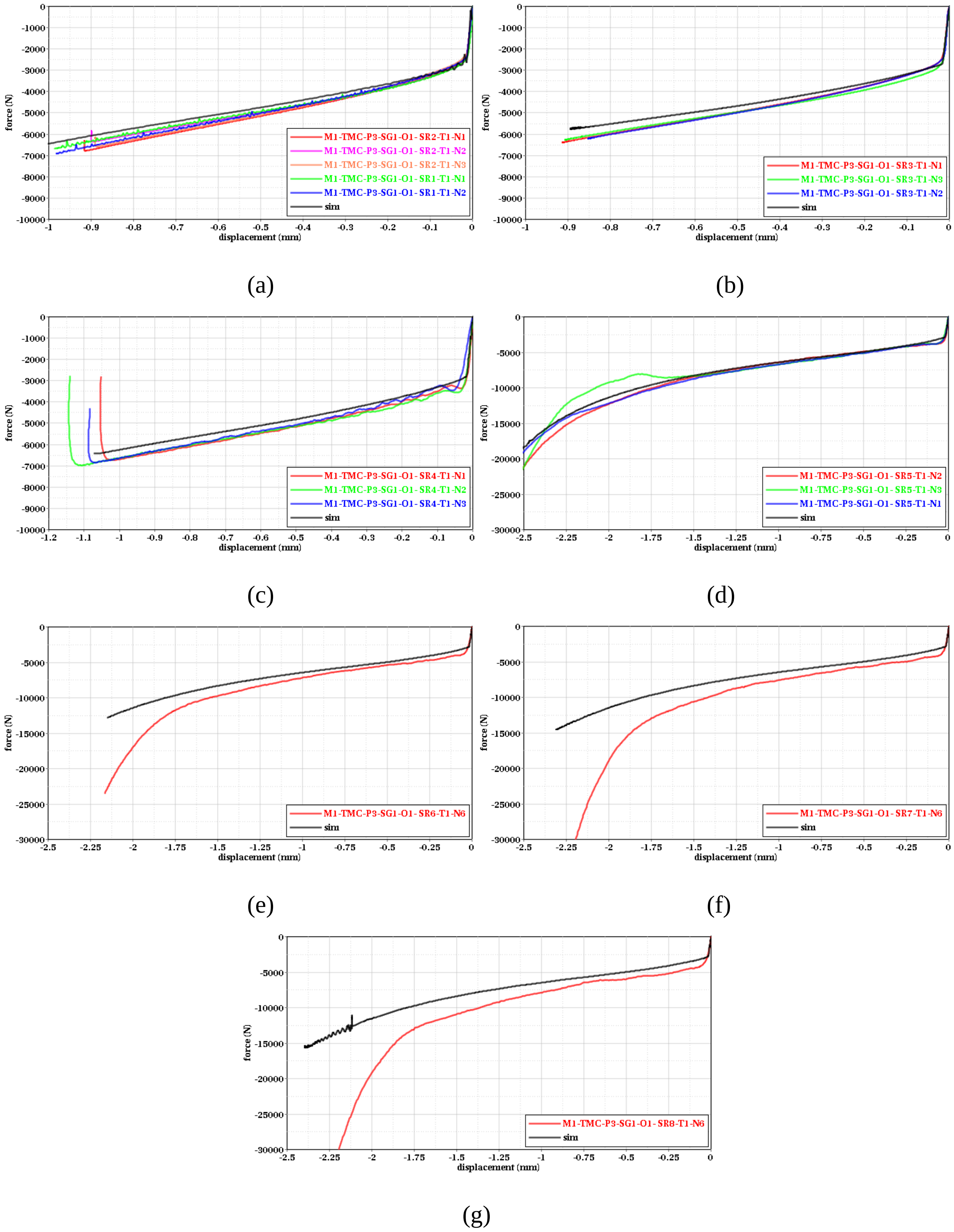

(a)

(b)

(c)

(d)

(e)

(f)

(g)

Figure 24. Comparison of FD curves of test and simulation in compression rate series: (a) SR1 and SR2, (b) SR3, (c) SR4, (d) SR5, (e) SR6, (f) SR7, and (g) SR8

4.4 UPDATE OF THE TRIAXIALITY AND LODE PARAMETER DEPENDENT FAILURE SURFACE (LCF)

The failure strain of the original Johnson-Cook material model is given by:

$$\varepsilon^f = [D_1 + D_2 \exp(D_3\sigma^*)][1 + D_4 \ln(\dot{\varepsilon}^*)][1 + D_5 T^*], \tag{14}$$

where $D_1 \cdots D_5$ are failure parameters, σ^* is triaxiality, $\dot{\varepsilon}^*$ is normalized strain rate, and T^* is homologous temperature [21]. The first term of the right side in equation 14 defines the failure strain curve in terms of triaxiality, which is an exponentially increasing curve when triaxiality is increasing. In *MAT_224, by the Johnson-Cook failure strain curve is extended to a failure strain surface, as the Lode parameter is added to triaxiality as a second defining variable. Having two defining variables allows for a complete characterization of a normalized three-dimensional state of stress. By using tabulated input, the failure surface can also provide a much closer match to the material properties than the failure parameters of the original Johnson-Cook model.

The LCF table defines the plastic failure strain, ε_p^f, as a function of the state of stress, as specified by the triaxiality and Lode parameter. It was developed by creating an approximate surface using failure plastic strains at various stress state points of the failure test series shown in tables 5–9. In the failure test series, every specimen’s geometry (shown in figure 4) and test condition were designed for a particular state of stress at initial failure. Table 12 summarizes the designed states of stress in all 21 failure tests. However, as measured in the actual test and reconstructed in simulations, the states of stress are a little different from the designed values, as shown in table 12. Figure 25 shows the actual state of stresses for all the failure tests, as a function of the Lode parameter versus the triaxiality. The states of stress of various triaxiality and Lode parameter combinations is described in appendix C.

Table 12. Triaxiality, Lode parameter, and failure plastic strain of failure test series

		Triaxiality (σ^*)		Lode parameter (L)		Plastic failure strain (ε_p^f)		Final plastic failure strain in the LCF
		designed	actual	designed	actual	low	high	
Plane stress series	SG1	-0.333	-0.333	1.000	1.000	0.21	0.30	0.25
	SG2	-0.431	-0.407	0.660	0.920	0.24	0.30	0.26
	SG3	-0.490	-0.470	0.415	0.663	0.23	0.26	0.24
	SG4	-0.577		0.000				
Axi-symmetric series	SG5	-0.333	-0.333	1.000	1.000	0.16	0.43	0.25
	SG6	-0.524	-0.636	1.000	1.000	0.27	0.34	0.29
	SG7	-0.607	-0.684	1.000	1.000	0.28	0.29	0.27
	SG8	-0.675	-0.743	1.000	1.000	0.26	0.28	0.26
	SG9	-0.763	-0.785	1.000	1.000	0.22	0.25	0.24
	SG10	-0.855	-0.870	1.000	1.000	0.20	0.22	0.22
Plane strain series	SG11	-0.577	-0.561	0.000	0.183	0.17	0.18	0.19
	SG12	-0.606	-0.644	0.000	0.074	0.19	0.22	0.19
	SG13	-0.730	-0.756	0.000	0.012	0.21	0.23	0.20
Tension-torsion series	LR1	-0.281	-0.269	0.805	0.940	0.24	0.27	0.23
	LR2	-0.188	-0.172	0.509	0.703	0.20	0.24	0.21
Torsion	LR3	0.000	0.000	0.000	0.000	0.12	0.20	0.22
Compression-torsion series	LR4	0.147	0.200	-0.390	-0.780	0.44	0.44	0.48
	LR5	0.233	0.388	-0.550	-0.961	0.33	0.39	0.60
New punch series	Unbacked	-0.670	-0.630	-1.000	-1.000	0.40	0.45	0.41
	Thin-backed	-0.200	-0.178	-1.000	-0.880	0.50		0.44
	Thick-backed	0.170	0.238	-1.000	-0.765	0.50		0.48

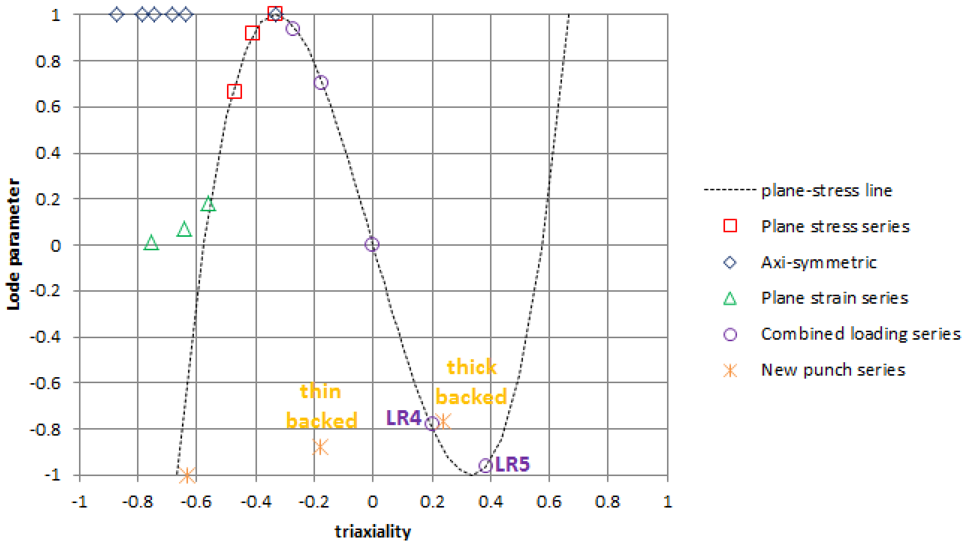

Figure 25. Actual state of stress locations of all the failure tests as defined by the Lode parameter vs. triaxiality

The SG4 failure test in the plane stress series was designed such that the initial failure should occur at the center of the specimen gauge area to achieve the desired state of stress. However, in the SG4 simulation, the initial failure occurs at the both edges of the gauge area, as shown in figures 26–27, where the state of stress is totally different than the desired values. Therefore, the SG4 failure test was not considered in developing the LCF.

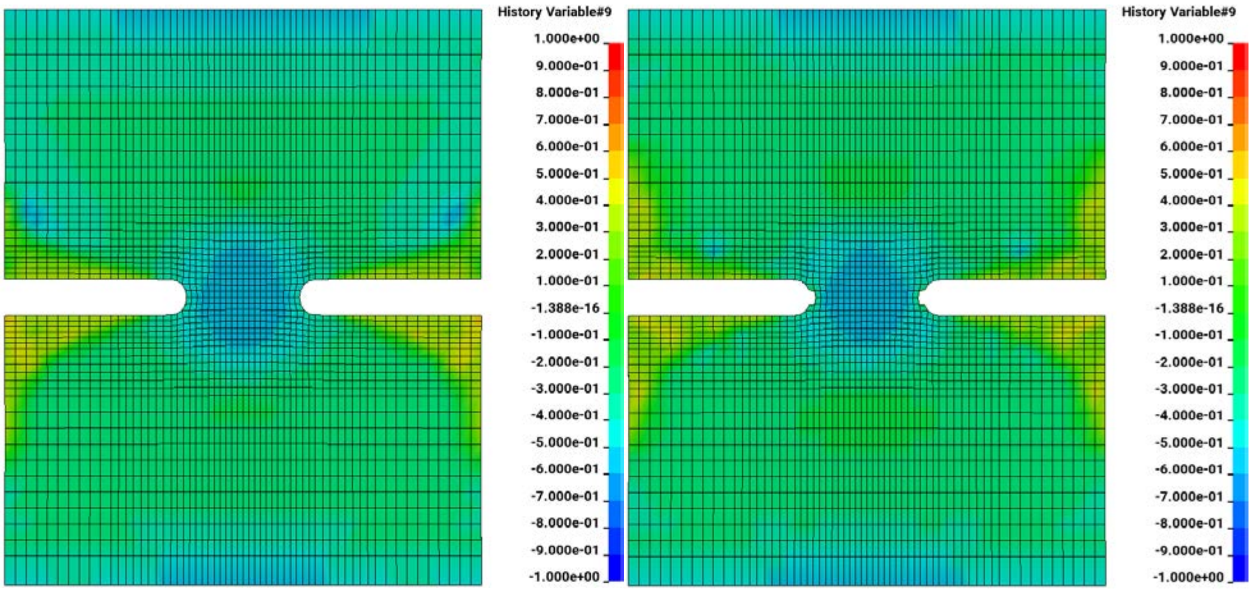

(a) (b)

Figure 26. SG4 failure test simulation (triaxiality contour): (a) right before initial failure and (b) right after initial failure

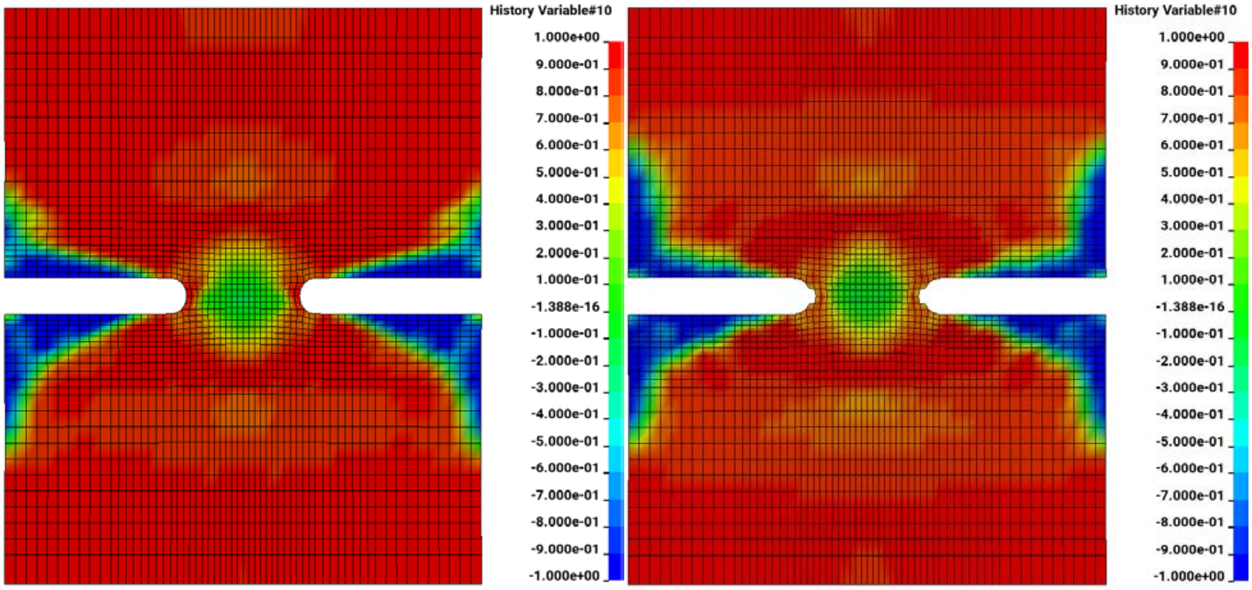

(a) (b)

Figure 27. SG4 failure test simulation (Lode parameter contour): (a) right before initial failure and (b) right after initial failure

Figures 28–34 show the FD (or torsion-angle) plots of all the failure tests. The low and high failure strains of failure tests summarized in table 12 were identified by iterative simulations to match the failure displacements in FD curves in figures 28–34. The approximate LCF surface of failure strain in the state of stress plane can be generated by using the failure strains in table 12.

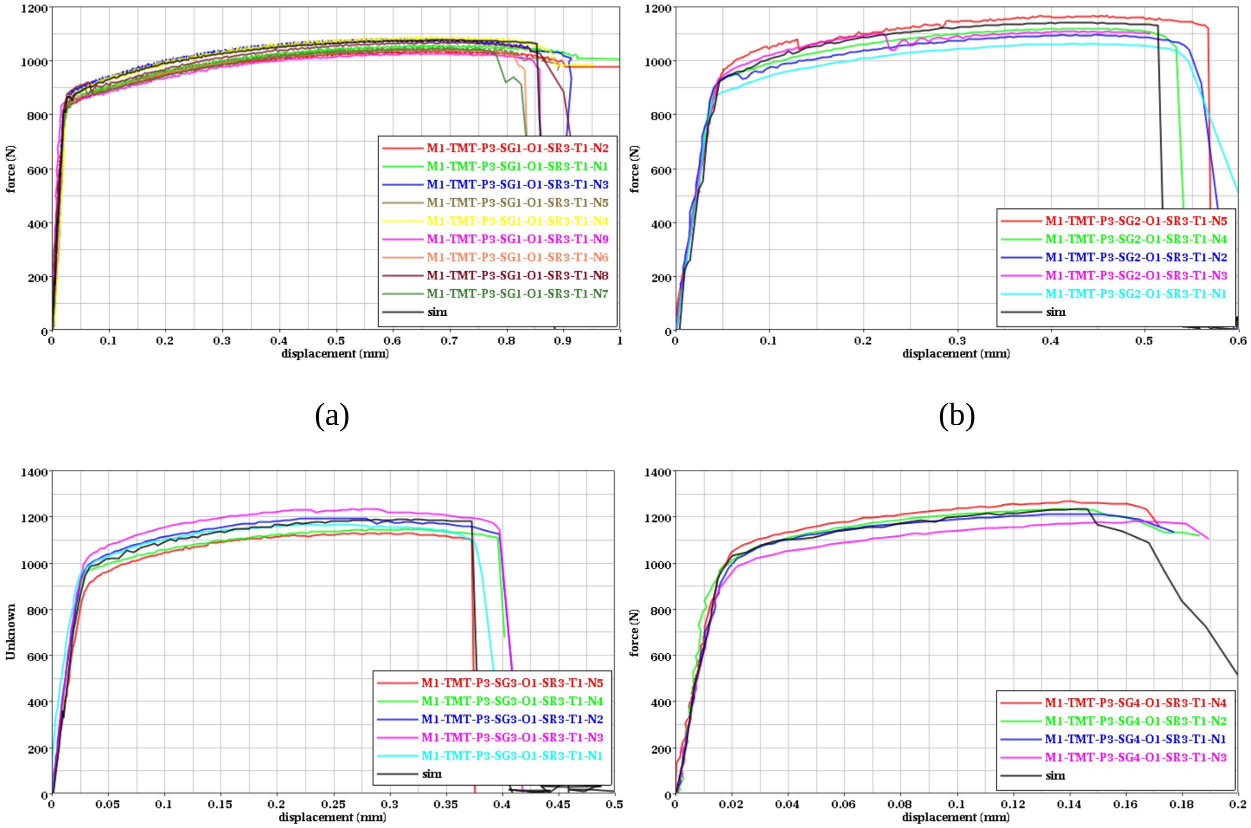

(a) (b)

(c) (d)

Figure 28. FD plots of failure test series—plane stress: (a) SG1, (b) SG2, (c) SG3, and (d) SG4

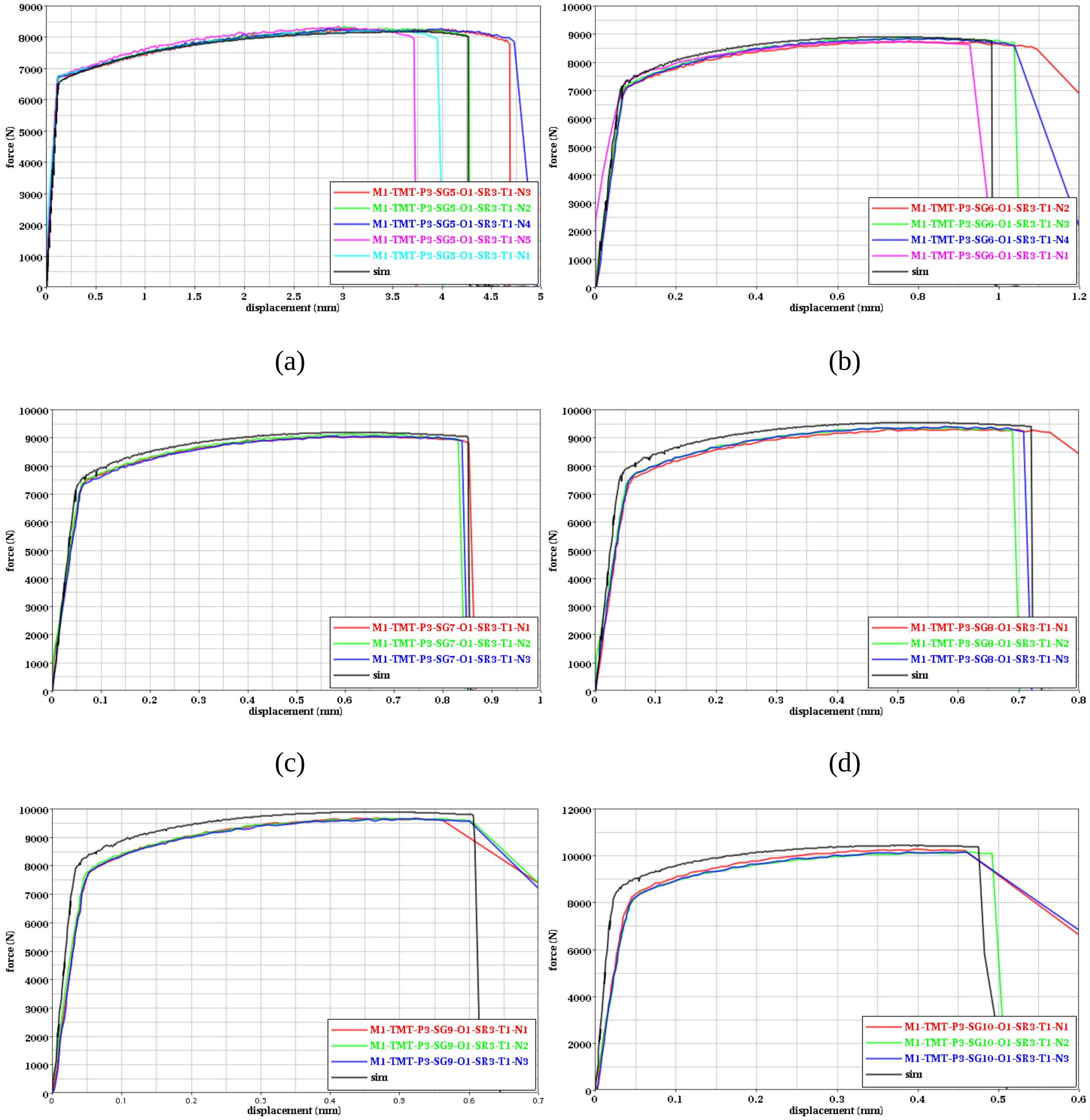

(a) (b)

(c) (d)

(e) (f)

Figure 29. FD plots of failure test series—axisymmetric: (a) SG5, (b) SG6, (c) SG7, (d) SG8, (e) SG9, and (f) SG10

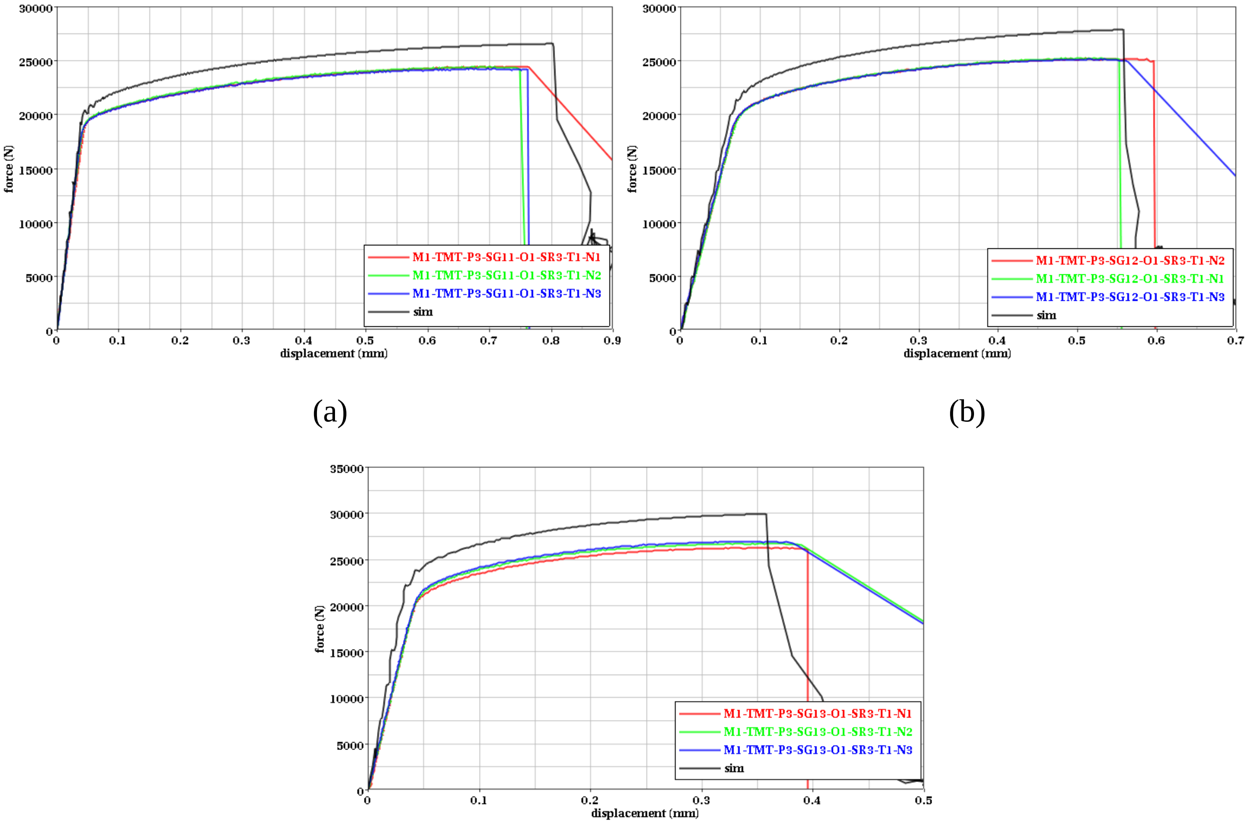

(a) (b)

(c)

Figure 30. FD plots of failure test series—plane strain: (a) SG11, (b) SG12, and (c) SG13

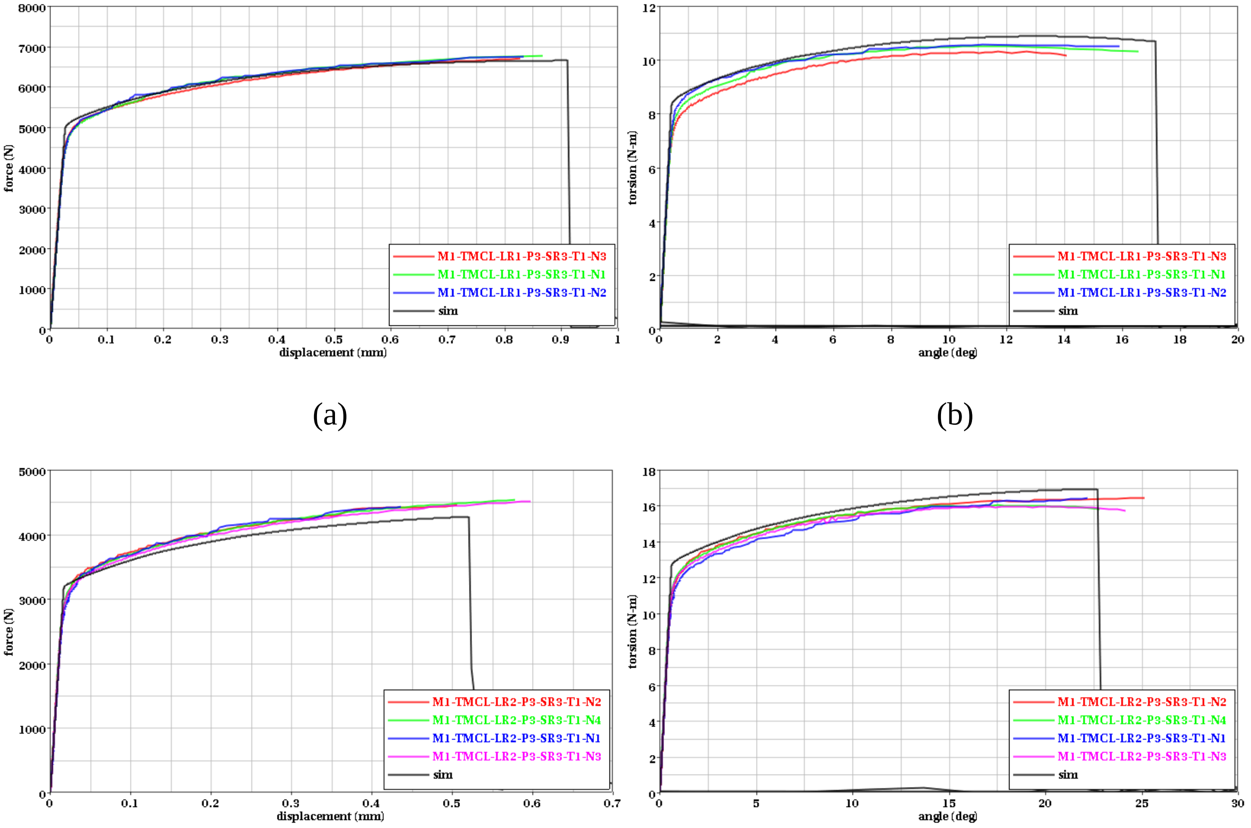

(a) (b)

(c) (d)

Figure 31. FD and torsion-angle plots of failure test series—tension-torsion combined: (a) FD of LR1, (b) torsion-angle of LR1, (c) FD of LR2, and (d) torsion-angle of LR2

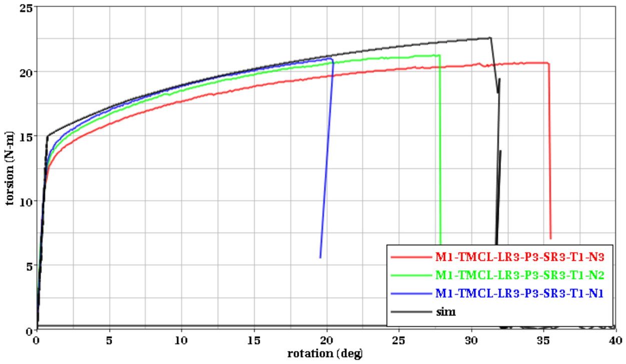

Figure 32. Torsion-angle plots of failure test series—torsion-angle of LR3

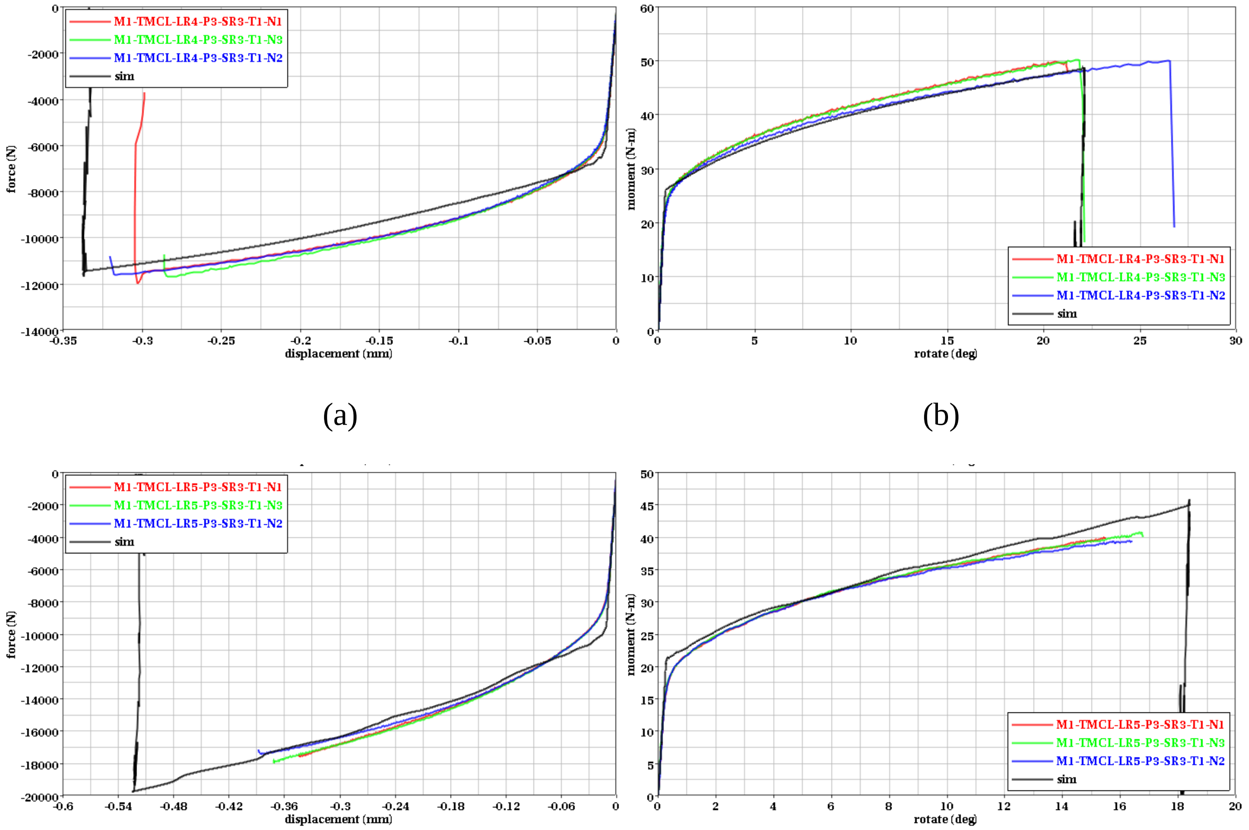

(a) (b)

(c) (d)

Figure 33. FD and torsion-angle plots of failure test series—compression-torsion combined: (a) FD of LR4, (b) torsion-angle of LR4, (c) FD of LR5, and (d) torsion-angle of LR5

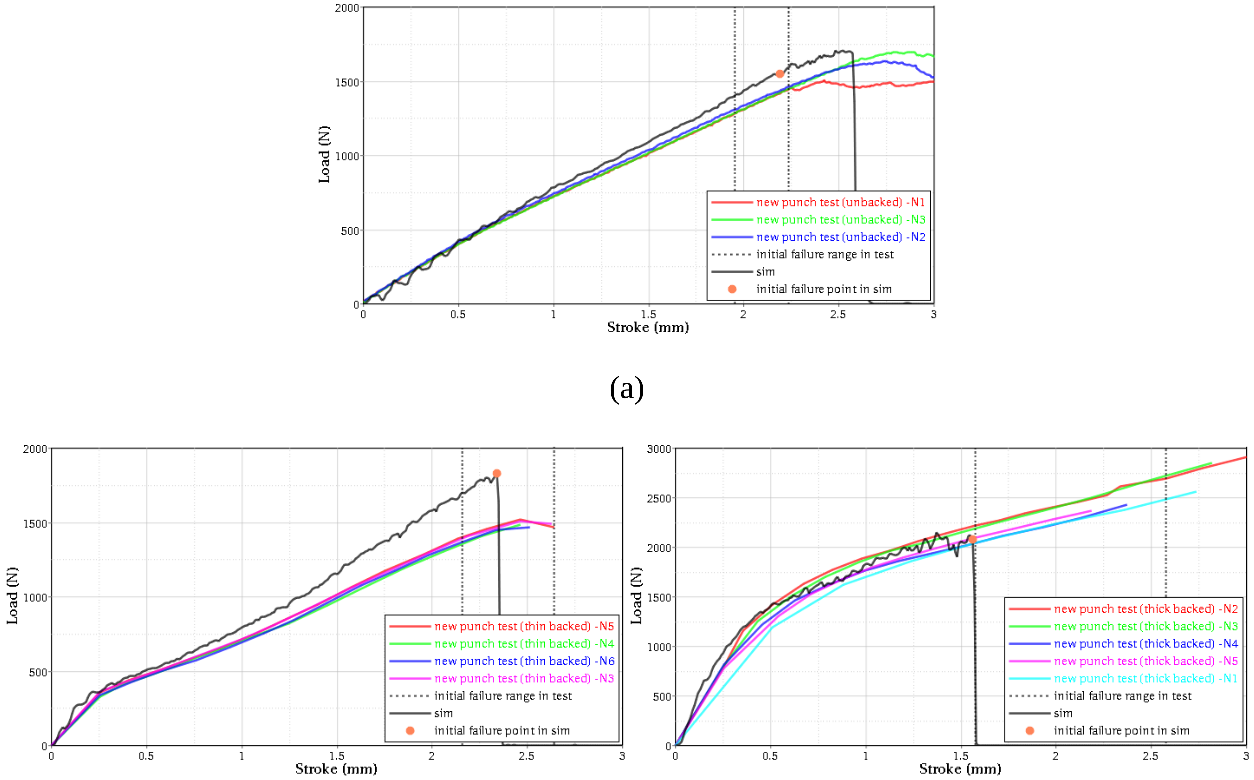

(a)

(b) (c)

Figure 34. FD plots of failure test series—new punch: (a) unbacked, (b) thin-backed plate, and (c) thick-backed plate

The new punch tests required more advanced simulation techniques. In the new punch tests with the backed plate, in the area between the punch and backing plate, the aluminum plate is placed under compressive force. Cracks are initiated in the area under compressive force and are propagated through the thickness, yet the material around the crack is still carrying compressive force. In most material test simulations, elements are eroded when their strain reaches their failure criteria. When the element is eroded, the eroded element will create a void that cannot carry force, which is fundamentally different from the actual failure. In addition, in the simulation, element erosion requires more deformation energy than crack initiation in the test, which leads to very high failure strains in the simulation.

To simulate crack initiation in the new punch test with a backed plate, an advanced modeling technique was used. In the advanced model, the solid elements are not connected by sharing common nodes. Instead, the nodes of neighbor solid elements are tied using the LS-DYNA keyword *CONSTRAINED_TIED_NODES_FAILURE. Then, the specified nodes are tied together until the *MAT_224 damage variable reaches unity, which occurs when the plastic failure strain exceeds the specified value. As a result, crack initiation is simulated by untying the nodes and no element erosion occurs.

However, non-eroding elements may also cause a numerical problem. Soon after tie-breaking, the detached elements can both distort excessively and entangle. After this occurs, the numerical solution becomes unreliable. Although excessive distortion makes the advanced simulation difficult, as discussed above, because there is no erosion, the load path is not eliminated as elements erode. Therefore, it provides for a much closer match to the tested force results than using element erosion. Using tied nodes to simulate the new punch test with a backed plate after initial failure also provides a more reasonable failure strain. This more accurate failure strain was important in the development of the final LCF.

The initial, state-of-stress dependent, failure strain surface (LCF table) is created by using the failure strains listed in table 12. To make the LCF match the failure test series, a significant number of iterative simulations were conducted by adjusting the failure strains at the control points between the low and high values. Next, as shown in figure 25, these 21 stress state failure strains (control points) do not cover the complete surface. Several assumptions were made to create the surface in areas without any control points. The basic approach to develop the failure strain surface in those regions is as follows:

- The area of approximately $-1.0 \leq \sigma^* \leq 0.6$ and $0.0 \leq L \leq 1.0$:

  In this area, there are reasonably enough control points, as shown in figure 25, to create an approximate surface. However, there is no control point in the $0.0 \leq \sigma^* \leq 0.6$ region. Therefore, it was assumed that the failure strains increase as the triaxiality increases, similar to the failure strain curve of the Johnson-Cook material model in equation 14.

- The area of approximately $-1.0 \leq \sigma^* \leq 0.6$ and $-1.0 \leq L \leq 0.0$:

  It is very important to create the proper surface in this area, because failure of plates in many ballistic impact tests is initiated under these states of stress. However, it is difficult to develop simple material property tests and specimens, which will fail under these states of stress. As a result, in this area, there are few control points available, as shown in figure 25.

  These control points come from two types of material tests: 1) compression-torsion combined load tests and 2) the new punch tests. Unfortunately, the failure strains identified by these two different types of tests are inconsistent. Specifically, as shown in figure 25, the state of stress in the thick-backed punch test is very close to the state of stress in the combined LR4 compression-torsion test. However, the failure strain in the thick-backed punch test is more than 0.5, but the failure strain in the LR4 test is below 0.5, as listed in table 12. Moreover, the failure strain in the LR5 test is smaller than the failure strain in the LR4 test, even though the triaxiality in the LR5 test is higher than the triaxiality in the LR4 test. This result is inconsistent with the general observation that failure strains increase with higher degrees of compression, which results in no failure in hydrostatic compression. (This general observation resulted in the assumption used in the Johnson-Cook material model [see equation 14] of increasing failure strain as the triaxiality is increasing.) As a result, matching LR4, LR5, and the thick-backed punch test with a single failure surface was not possible, and priority was given to matching the thick-backed punch test results.

  The final failure surface (LCF table) was developed by many iterative simulations of the material tests and the ballistic tests introduced in section 3.2. With the test series of the spherical projectiles impacting the 0.25-inch Al-2024 plate, using the LR4 and the LR5 failure strains yields ballistic limit predictions, which are too low. This result is consistent with giving priority to the thick-backed punch test failure strains. The final failure strain, as shown in table 12, yields a closer match to both the thick-backed punch test and the impact tests than the compression-torsion combined load tests.

- The area of approximately $\sigma^* \leq -1.0$ and $-1.0 \leq L \leq 1.0$:

  In this area, the surface is extended by extrapolation until $\sigma^* = -2.0$, with the failure strains decreasing. Then, it becomes flat. Even in hydrostatic tension, failure strains do not approach zero.

- The area of approximately $\sigma^* \geq 0.6$ and $-1.0 \leq L \leq 0.0$:

  The state of stress can be in this region near to the surface of impacted plates, especially the thicker ones as shown in figure 35. No material property test data are available for this area. The failure strain of the plateau was selected by iterative simulations of ballistic tests introduced in section 3.2. To simplify the iterative process, a flat plateau shape of the surface was adopted from $\sigma^* = 0.6$ until $\sigma^* = 4.0$. If this failure strain plateau is set too low, elements near the impacted surface under a compressive dominated state of stress will fail prematurely resulting in an unrealistic failure morphology. If this failure strain plateau is set too high, non-failure of elements near the surface prevents shear-band failure of the interior elements. In this case, the shear-band failure typical of thicker plates never initiates. At $\sigma^* \geq 4.0$, the surface increases rapidly as the triaxiality increases, similar to the failure strain curve of the Johnson-Cook material model (see equation 14).

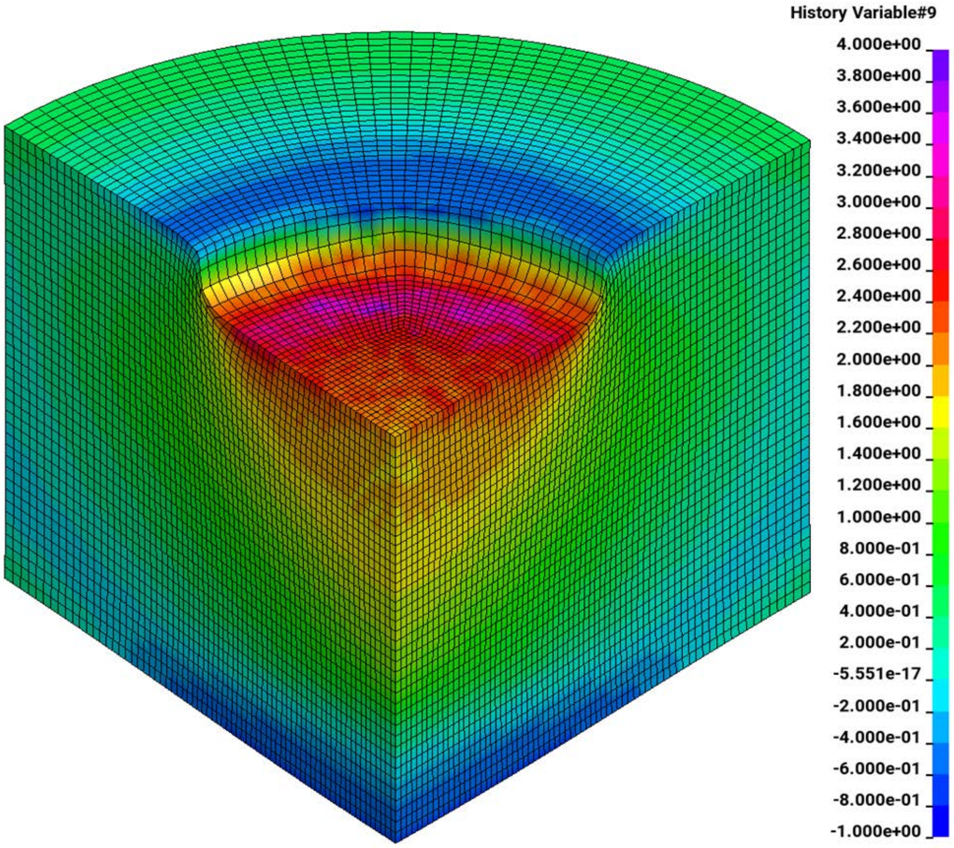

Figure 35. Contour plot of triaxiality (history variable #9), just before element erosion begins, demonstrating that the elements are in the plateau region ($\mathbf{4.0} \geq \boldsymbol{\sigma}^{*} \geq \mathbf{0.6}$).

Figure 36 shows the updated LCF table of *MAT_224. It was used to simulate the failure test series to confirm that it worked for all the simulations. Figures 28–34 show the comparison of the FD curves between tests and simulations. Mostly, they show good matches between tests and simulations in terms of force level and displacement at failure. Figures 34(b) and 34(c) show the new punch tests with backed plates. In these simulations, the displacement at failure in the FD curves is within the test range; the force drops down quickly unlike tests. This quick drop in force is caused by numerical instability after the initial failure.

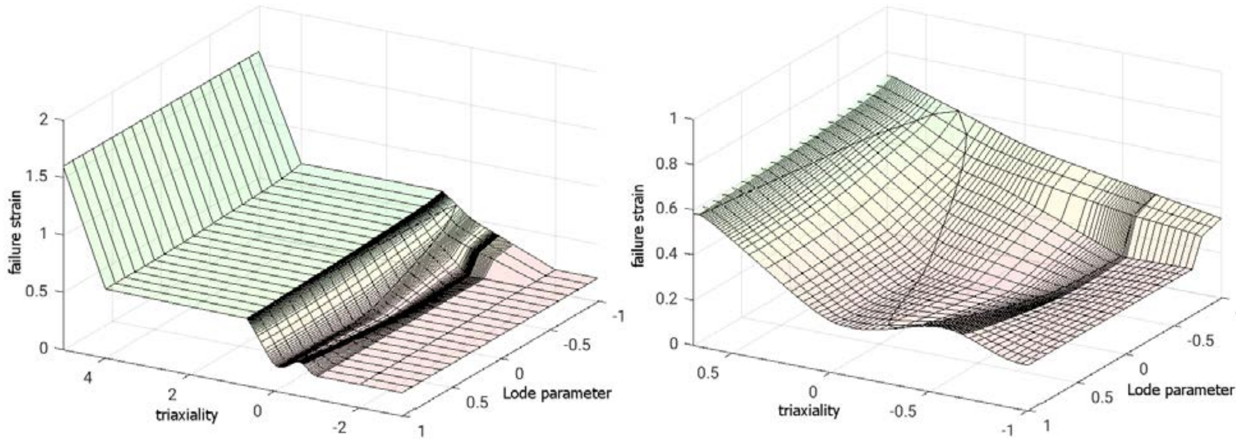

(a) (b)

Figure 36. Updated LCF of *MAT_224: (a) full range of Lode parameter, and (b) zoomimg-up the range of $-1.0 \leq \mathbf{Lode\ parameter} \leq 0.7$.

Alternate LCF tables, containing theoretically defined failure surfaces are shown in appendix D. Comparisons of analysis using these alternate approaches to ballistic tests are also shown in Appendix D.

4.5 UPDATE OF THE TEMPERATURE SCALING OF THE FAILURE SURFACE (LCH)

The LCH is the scale factor curve of the plastic failure strain ε_p^f as a function of temperature. It scales the LCF table and is created after the LCF table is complete. The LCH curve can be developed by normalizing the plastic failure strains in tensile tests of the temperature series, as shown in table 2. The low and high failure strains at each different temperature were identified by iterative tensile simulations, matching the failure displacements of FD curves shown in figure 8. Figure 37 shows the low and high failure strains and their average strains at the different temperatures. Their normalization is defined as:

$$h(T) = \frac{\varepsilon_p^f(T)}{\varepsilon_p^f(\mathbf{T1})}. \tag{15}$$

The updated LCH curve, shown in figure 38, was developed by interpolating the average points. To remove any non-physical extrapolation leading to instability, the LCH becomes flat below temperature T1 and over temperature T4.

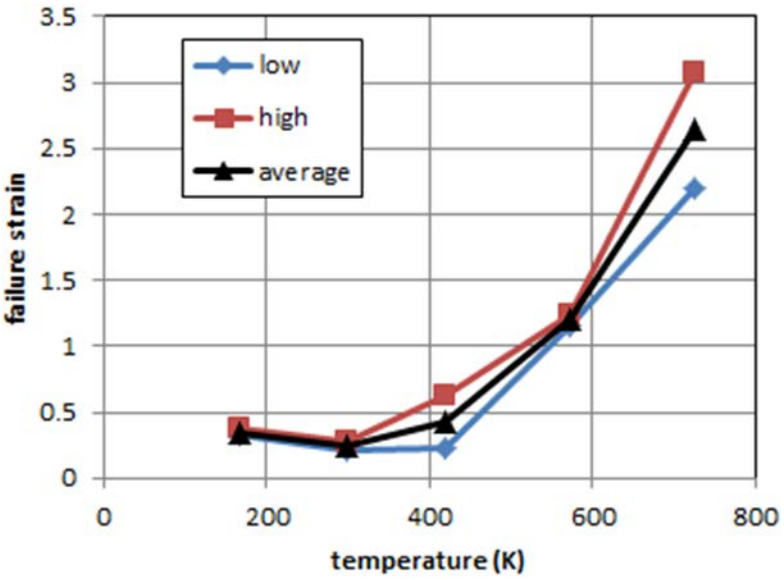

Figure 37. Low, high, and average failure strains at different temperatures

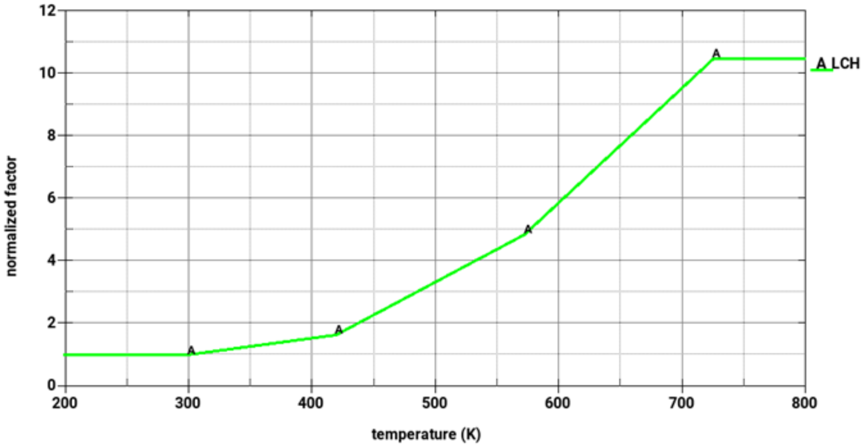

Figure 38. Updated LCH of *MAT_224

4.6 UPDATE OF STRAIN RATE SCALING OF THE FAILURE SURFACE (LCG)

The LCG is the scale factor curve of the plastic failure strain ε_p^f as a function of strain rate. It scales the LCF table and it is created after the LCH curve is complete. It can be developed by normalizing the plastic failure strains in tensile tests of rate series, as shown in tables 3 and 4. Figure 39 shows the data points of the failure strains versus strain rates at the moments of specimen failure, which were identified by iterative tensile simulations to match the failure displacements in FD curves. There are two datasets; the one dataset is obtained from the rate tests conducted in the previous research and the other dataset is obtained from the additional higher rate tests. Note that the displacements from these new tests were obtained using DIC.

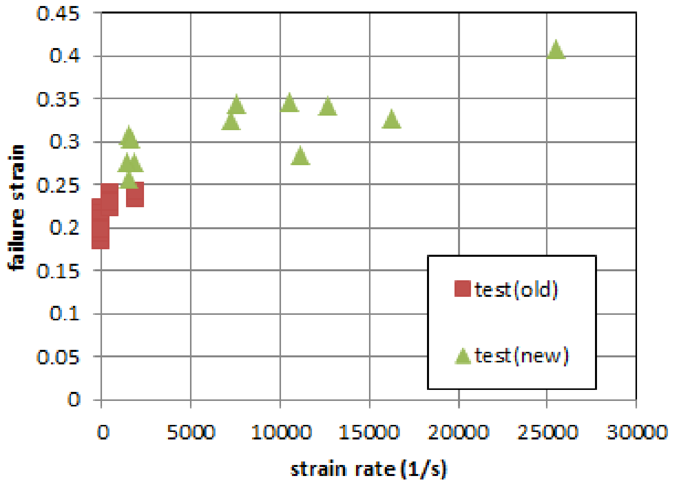

Figure 39. Failure strains versus strain rates at the moments of specimen failure

The failure strains are normalized by:

$$g(\dot{\varepsilon}_p) = \frac{\varepsilon_p^f(\dot{\varepsilon}_p)}{\varepsilon_p^f(\mathbf{SR1})}, \tag{16}$$

as shown in figure 40. The second term of the failure strain of the Johnson-Cook material model in equation 14 corresponds to the LCG of *MAT_224 and is defined as a logarithmic function. Therefore, the LCG curve was created as a logarithmic function of the strain rate. The final LCG curve was developed using many iterative tensile simulations of the rate series shown in figure 40. Figure 41 shows the FD curves of rate tensile tests. It is observed that the simulation failure displacements match the tests well for all the rate cases.

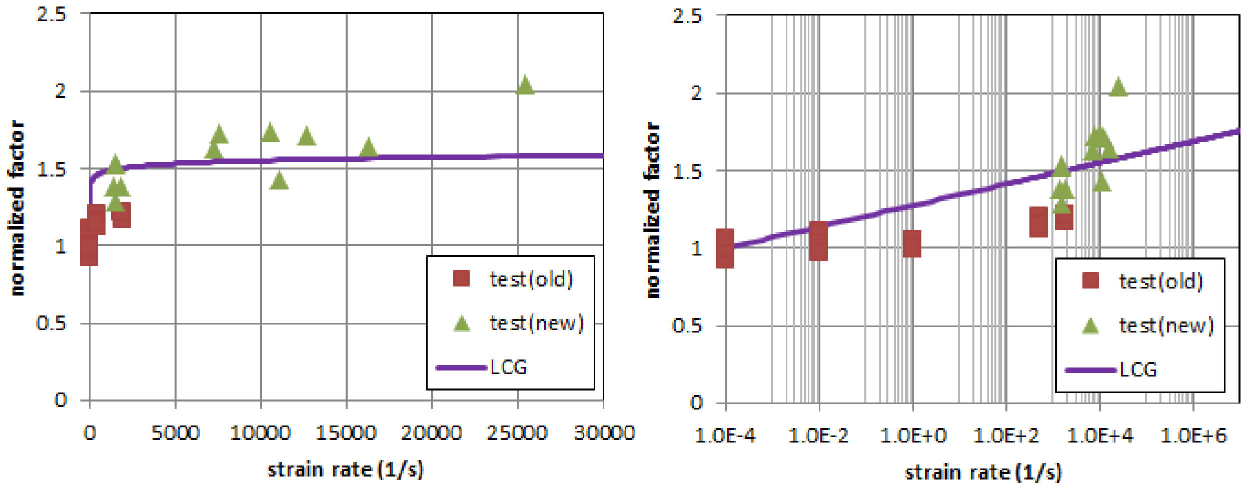

Figure 40. Updated LCG of *MAT_224: (a) linear scale in *x*-axis and (b) logarithmic scale in *x*-axis

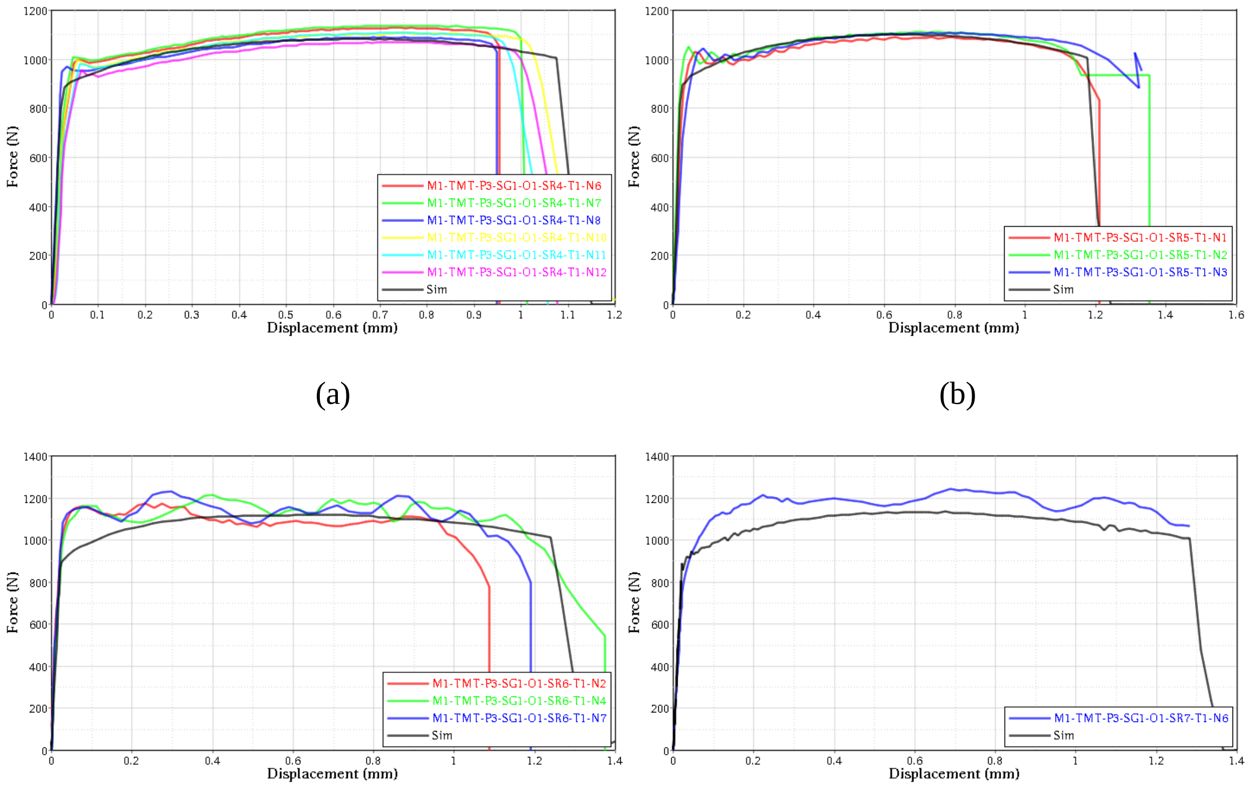

(a) (b)

(c) (d)

Figure 41. Comparison of FE curves of test and simulation in tension rate series: (a) SR4, (b) SR5, (c) SR6, and (d) SR7

4.7 UPDATE OF THE MESH REGULARIZATION (LCI)

In most simulations, element failure is influenced by the element size in FE mesh. Element removal with the unavoidable mesh dependency is regularized by the LCI in *MAT_224. The LCI is defined as a scale factor curve or surface of the plastic failure strain ε_p^f, as a function of element size, triaxiality, and Lode parameter. The element size of a solid element in LS-DYNA is defined as the characteristic length l_c, which is calculated as:

$$l_c = \frac{V_e}{A_{e_{max}}}, \tag{17}$$

where V_e is the volume of a solid element, and $A_{e_{max}}$ is the area of the largest side of a solid element [22]. Regularization performance degrades as the aspect ratio of the solid element deviates from 1:1:1. The LCI can be developed by normalizing the plastic failure strains from FE models with different element sizes in a particular state of stress, such as:

$$i(l_c, \sigma^*, L) = \frac{\varepsilon_p^f(l_c, \sigma^*, L)}{\varepsilon_p^f(\boldsymbol{l_c^{baseline}}, \sigma^*, L)}. \tag{18}$$

In this study, the baseline characteristic length $l_c^{baseline}$ was set to approximately 0.15 mm in all FE models. All of the preceding analysis was conducting using elements of approximately this size.

In the original Al-2024 material model, the LCI was defined as a function of element size only, using the SG1 tensile test simulations with different mesh sizes. This means that the original LCI was independent of the state of stress. In the new material model, the updated LCI is defined as a function of element size, triaxiality, and Lode parameter, because it was realized that the mesh size dependency was not only a function of element size but also a function of the state of stress. First, to see the dependence of regularization on triaxiality and Lode parameter, six material tests in the different states of stress were selected, as shown in figure 42. Multiple FE models with differing element sizes were developed, with varying numbers of elements through the thickness direction of the specimens. The characteristic length (element size) of the FE models for six material test simulations is summarized in table 13.

Note that only one element through the thickness can generate an approximately correct state of stress in an uni-axial state of stress, such as SG1. This is not the case with other specimens and states of stress, in which multiple elements through the thickness are required.

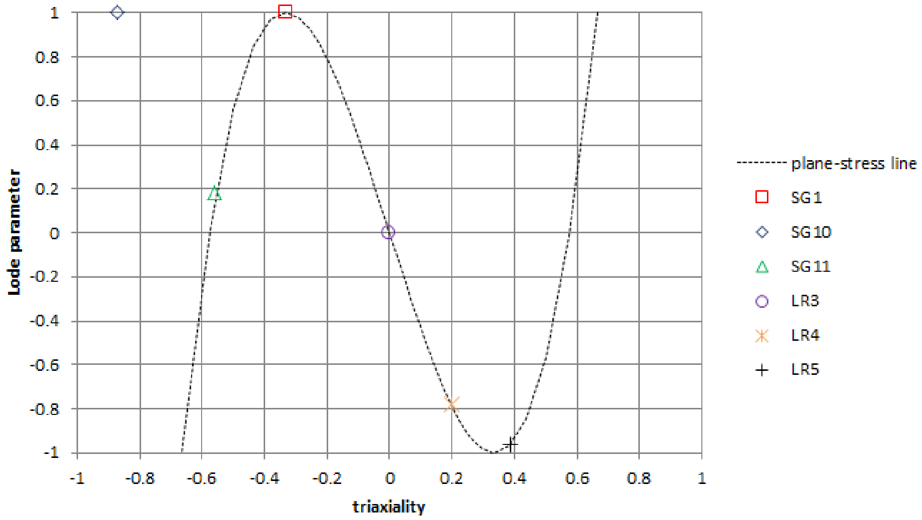

Figure 42. The state of stress of specimens of material tests selected for developing regularization

Table 13. Element dimension of each of the models used to develop the LCI table

Number of elements through thickness	Characteristic length of an initial failure element (l_c) (unit: mm)				
	SG1	SG10	SG11	LR3	LR4 / LR5
1	0.667	-	-	-	-
2	0.333	-	-	0.283	-
3	0.250	-	-	0.189	0.383
4	0.167	-	0.508	-	-
5	0.152	-	-	0.113	-
6	-	-	0.302	-	0.192
8	-	0.595	-	-	-
10	0.076	-	-	0.057	-
12	-	-	-	-	0.096
14	-	-	0.145	-	-
16	-	0.297	-	-	0.064
20	0.038	-	0.100	-	-
24	-	-	-	-	0.048
30	-	-	0.068	-	-
32	-	0.147	-	-	-
64	-	0.074	-	-	-

Each of the models identified in table 13 produces a different plastic failure strain, which is not shown. For each material test, this plastic failure strain is divided by the plastic failure strain from the baseline analysis, as shown in equation 18. Then the normalized failure strain values from the varying mesh size models of each material test are assembled into a regularization curve. Figure 43 shows the six regularization curves developed from six material tests using equation 18. Note that because $l_c^{baseline} \cong 0.15$ mm, in figure 43, all of the curves pass through approximately 1.0 at that characteristic length.

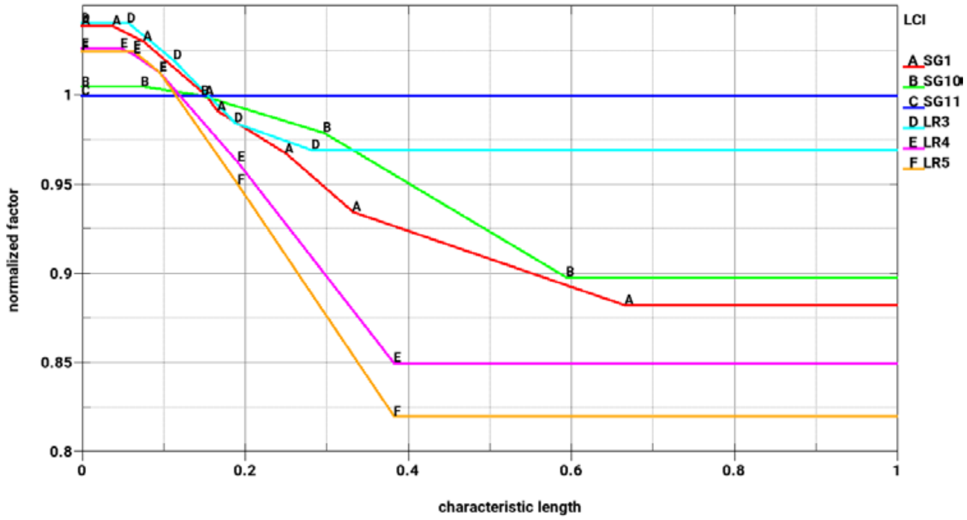

Figure 43. Regularization curves for six material tests, with the normalization factor as a function of characteristic length (mm)

For each state of stress, the regularization curves are different, which demonstrates that the mesh dependency is also influenced by the state of stress. To develop the regularization surface, the curves can be lined up in order of triaxiality or Lode parameter. First, if they are lined up in order of triaxiality, such as SG10 → SG11 → SG1 → LR3 → LR4 → LR5, then the regularization surface developed severely fluctuates without a pattern. Alternately, when they are lined up in order of Lode parameter they can be grouped into three, as LR4 and LR5 (Lode parameter ≅ -1.0), SG11 and LR3 (Lode parameter ≅ 0.0), and SG1 and SG10 (Lode parameter ≅ 1.0). Then, it can be observed that each group's regularization curves have a similar magnitude, and a clear pattern is shown. The least mesh dependency is at Lode parameter ≅ 0.0, but the mesh dependency increases when the Lode parameter is -1.0 or 1.0. The mesh dependency is higher at Lode parameter ≅ -1.0 than at Lode parameter ≅ 1.0. Therefore, it seems that the mesh dependency is more influenced by the Lode parameter than triaxiality. The updated LCI surface shown in figure 44 was developed by selecting one regularization curve in each of the three groups of Lode parameter (LR5, LR3, and SG10).

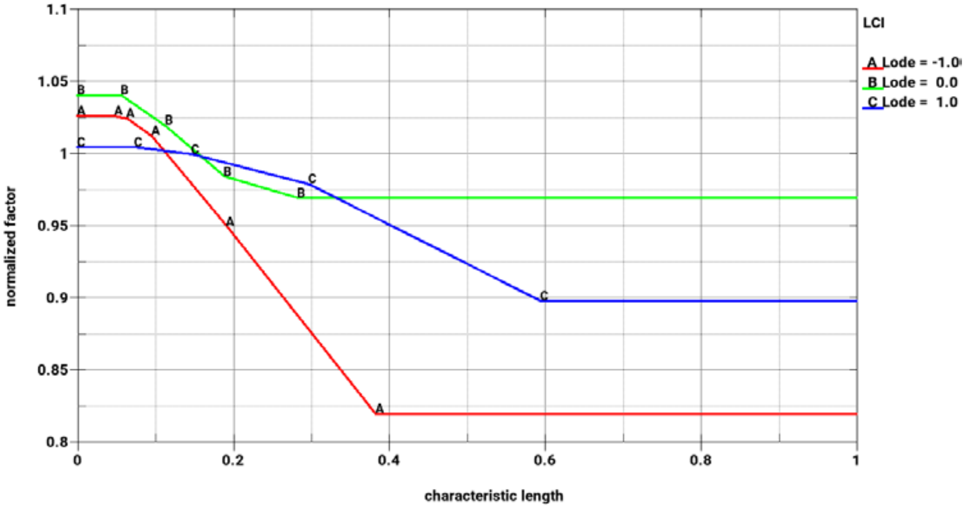

Figure 44. Updated LCI of *MAT_224, with the normalization factor as a function of characteristic length (mm)

The updated LCI was evaluated by using it in the simulations shown in table 13 and comparing the resulting failure strains and the simulation without regularization. Figures 45–50 show the comparisons of simulations with and without regularization. It clearly shows that the updated LCI improves the failure timing in FD curves and torque-angle (TA) curves.

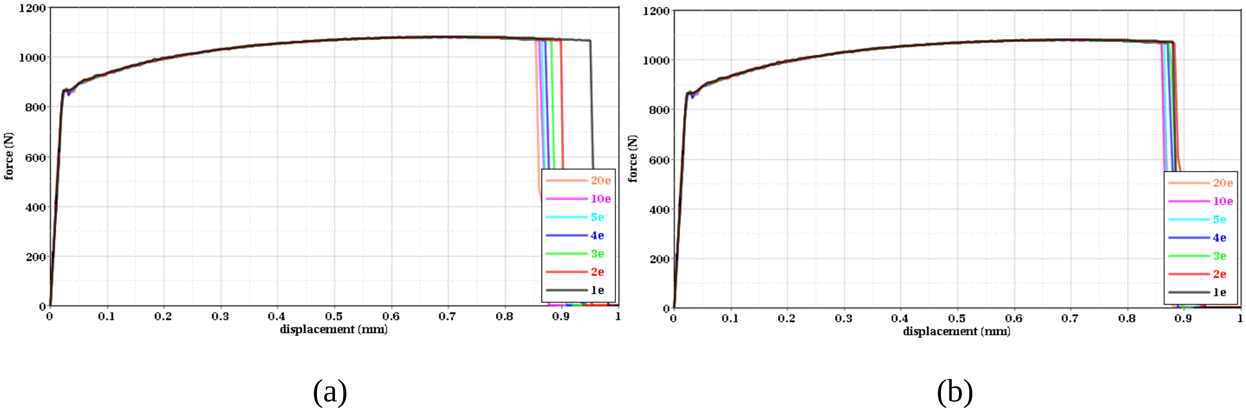

(a)

(b)

Figure 45. FD curves of SG1 simulations with different mesh sizes: (a) without regularization and (b) with regularization

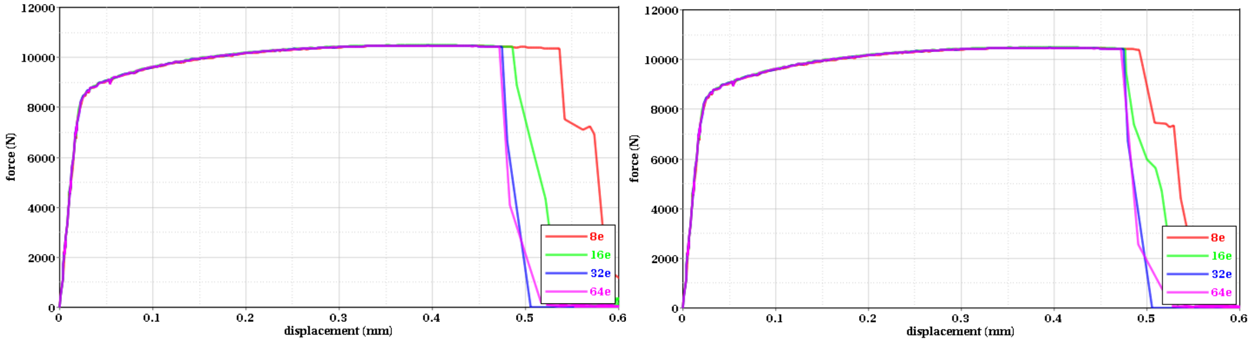

(a) (b)

Figure 46. FD curves of SG10 simulations with different mesh sizes: (a) without regularization and (b) with regularization

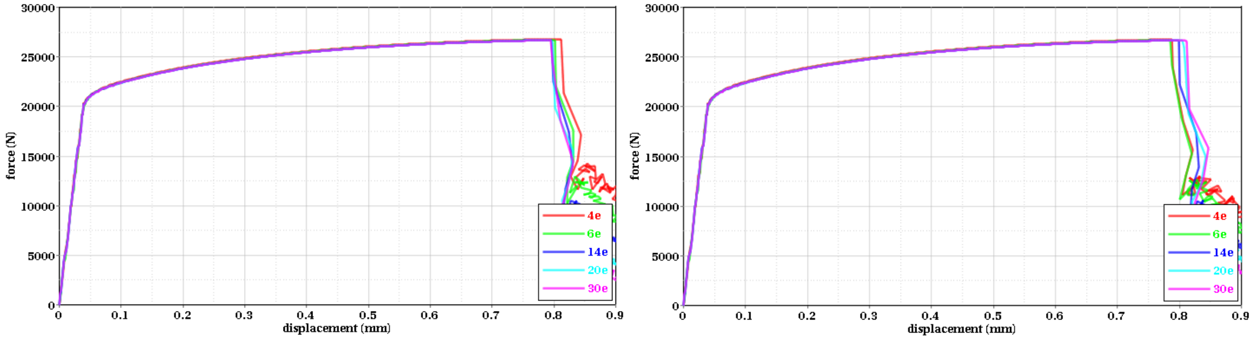

(a) (b)

Figure 47. FD curves of SG11 simulations with different mesh sizes: (a) without regularization and (b) with regularization

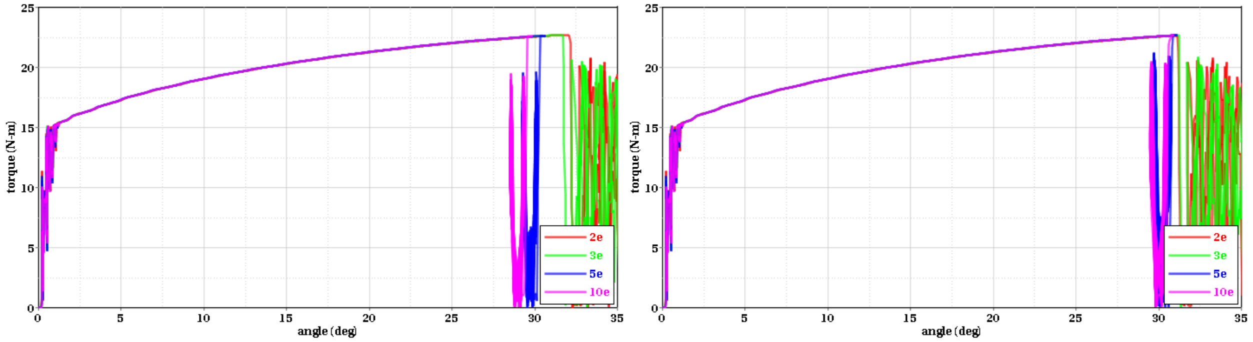

(a) (b)

Figure 48. FD curves of LR3 simulations with different mesh sizes: (a) without regularization and (b) with regularization

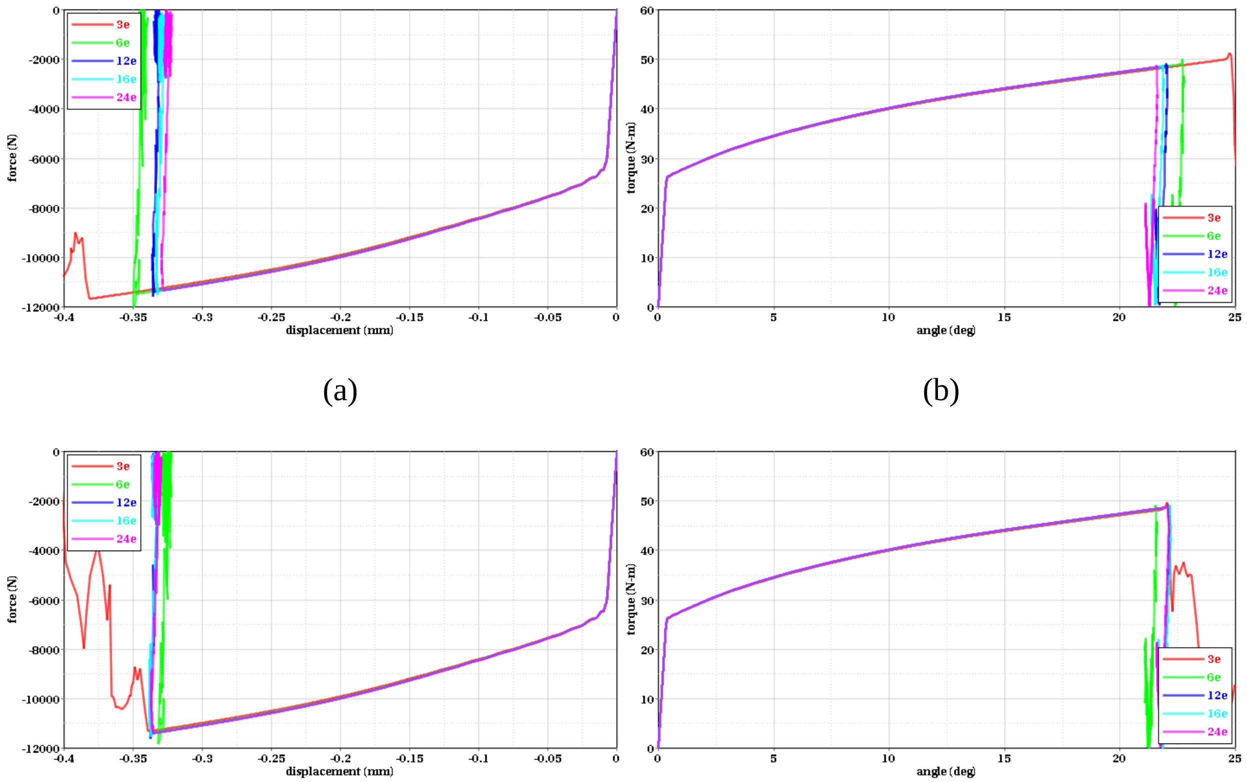

(a) (b)

(c) (d)

Figure 49. FD and TA curves of LR4 simulations with different mesh sizes: (a) FD curves without regularization, (b) TA curves without regularization, (c) FD curves with regularization, and (d) TA curves with regularization

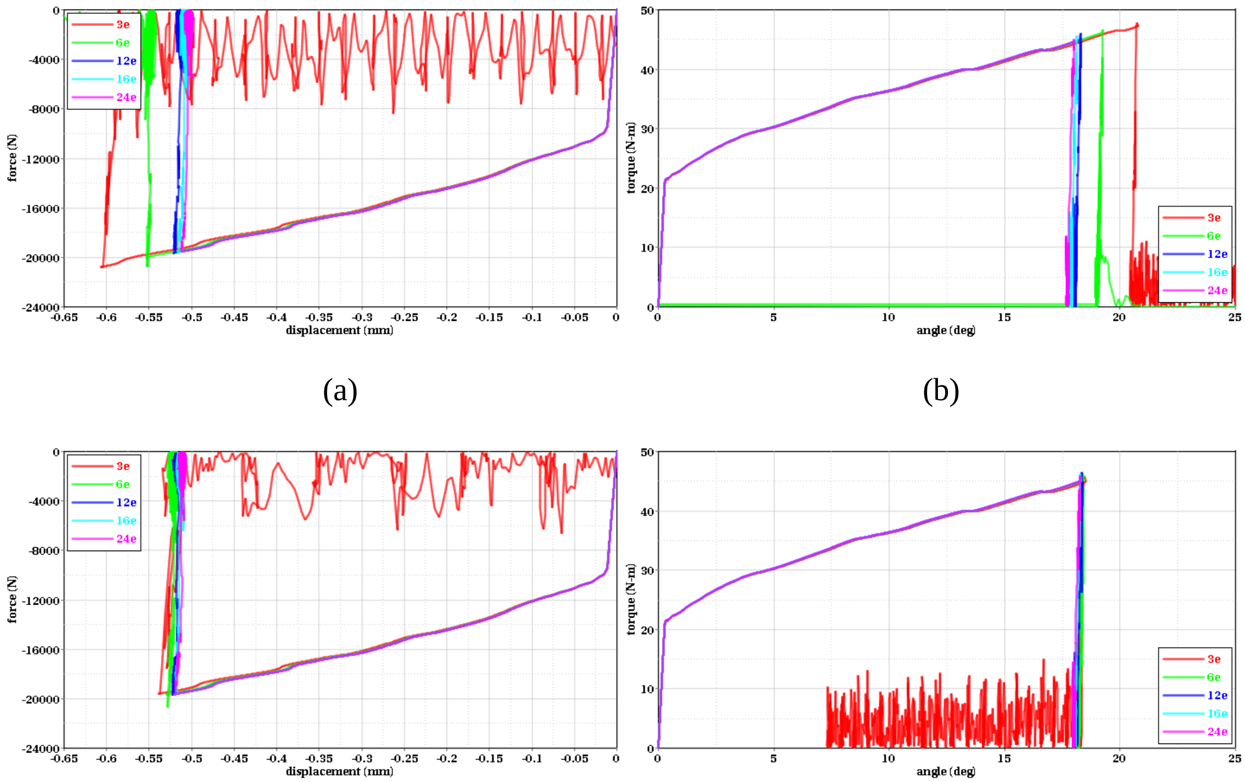

(a) (b)

(c) (d)

Figure 50. FD and TA curves of LR5 simulations with different mesh sizes: (a) FD curves without regularization, (b) TA curves without regularization, (c) FD curves with regularization, and (d) TA curves with regularization

Several cautions must be given, in regards to the regularization, when using the updated Al-2024 model. Note that the bounds of the element sizes in the updated LCI vary between approximately 0.05 mm to 0.5 mm. Use of element sizes outside of this range limit will limit the effectiveness of regularization. For such characteristic lengths, the LCI should be extended for regularization to function, and for element erosion to occur correctly. In addition, element aspect ratios should remain close to 1:1:1 for the characteristic length to adequately characterize the element size. Finally, mesh density must be high enough for the displacement field to be captured accurately (i.e., regularization is not a substitute for a mesh that is so coarse that it fails to converge with respect to the displacement).

5. VALIDATION OF THE UPDATED *MAT_224 OF ALUMINUM 2024 ALLOY

The updated material model of *MAT_224 of Aluminum 2024-T351 alloy described in section 4 was validated by using the ballistic impact tests mentioned in section 3.2. There are two series of the ballistic impact tests to Aluminum 2024 alloy plates: spherical projectile impact tests conducted by UCB [14], and cylindrical projectile impact tests conducted by NASA-GRC [15].

5.1 SPHERICAL PROJECTILE IMPACT TEST SIMULATIONS

In the ballistic impact tests conducted by UCB [14], 12-by-12-inch square Aluminum 2024 alloy plates with three different thicknesses (0.063 inch, 0.125 inch, and 0.25 inch) were impacted by a 0.5-inch diameter chrome steel sphere projectile with various initial impact speeds. The projectile weight was approximately 8.3 grams. Their test results were shown in figure 5(a).

The simulation setup of the sphere impact test is shown in figure 51. A quarter symmetric model is used. The boundary of the plate is fixed because the diameter of the spherical projectile is sufficiently smaller than the size of the plate to ignore boundary effects on the impact. The simulation results are shown in figure 52. It can be observed that the exit velocities of the simulations are very close to the tests. Especially, the critical ballistic velocities for the three different thicknesses of the plates are closely predicted by test simulations.

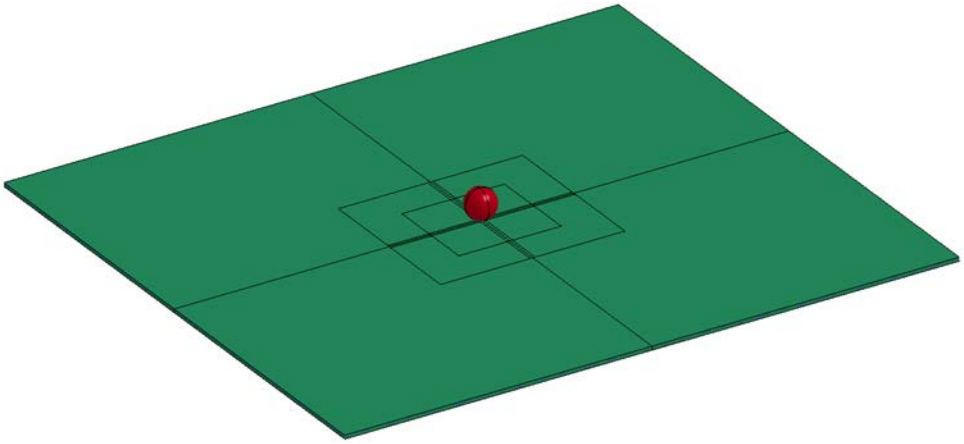

Figure 51. Simulation setup of the sphere impact test

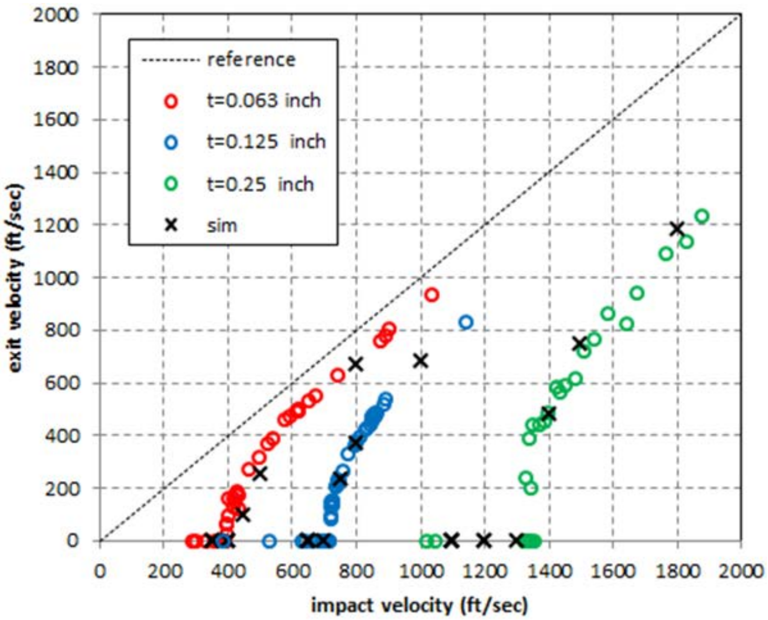

Figure 52. Results of ballistic impact tests with the spherical projectile on three different thickness plates of Aluminum 2024 alloy, and the results of their simulations using the updated material model of *MAT_224

*The ballistic limit of the test results may be estimated by averaging the highest impact velocity that was contained with the lowest impact velocity that was uncontained. The simulation ballistic limits were estimated by fitting the best analytical curve using equation 11. Note that the accuracy of this estimate will be dependent on both the data scatter in the test results and the interval of varying impact velocities in the analysis. Table 14 shows a comparison of the ballistic limit estimates. As can be seen in figure 52, the 13% error listed in table 14, for the 0.063-inch plate, is an overestimate resulting from the simulation impact velocity interval.

Table 14. Summary of ballistic limit velocities of the spherical projectile

		Test ballistic limit velocity (ft/sec)	Sim. ballistic limit velocity (ft/sec)	Error	Test ballistic limit velocity (ft/sec)	Sim. ballistic limit velocity (ft/sec)	Error	Test ballistic limit velocity (ft/sec)	Sim. ballistic limit velocity (ft/sec)	Error
Sphere impact	Plate thickness	0.063 inch			0.125 inch			0.25 inch		
	Comparison	391	440	13%	717	710	-1%	1,327	1,300	-2%

Figure 53 shows the failure shapes at the center of the aluminum plate caused by the spherical projectile impact. The typical failure mechanism is a combination of plugging and petaling in the plates with the thin and intermediate thicknesses (0.063 and 0.125 inches), and mostly plugging in the thick plate (0.25 inch). Similar failure shapes in the simulations are observed, as shown in figure 54.

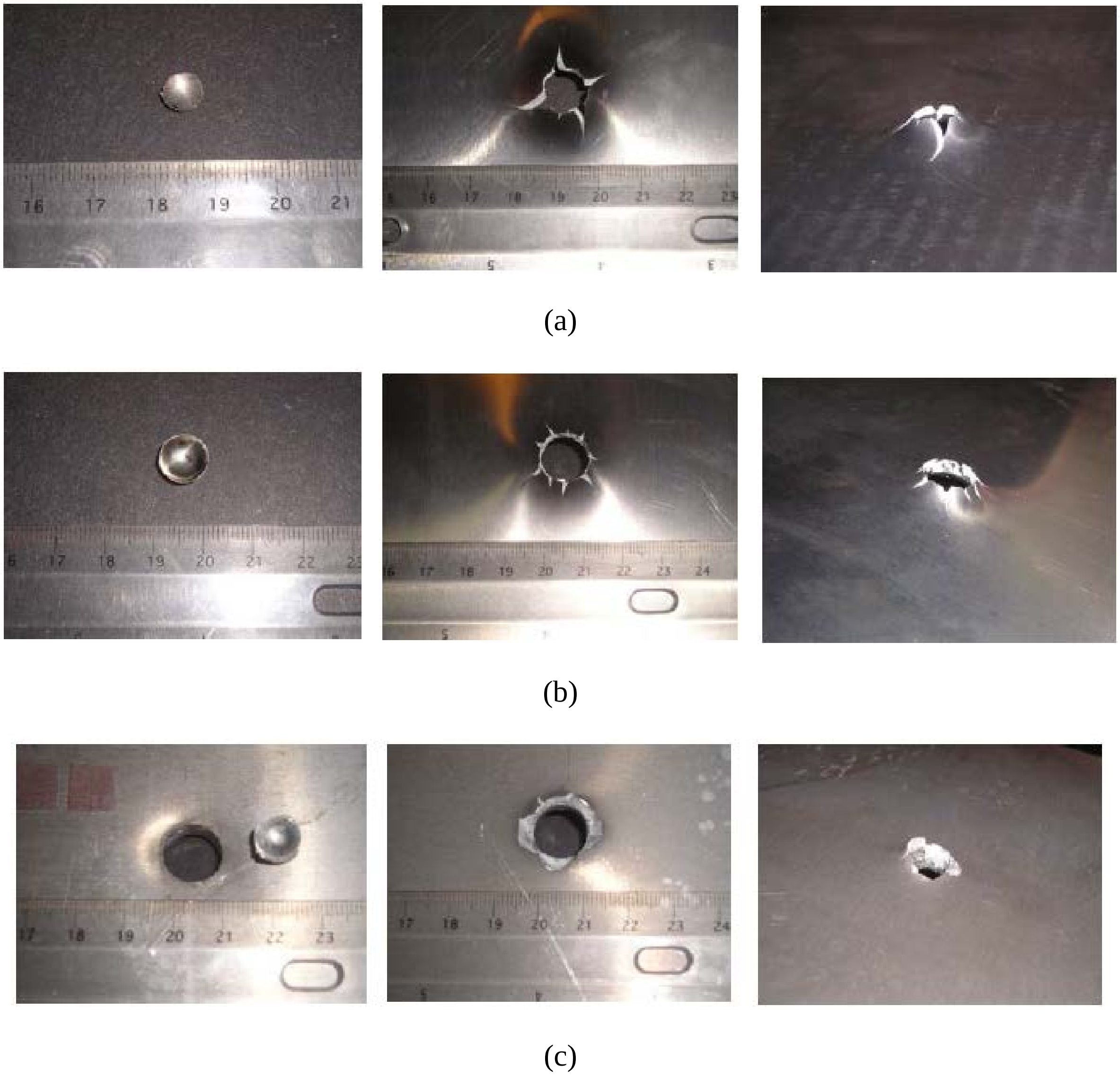

Figure 53. Failure views (front view with plug, back view, and angled back view) of the aluminum plate in the sphere impact tests [14]: (a) plate thickness = 0.063 inch and projectile impact speed = 390 ft/sec, (b) plate thickness = 0.125 inch and projectile impact speed = 724 ft/sec, and (c) plate thickness = 0.25 inch and projectile impact speed = 1,343 ft/sec

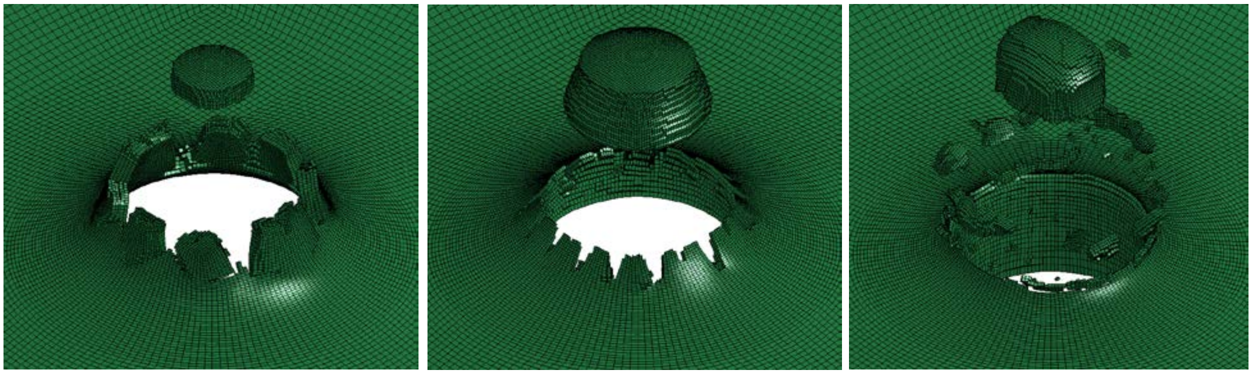

(a) (b) (c)

Figure 54. Failure views of the aluminum plate in the sphere impact simulations: (a) plate thickness = 0.063 inch and projectile impact speed = 450 ft/sec, (b) plate thickness = 0.125 inch and projectile impact speed = 750 ft/sec, and (c) plate thickness = 0.25 inch and projectile impact speed = 1,400 ft/sec

5.2 CYLINDRICAL PROJECTILE IMPACT TEST SIMULATIONS

In the ballistic impact tests conducted by NASA-GRC [15], 10-inch diameter circular Aluminum 2024-T351 alloy plates with three different thicknesses (0.125 inch, 0.25 inch, and 0.5 inch) were impacted by 0.5-inch diameter titanium and steel cylinder projectiles with various initial impact speeds. The projectile weights were approximately 9.9, 12.8, and 28.0 grams for 0.125-, 0.25-, and 0.5-inch target plates, respectively. The projectile materials were titanium for the 0.125- and 0.25-inch target plates, and tool steel for the 0.5-inch target plate. Their test results are shown in figure 5(b).

The simulation setup of the cylinder impact test is shown in figure 55. A quarter symmetric model is used. The boundary of the plate is fixed because the diameter of the cylinder projectile is sufficiently smaller than the size of the plate to ignore boundary effects on the impact. The simulation results are shown in figure 56. It can be observed that the exit velocities in simulations are very close to the tests. Especially, the critical ballistic velocities for three different thicknesses of the plates are closely predicted by test simulations.

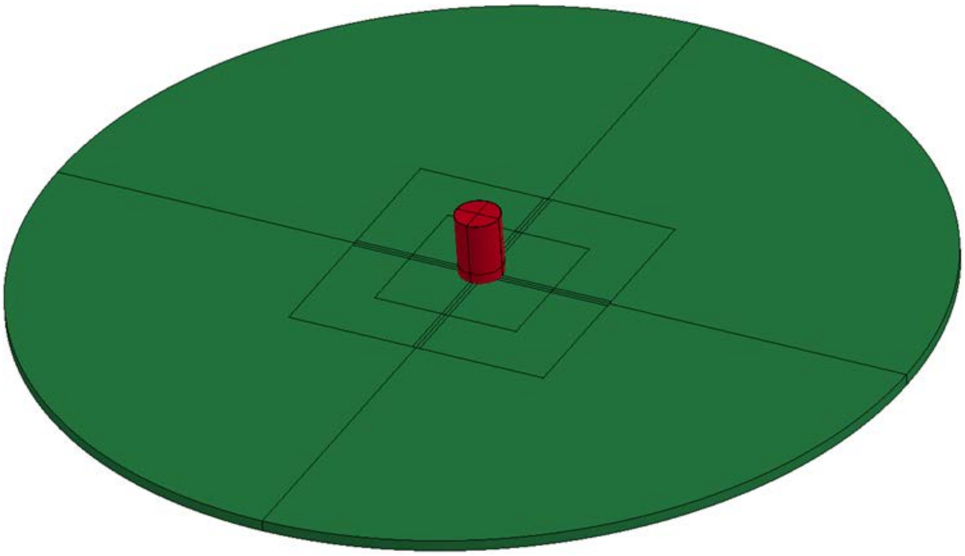

Figure 55. Simulation setup of the cylinder impact test

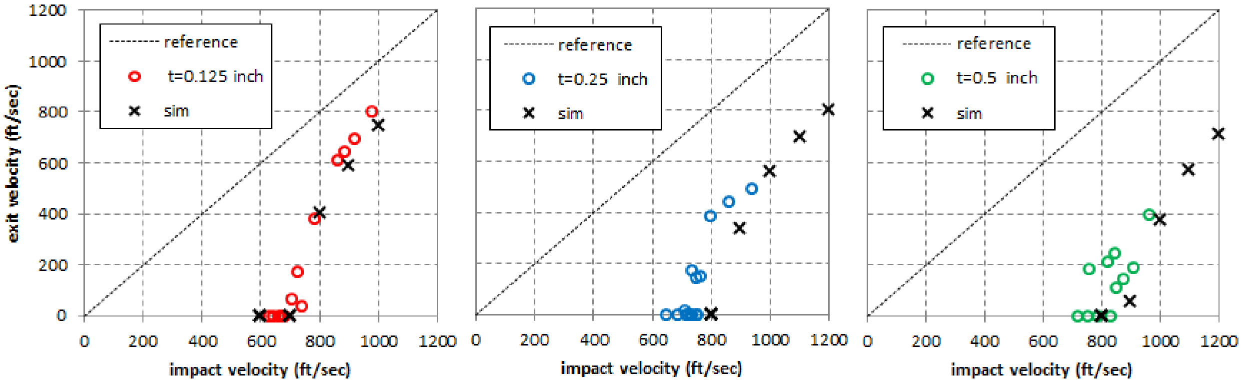

(a) (b) (c)

Figure 56. Results of ballistic impact tests with the cylindrical projectile on three different thickness plates of Aluminum 2024 alloy, and the results of their simulations using the updated material model of *MAT_224: (a) plate thickness = 0.125 inch, (b) plate thickness = 0.25 inch, and (c) plate thickness = 0.5 inch

As with the sphere impacts, the ballistic limit of the results may be estimated by averaging the highest impact velocity that was contained with the lowest impact velocity that was uncontained. The simulation ballistic limits were estimated by fitting the best analytical curve, using equation 11. Table 15 shows a comparison of the ballistic limit estimates. As can be seen in figure 56, the 13% error listed in table 15, for the 0.25-inch plate, shows that the simulation overpredicts the ballistic limit. However, as also can be seen in table 15, the analytical results do overestimate the ballistic limit velocity to some degree. The 7% error listed in table 15, for the 0.5-inch plate, is partially a function of the data scatter in the test results, as shown in figure 56.

Table 15. Summary of ballistic limit velocities of the cylindrical projectile

		Test ballistic limit velocity (ft/sec)	Sim. ballistic limit velocity (ft/sec)	Error	Test ballistic limit velocity (ft/sec)	Sim. ballistic limit velocity (ft/sec)	Error	Test ballistic limit velocity (ft/sec)	Sim. ballistic limit velocity (ft/sec)	Error
Cylinder impact	Plate thickness	0.125 inch			0.25 inch			0.5 inch		
	Comparison	710	740	4%	750	850	13%	840	900	7%

Figure 57 shows the failure modes at the center of the aluminum plate by the cylinder projectile. Plugging is the main failure mode for all three plate thicknesses.

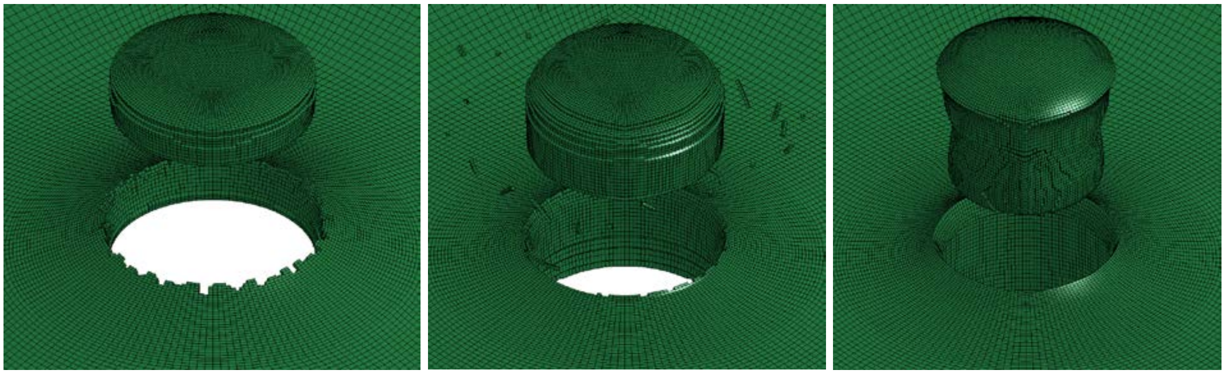

(a) (b) (c)

Figure 57. Failure views of the aluminum plate in the cylinder impact simulations: (a) plate thickness = 0.125 inch and projectile impact speed = 800 ft/sec, (b) plate thickness = 0.25 inch and projectile impact speed = 900 ft/sec, and (c) plate thickness = 0.5 inch and projectile impact speed = 900 ft/sec

However, the plugging failures of the three thickness plates are somewhat different from each other, and the failure occurs under very different states of stress, as shown in figure 58. In the thin plate, the failure starts at the bottom surface caused by bi-axial tension force and propagates upward through thickness. The bi-axial tension failure occurs where triaxiality is approximately -0.66, and Lode parameter is greater than -0.5, as shown in figure 58(a). In the thick plate, the failure is caused by the development of a shear band, which starts at the edge of the impact area on the top surface and propagates downward through thickness. The shear band failure occurs where triaxiality is greater than or equal to zero and Lode parameter is approximately zero, as shown in figure 58(c). In the intermediate plate, shown in figure 58(b), both failure modes occur concurrently or sequentially. First, the shear band failure starts at the top surface, and then the bi-axial tension failure occurs at the bottom surface. The two failures meet at the middle of the thickness. As will be discussed in the next section, the coexistence of two failure modes make this analysis particularly sensitive to mesh density.

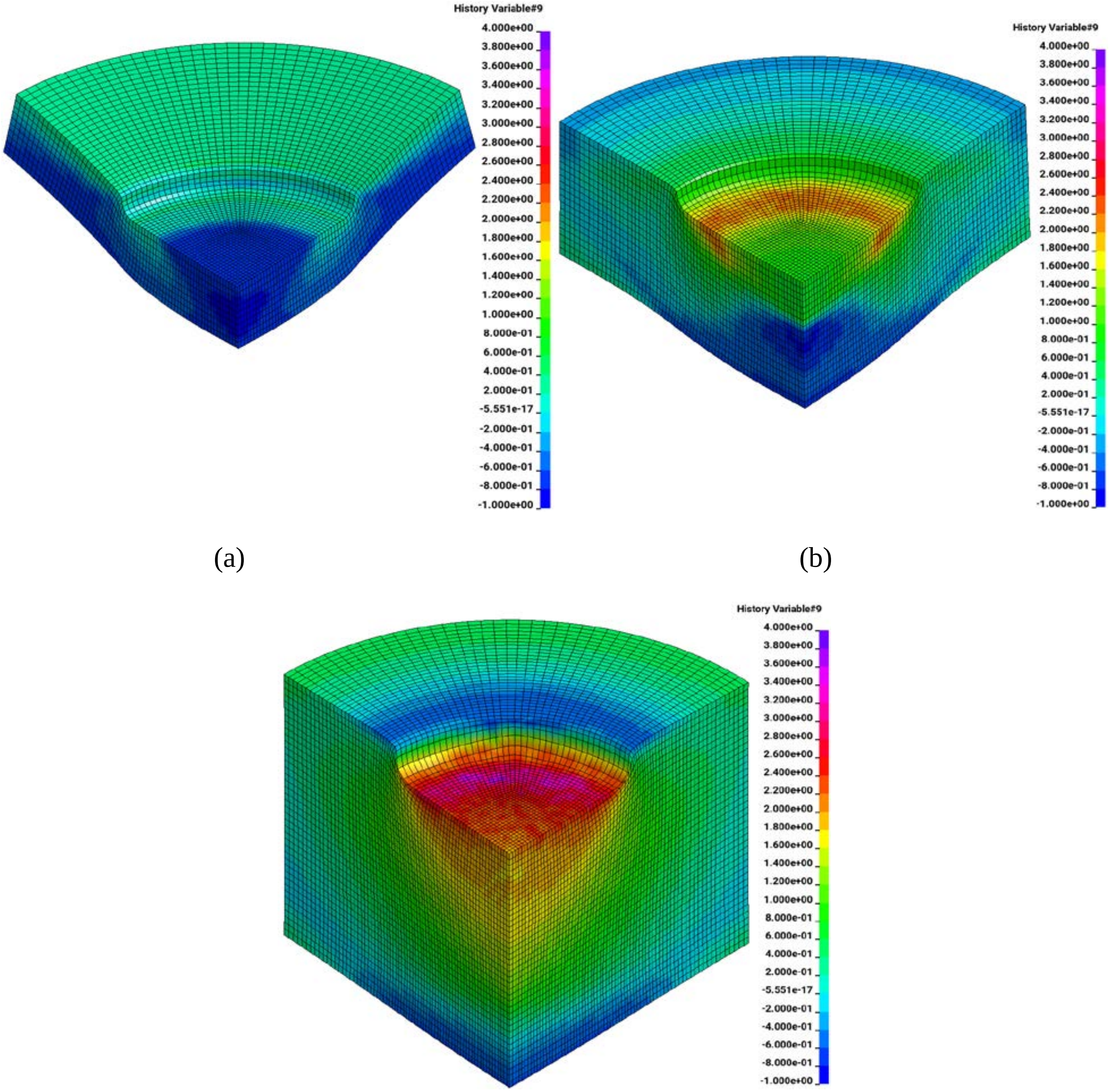

(a) (b)

(c)

Figure 58. Triaxiality contour of the aluminum plate in the cylinder impact simulations right before initial failure: (a) plate thickness = 0.125 inch and projectile impact speed = 800 ft/sec, (b) plate thickness = 0.25 inch and projectile impact speed = 900 ft/sec, and (c) plate thickness = 0.5 inch and projectile impact speed = 900 ft/sec

5.3 REGULARIZATION

The mesh regularization of the updated *MAT_224 for aluminum 2024 alloy is evaluated by simulating the ballistic impact tests using different mesh sizes in the FE models of the aluminum plate. Table 16 summarizes the different meshes, with the element sizes within the approximately 0.05 mm to 0.5 mm bounds of the updated LCI. There is a total of five studied meshes, with different characteristic element lengths at the center of the aluminum plate. Among these five, there are two mesh patterns—rectangular and circular—as shown in figure 59. Mesh-3 is the baseline mesh used for all the simulations shown in sections 5.1 and 5.2. Mesh-1 was not used for the thin plate in the sphere impact simulations because the number of elements through plate thickness was less than five.

Table 16. Summary of mesh sizes of the aluminum plate (RM: regular mesh and CM: circular mesh)

	Characteristic length (l_c) of an element at the center		Aspect ratio (length:height)	Number of elements through plate thickness					
				Sphere impact test			Cylinder impact test		
				Plate thickness (inch)					
	inch	mm		0.063	0.125	0.25	0.125	0.25	0.5
Mesh-1	0.0208 (RM)	0.5304	1:1	-	6	12	6	12	24
Mesh-2	0.0125 (RM)	0.3182	1:1	5	10	20	10	20	40
Mesh-3 (Baseline)	0.0063 (CM)	0.1591	1:2	5	10	20	10	20	40
Mesh-4	0.0063 (CM)	0.1591	1:1	10	20	40	20	40	80
Mesh-5	0.0063 (RM)	0.1591	1:1	10	20	40	20	40	-

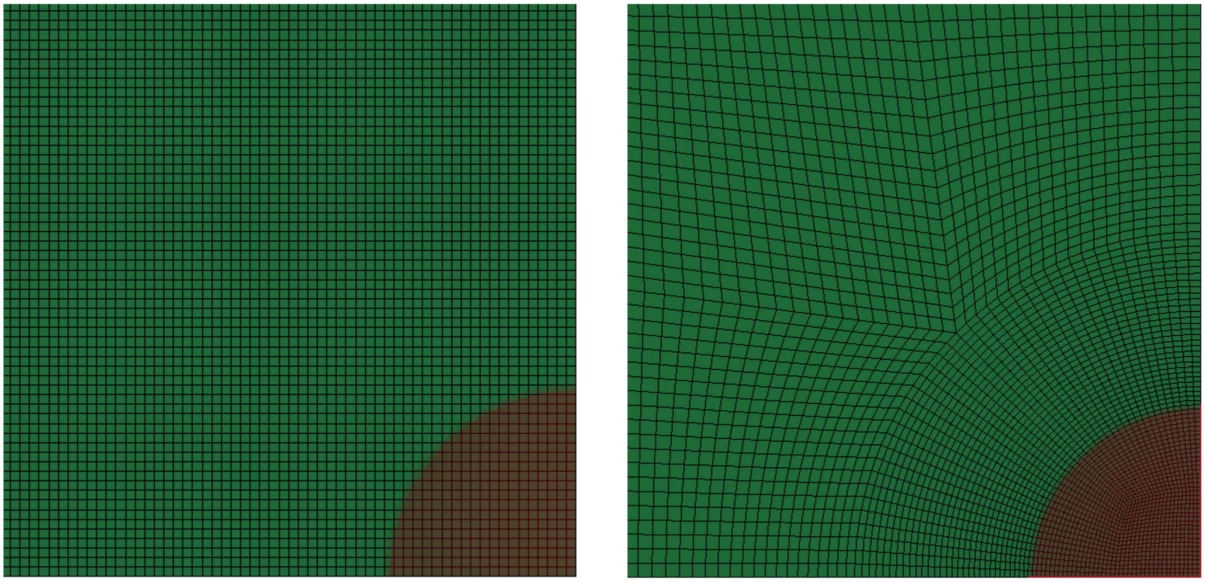

(a) (b)

Figure 59. Mesh patterns of the aluminum plate at the impact area; (a) rectangular mesh (Mesh-2) and (b) circular mesh (Mesh-3)

Figures 60 show the simulation results of the sphere impact simulations when using the different meshes. For the thin (0.063 inch) plate case, the results of Mesh-2, Mesh-4, and Mesh-5 are similar to the result of the baseline (Mesh-3) mesh, with the ballistic limit from Mesh-2 being slightly higher than the baseline. For the intermediate (0.125 inch) plate case, the results of Mesh-1 and Mesh-4 are similar to the results from the baseline (Mesh-3) mesh. The Mesh-2 and Mesh-5 ballistic limit is slightly underpredicted, but it is within a 10% error range. For the thick (0.25 inch) plate case, the results of Mesh-4 are similar to the results of the baseline (Mesh-3) mesh. The ballistic limits using Mesh-1, Mesh-2, and Mesh-5 are underpredicted, whereas the exit velocities are overpredicted. The Mesh-1 predictions differ from than the baseline by more than a 10% error range. However, it should be noted that Mesh-1 is the coarsest mesh with element size approaching the limits of the regularization curves.

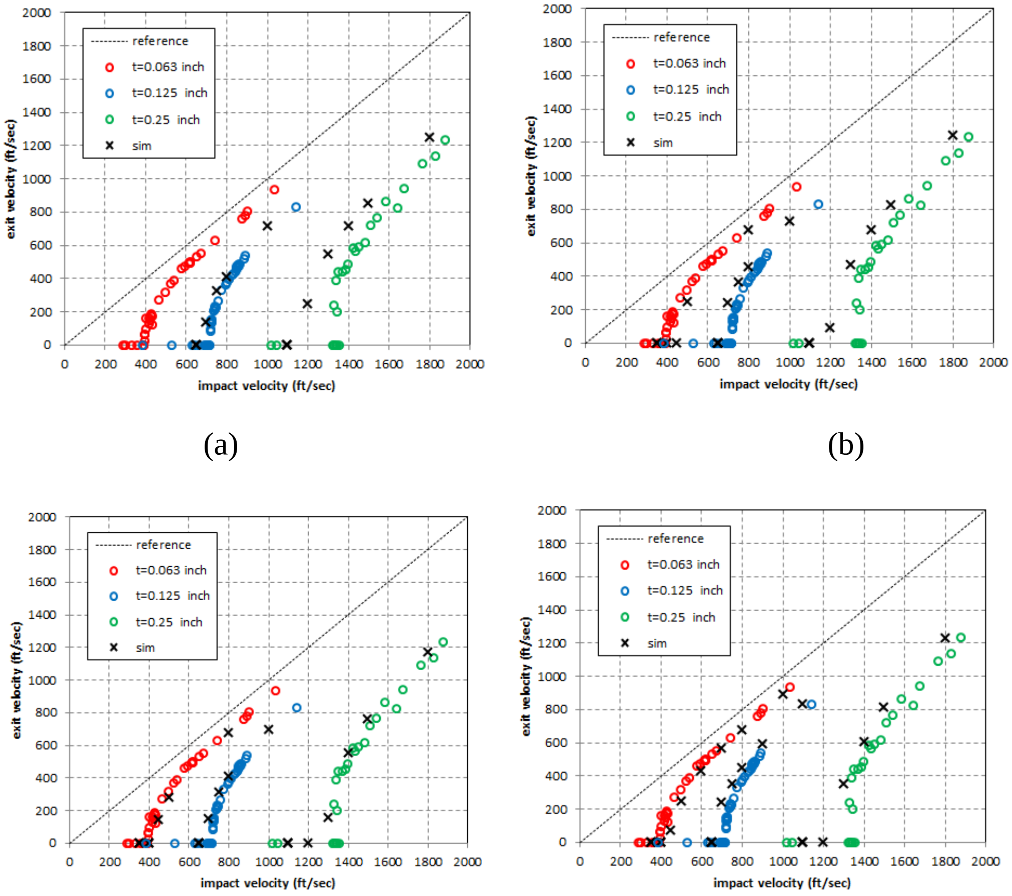

(a)

(b)

(c)

(d)

Figure 60. Results of ballistic impact tests with the sphere projectile to three different thickness plates of Aluminum 2024 alloy and the results of their simulations using the updated material model of *MAT_224 and different meshes: (a) Mesh-1, (b) Mesh-2, (c) Mesh-4, and (d) Mesh-5

Figure 61 shows the sphere projectile impact failure shapes at the center of the aluminum plate with the different meshes. Mostly, the failure shapes are close to the baseline (Mesh-3 shown in figure 54), but the plugs in the thick (0.25 inch) plate cases with Mesh-1, Mesh-2, and Mesh-5 disappear by erosion, which might be the cause of the underpredicted exit velocities shown in figure 60 (a and b).

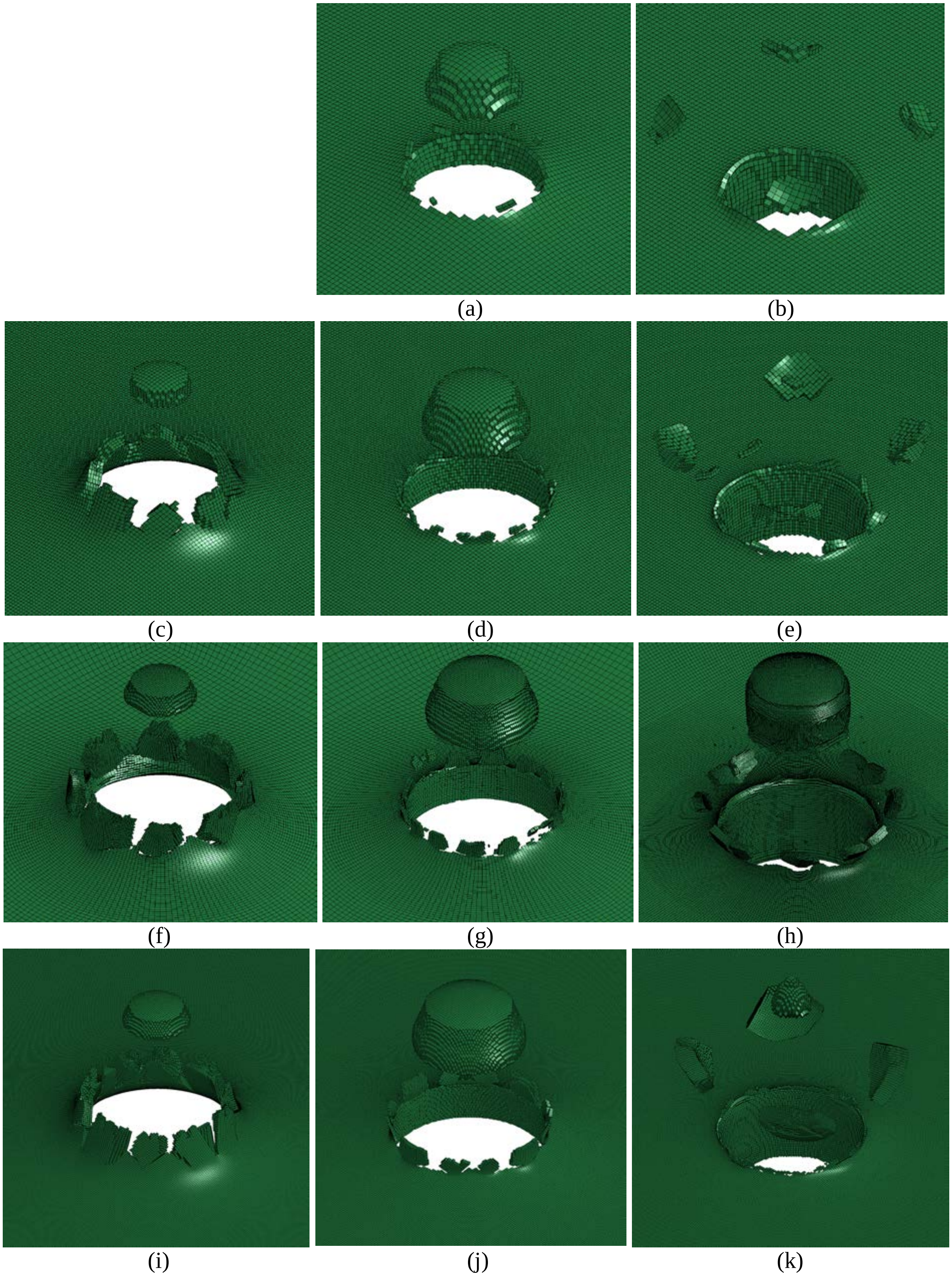

Figure 61. Failure shapes of the aluminum plate in the sphere impact simulations with four different meshes: (a, b) Mesh-1, (c, d, e) Mesh-2, (f, g, h) Mesh-4, (i, j, k) Mesh-5

In figure 61, (a) Mesh-1, plate thickness = 0.125 inch and projectile impact speed = 700 ft/sec, (b) Mesh-1, plate thickness = 0.25 inch and projectile impact speed = 1,200 ft/sec, (c) Mesh-2, plate thickness = 0.063 inch and projectile impact speed = 500 ft/sec, (d) Mesh-2, plate thickness = 0.125 inch and projectile impact speed = 700 ft/sec, (e) Mesh-2, plate thickness = 0.25 inch and projectile impact speed = 1,200 ft/sec, (f) Mesh-4, plate thickness = 0.063 inch and projectile impact speed = 450 ft/sec, (g) Mesh-4, plate thickness = 0.125 inch and projectile impact speed = 700 ft/sec, (h) Mesh-4, plate thickness = 0.25 inch and projectile impact speed = 1,300 ft/sec, (i) Mesh-5, plate thickness = 0.063 inch and projectile impact speed = 450 ft/sec, (j) Mesh-5, plate thickness = 0.125 inch and projectile impact speed = 700 ft/sec, and (k) Mesh-5, plate thickness = 0.25 inch and projectile impact speed = 1,300 ft/sec.

For the sphere projectile impacts, the finer element meshes (Mesh-3, Mesh-4, and Mesh-5) give good matching results to the test, and the larger element meshes (Mesh-1 and Mesh-2) underpredict the exit velocities. Additionally, the FE models of the thicker plate sphere impact simulations show more mesh size dependency, even if mesh regularization is used, as in *MAT_224.

Figures 62–63 show the simulation results of the cylinder impact simulations when using the different meshes. For the thin (0.125 inch) plate case, the results of Mesh-2, Mesh-4, and Mesh-5 are similar to the result of the baseline (Mesh-3) mesh. Mesh-1 overpredicts the ballistic limit and underpredicts the exit velocity of the cylindrical projectile, but it is within a 10% error range. For the intermediate (0.25 inch) plate case, all the different meshes (Mesh-1, Mesh-2, Mesh-4, and Mesh-5) overpredict the ballistic limits by more than a 10% error range. For the thick (0.5 inch) plate case, the result of Mesh-4 is similar to the result of the baseline (Mesh-3) mesh. The ballistic limits from Mesh-1 and Mesh-2 overpredict the test by more than a 10% error range.

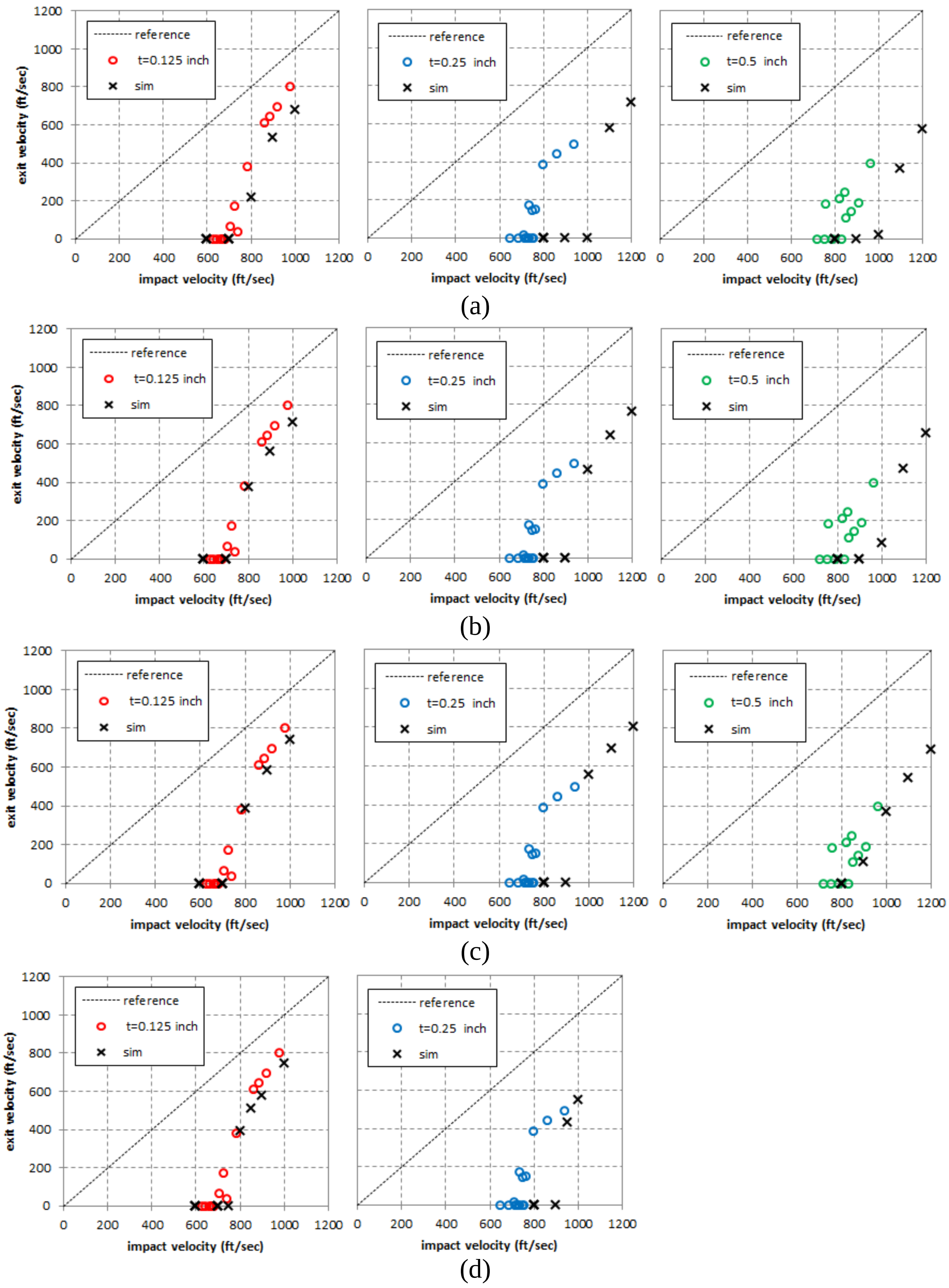

(a)

(b)

(c)

(d)

Figure 62. Results of ballistic impact tests with the cylinder projectile to three different thickness plates of Aluminum 2024 alloy and the results of their simulations using the updated material model of *MAT_224 and different meshes: (a) Mesh-1, (b) Mesh-2, (c) Mesh-4, and (d) Mesh-5

Figure 63 shows the failure shapes at the center of the aluminum plate by the cylinder projectile with different meshes. Mostly, the failure shapes are close to the baseline (Mesh-3 shown in figure 57), but the plugs in the thick plate cases with Mesh-1 and Mesh-2 have some erosion at their top and bottom surfaces.

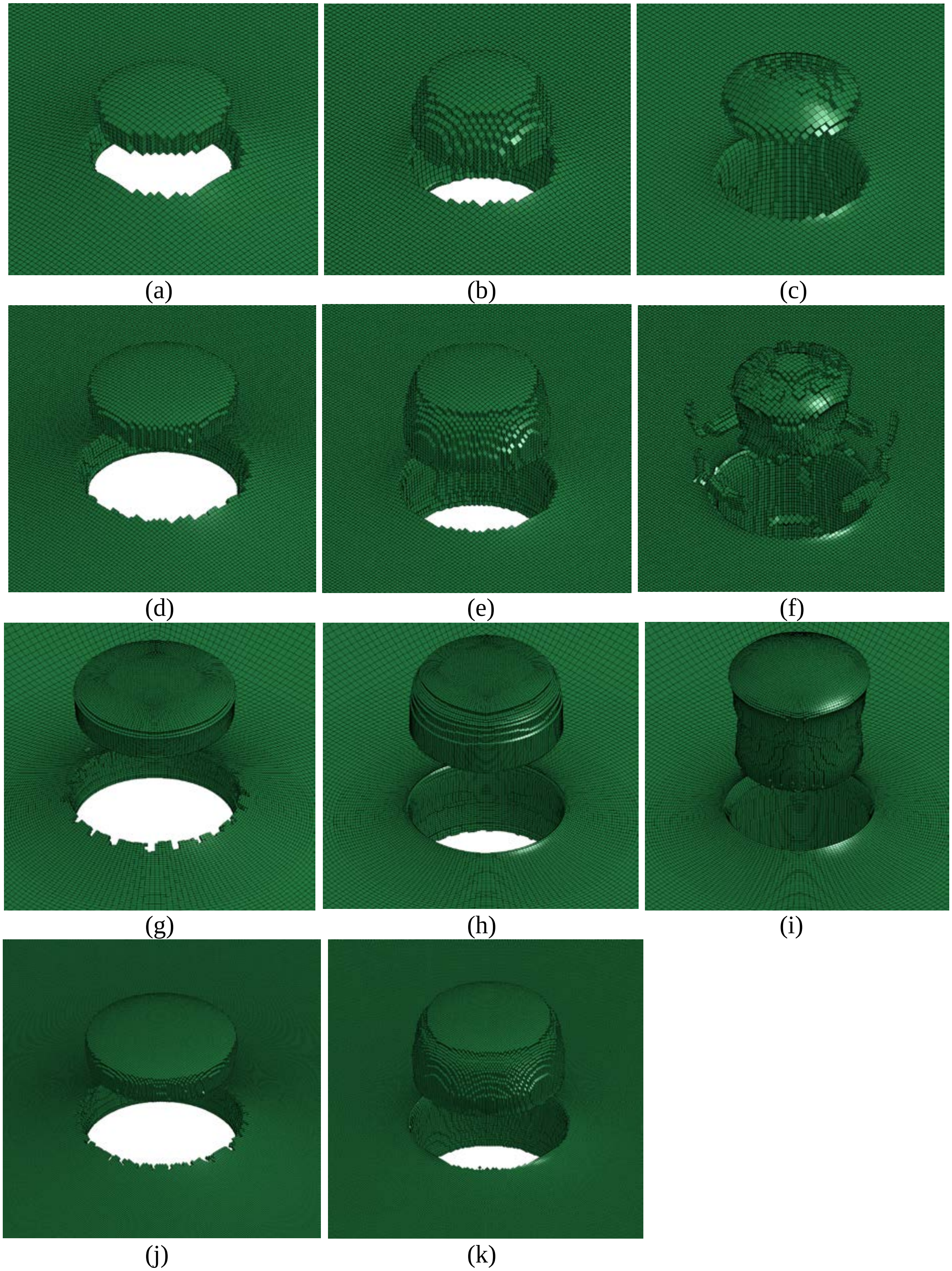

(a) (b) (c)

(d) (e) (f)

(g) (h) (i)

(j) (k)

Figure 63. Failure views of the aluminum plate in the cylinder impact simulations with three different meshes: (a, b) Mesh-1, (c, d, e) Mesh-2, (g, h, i) Mesh-4, (j, k) Mesh-5

In figure 63, (a) Mesh-1, plate thickness = 0.125 inch and projectile impact speed = 800 ft/sec, (b) Mesh-1, plate thickness = 0.25 inch and projectile impact speed = 1,100 ft/sec, (c) Mesh-1, plate thickness = 0.5 inch and projectile impact speed = 1,000 ft/sec, (d) Mesh-2, plate thickness = 0.125 inch and projectile impact speed = 800 ft/sec, (e) Mesh-2, plate thickness = 0.25 inch and projectile impact speed = 1,000 ft/sec, (f) Mesh-2, plate thickness = 0.5 inch and projectile impact speed = 1,000 ft/sec, (g) Mesh-4, plate thickness = 0.125 inch and projectile impact speed = 800 ft/sec, (h) Mesh-4, plate thickness = 0.25 inch and projectile impact speed = 1,000 ft/sec, (i) Mesh-4, plate thickness = 0.5 inch and projectile impact speed = 900 ft/sec, (j) Mesh-5, plate thickness = 0.125 inch and projectile impact speed = 800 ft/sec, and (k) Mesh-5, plate thickness = 0.25 inch and projectile impact speed = 950 ft/sec.

For the cylinder projectile impacts, the finer meshes (Mesh-3, Mesh-4, and Mesh-5) give good matching results to the test in thin and thick plate cases, and the larger meshes (Mesh-1 and Mesh-2) overpredict the ballistic limits. As in the sphere impacts, the FE models of the thicker plate in the cylinder impact simulations show more mesh size dependency even if the *MAT_224 mesh regularization is defined. As introduced in the previous section, the results show that the FE model of the intermediate plate in the cylinder impact simulations is especially sensitive to mesh size, because of the complicated failure mode. The estimates for the ballistic limits for all of the impact tests and meshes, including both sphere and cylinder projectiles, are given in table 17.

Table 17. Summary of ballistic limit velocities of a projectile with using different meshes

		Test ballistic limit velocity (ft/sec)	Sim. ballistic limit velocity (ft/sec)	Error	Test ballistic limit velocity (ft/sec)	Sim. ballistic limit velocity (ft/sec)	Error	Test ballistic limit velocity (ft/sec)	Sim. ballistic limit velocity (ft/sec)	Error
Sphere impact	Plate thickness	0.063 inch			0.125 inch			0.25 inch		
	Mesh-1	391	-	-	717	685	-4%	1,327	1,170	-12%
	Mesh-2		450	15%		650	-9%		1,195	-10%
	Mesh-3 (Baseline)		440	13%		710	-1%		1,300	-2%
	Mesh-4		430	10%		680	-5%		1,290	-3%
	Mesh-5		440	13%		660	-8%		1,250	-6%
Cylinder impact	Plate thickness	0.125 inch			0.25 inch			0.5 inch		
	Mesh-1	710	790	11%	750	1,000	33%	840	1,000	19%
	Mesh-2		750	6%		900	20%		1,000	19%
	Mesh-3 (Baseline)		740	4%		850	13%		900	7%
	Mesh-4		750	6%		900	20%		900	7%
	Mesh-5		750	6%		900	20%		-	-

In summary, the *MAT_224 mesh regularization clearly helps mitigating the mesh sensitivity of simulations. However, if the mesh is not sufficiently dense to accurately represent the state of deformation, and the physical material failure behavior, then the regularization cannot make up for that deficiency. As discussed in section 4.7, regularization is not a substitute for a mesh that is too coarse for the displacement field to have converged.

There are additional limitations to regularization. In finite elements, element erosion necessarily follows the mesh pattern. This is an inherent problem with Lagrangian finite elements. Unfortunately, regularization only partially helps mitigate this problem. In addition, mesh density and mesh sensitivity are also somewhat linked to the size of the part being modeled. It is not possible to include this link in a material law, which means that a regularization curve is somewhat linked to a class of applications. Additionally, regularization as currently implemented only adjusts the failure strain based on mesh size, not the post-necking plasticity that may also be mesh-size dependent. Therefore, the energy absorption at failure may also be somewhat mesh-dependent.

6. CONCLUSIONS

This report documented the development of the updated *MAT_224 input parameters for an Aluminum 2024-T351 alloy for ballistic impact simulations using LS-DYNA. In the development process, additional material tests were conducted and improved test measurement techniques were adopted. The updated material model was validated by the series of ballistic impact tests. Overall, the ballistic impact simulations using the updated material model of *MAT_224 of the Aluminum 2024-T351 alloy show a relatively good match to the tests.

It has been shown that using a well-constructed failure surface (LCF) in *MAT_224 is critical in simulating the ballistic impact tests accurately. This report also shows that utilizing more material test point data provides a better-constructed LCF. Additional study shows that the regularization (LCI) in *MAT_224 helps mitigate the mesh sensitivity of simulations. However, the mesh still needs to be sufficiently dense to accurately represent the displacement field and the physical material failure behavior.

There are three future tasks recommended for further improvement to the Aluminum 2024-T351 input parameters. First, the Taylor-Quinney coefficient (Beta), which is currently a constant, should be updated based on ongoing research at OSU. This research, using an IR camera, will provide a more direct and accurate measurement of Beta. Beta may be dependent on strain rate and strain, and can be modeled as such using *MAT_224. Second, the LCF needs to be improved further using additional material tests. These additional tests should be designed to determine failure strains at stress states that are currently unknown. These stress states, for which failure strains are currently unknown, include both lower triaxiality tension and higher triaxiality compression. Finally, the Aluminum 2024-T351 alloy exhibited some anisotropic behavior [6]. Modeling this behavior will require using *MAT_264, the anisotropic version of *MAT_224.

7. REFERENCES

1. FAA Report. (2014). Development of a new metal material model in LS-DYNA Part 1: FAA, NASA, and industry collaboration background. (DOT/FAA/TC-13/25, P1).

2. FAA Report. (2007). Statistical testing and material model characterization of aluminum and titanium for transport airplane rotor burst fragment shielding. (DOT/FAA/AR-07/26).

3. FAA Report. (2008). Impact tests of aircraft aluminums and composites for uncontained engine fragment modeling. (DOT/FAA/AR-08/46).

4. FAA Report. (2014). Development of a new metal material model in LS-DYNA Part 2: Development of a tabulated thermo-viscoplastic material model with regularized failure for dynamic ductile failure prediction of structures under impact loading. (DOT/FAA/TC-13/25, P2).

5. Livermore Software Technology Corporation, (2017). *LS_DYNA Keyword User's Manual, Volume I and II, Version R10.0,* Livermore, California: LSTC.

6. FAA Report. (2014). Development of a new metal material model in LS-DYNA Part 3: Plastic deformation and ductile fracture of 2024 aluminum under various loading conditions. (DOT/FAA/TC-13/25, P3).

7. FAA Report. (2016). Development of a titanium alloy Ti-6Al-4V material model used in LS-DYNA. (DOT/FAA/TC-15/23).

8. Dolci, S., Carney, K., Wang, L., Kan, C.D., and Du Bois, P. (2016). *Incorporation of inconel-718 material test data into material model input parameters for *MAT_224,* 14th International LS-DYNA Users Conference, Dearborn, MI.

9. FAA Report. (2016). An anisotropic and asymmetric material model for simulation of metals under dynamic loading. (DOT/FAA/TC-TT16/44).

10. Wang, L., Haight, S., Carney, K., Du Bois, P., Kan, C.D., Dicecca, F., and Emmerling, W. (2016). *Test and simulation comparison using titanium material models based on *MAT_224,* 14th International LS-DYNA Users Conference, Dearborn, MI.

11. FAA Report. (2014). Plastic deformation and ductile fracture of Ti-6Al-4V under various loading conditions. (DOT/FAA/TC-TT14/2).

12. Lowe, R.L., Seidt, J.D., and Gilat, A. (2016). *Characterization of the Lode = -1 meridian on the Al-2024 failure surface for *MAT_224 in LS-DYNA*, 14th International LS-DYNA Users Conference, Dearborn, MI.

13. Seidt, J.D., Kuokkala, V-T., Smith, J.L., and Gilat, A. (2017). Synchronous full-field strain and temperature measurement in tensile tests at low, intermediate and high strain rates. *Experimental Mechanics, 57*(2), 219–229.

14. FAA Report. (2006). Statistical testing of aircraft materials for transport airplane rotor burst fragment shielding. (DOT/FAA/AR-06/9).

15. NASA/FAA Report. (2013). Impact testing of aluminum 2024 and titanium 6Al-4V for material model development. (NASA/TM–2013-217869; DOT/FAA/TC–12/58).

16. Recht, R.F., and Ipson, T.W. (1963). Ballistic perforation dynamics. *Journal of Applied Mechanics, 30*(3), 384–390.

17. Børvik, T., Hopperstad, O.S., and Pedersen, K.O. (2010). Quasi-brittle fracture during structural impact of AA7075-T651 aluminium plates. *International Journal of Impact Engineering*, *37*(5), 537–551.

18. Z. Rosenberg, Z., and Dekel, E. (2012). *Terminal Ballistics*, New York, NY: Springer.

19. Carney, K., Pereira, M., Revilock, D., and Matheny, P. (2009). Jet engine fan blade containment using an alternate geometry and the effect of very high strain rate material behavior. *International Journal of Impact Engineering, 36*(5), 720–728.

20. Ravichandran, G., Rosakis, A.J., Hodowany, J., and Rosakis, P. (2002). On the conversion of plastic work into heat during high-strain-rate deformation. *AIP Conference Proceedings, 620*(1), 557–562.

21. Johnson, G.R., and Cook, W.H. (1985). Fracture characteristics of three metals subjected to various strains, strain rates, temperatures and pressures. *Engineering Fracture Mechanics, 21*(1), 31–48.

22. Livermore Software Technology Corporation (2018). *LS_DYNA Theory Manual*, Livermore, California: LSTC.

APPENDIX A—DESCRIPTION OF NEW PUNCH TEST SERIES

A sphere punch test was designed to initiate bi-axial tension failure at the bottom of a specimen plate. The stress state is bi-axial tension with a Lode parameter equal to -1.0, and the triaxiality varies with the stress in the thickness direction of the plate. If there is no stress along the thickness direction of the plate, then it is the plane stress condition, and the triaxiality is equal to -2/3. If there is negative (compression) stress in the thickness direction of the plate, then the triaxiality is in the range between -2/3 and 1/3. Creating negative stress requires a backing plate below the specimen plate, which causes the compression stress in the thickness direction. The level of the compression stress along the thickness direction of the specimen plate is dependent on the material and thickness of the backing plate.

The new punch test series has three tests: (unbacked, thin-backed, and thick-backed) for the three different states of stress at the initial failure point of the specimen plate. The punch has a spherical shape. The size of the punch is much smaller than the diameter of the plate to remove any boundary effects. The material of the backing plate is copper. The test setup is shown in figure A-1 and the dimension of test components is summarized in table A-1.

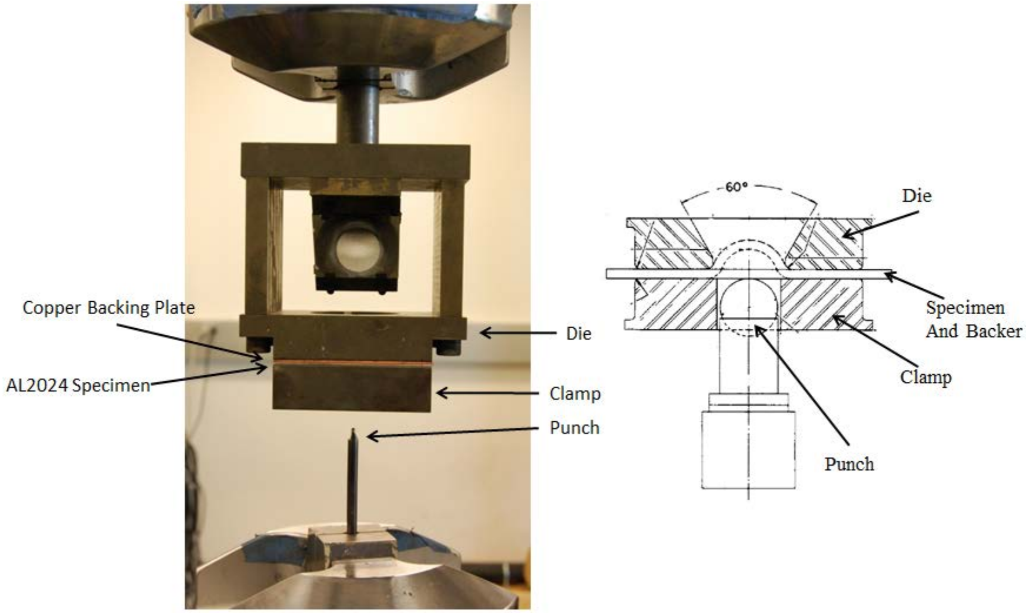

Figure A-1. Setup of new punch tests

Table A-1. Dimension of aluminum specimen plates, copper backing plates, punches, and fixture components

Case	Specimen Thickness (mm)	Backing Plate Thickness (mm)	Punch Diameter (mm)	Clamp Diameter (mm)	Die Diameter (mm)
Unbacked	1.27	N/A	2.3	47.625	50.8
Thin-backed	0.635	1.27		25.4	28.575
Thick-backed		2.54	1.6		

APPENDIX B—DEVELOPING PROCESS OF A MATERIAL CURVE FROM A MATERIAL TENSILE TEST

In general, a material tensile test provides a force-displacement (FD) curve from a test machine. Then, engineering stress σ_{eng} and engineering strain ε_{eng} can be derived by

$$\sigma_{eng}(t) = F(t)/A_0,\ \ \varepsilon_{eng}(t) = [L(t) - L_0]/L_0, \tag{B-1}$$

where $F(t)$ is the force in time t from the machine, A_0 is the original cross-sectional area of the specimen, $L(t)$ is the instantaneous gauge length in time, and L_0 is the original gauge length. Additionally, they can be converted to true stress σ and true strain ε as:

$$\sigma = \sigma_{eng}(1 + \varepsilon_{eng}),\ \ \varepsilon = \ln(1 + \varepsilon_{eng}). \tag{B-2}$$

For the *MAT_224, the strain needs to be converted to the plastic strain ε_p expressed as:

$$\varepsilon_p = \varepsilon - \sigma/E, \tag{B-3}$$

where E is the elastic modulus.

However, the simulation of the tensile test with the stress versus plastic strain input curve cannot generate the FD curve, which matches with the FD curve recorded from the tensile test machine. This is because the original cross-sectional area and gauge length of the specimen are varied after the necking in the specimen occurs, and then equation (B-2) is an approximation. Therefore, the (SS) input curve of the *MAT_224 needs to be developed by a reverse process, which is described here below.

The reverse process to generate the input of the *MAT_224 requires two inputs: a FD curve from a test machine and an SS curve from a DIC analysis. The procedure is as follows:

1. Convert the engineering SS curve to true SS curve by using equation B.2.

2. Find a yield point in the true stress versus true strain curve by using the elastic modulus and 0.2% strain offset, then convert the true strain to the plastic strain using equation B.3 to obtain the stress versus plastic strain curve.

3. Find a necking point using the relationship:

   $$\sigma(\varepsilon) = d\sigma(\varepsilon)/d\varepsilon \tag{B-4}$$

   which describes that necking occurs at the true stress is equal to the tangent modulus. Then, take the stress versus plastic strain curve before necking as the input of the *MAT_224. The curve after necking is defined in the next step.

4. Define the trial input curves after necking. The hardening curve of a metal is commonly expressed by a power-law equation as:

$$\sigma = k\varepsilon_p^n, \text{ where } k = \sigma_{necking}/\varepsilon_{necking}^n, \tag{B-5}$$

and where the exponent *n* is varied to generate the trial input curves after necking. The complete input curves are generated by combining the curves of before and after necking.

5. Repeat the tensile test simulations using trial input curves to find the FD curve of a simulation close to the test FD curve. If two FD curves of the simulation and test diverge at a certain point after necking, keep the input curve before the certain point and go back to steps 4 and 5. Repeat the process until the complete matching FD curve of the simulation up to a failure point is generated. After the failure point, the input curve is extrapolated until the plastic strain reaches unity.

APPENDIX C—DESCRIPTION OF THE STATE OF STRESS IN TRIAXIALITY AND LODE PARAMETER USING MOHR’S CIRCLES

Mohr’s circles for a three-dimensional state of stress are shown in figure C-1. Mohr’s circles can be identified in the plane of triaxiality and Lode parameter as shown in figure C-2. They give better insight and understanding into the relationship between the state of stress, and the triaxiality and Lode parameter.

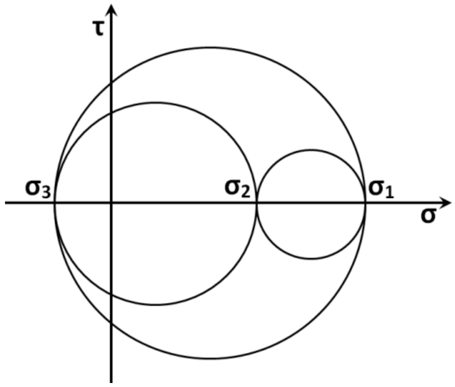

Figure C-1. Mohr's circles of a three-dimensional state of stress in the σ-τ coordinate system

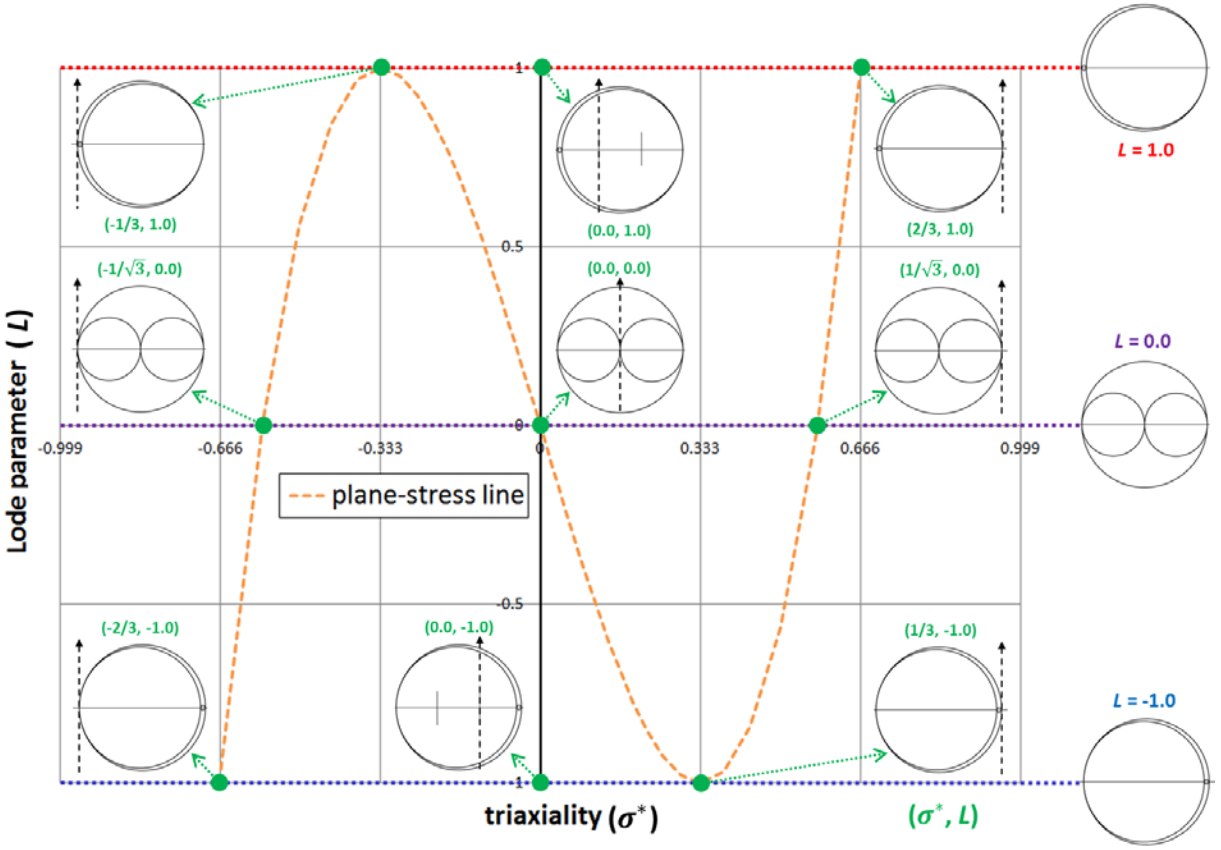

Figure C-2. Mohr's circles in the plane of triaxiality and Lode parameter

The triaxiality is the location of the Mohr's circles in the σ-τ coordinate system.

- If the triaxiality is smaller than the leftmost plane-stress line, then Mohr's circles are located at the right side of the τ-axis, which means that all the states of stress are tension.
- If triaxiality is between the leftmost and the rightmost plane-stress lines, then Mohr's circles are located on the τ-axis, which means that the states of stress are combined with both tension and compression.
- If triaxiality is bigger than the rightmost plane-stress line, then Mohr's circles are located at the left side of the τ-axis, which means that all the states of stress are compression.

The Load parameter is the location of σ_2 between σ_1 and σ_3 in the Mohr's circles.

- If Lode parameter = 1.0, then $\sigma_2 = \sigma_3$.
- If Lode parameter = 0.0, then $\sigma_2 = (\sigma_3 + \sigma_1)/2$.
- If Lode parameter = -1.0, then $\sigma_2 = \sigma_1$.

APPENDIX D—THEORETICAL FAILURE STRAIN SURFACES

The failure strain surface (LCF) developed in this research is the approximate surface based on the test point data. Theoretical failure surfaces have been proposed by other researches [D1, D3]. In theory, failure surfaces can be created by using fewer test points. In this research, two typical theoretical failure surfaces, Hosford-Coulomb (H-C) failure surface and Basaran failure surface, were evaluated and compared with the approximate test-based failure surface. The two theoretical failure surfaces are shown in figure D-1. Additionally, their cross-sections at Lode parameter = 1.0, 0.0, and -1.0 are compared with the approximate test-based failure surface in figure D-2.

The H-C failure surface was developed by Mohr et al [D1, D2]. The H-C failure criterion was derived by adopting the Hosford equivalent stress into Mohr-Coulomb failure criterion. Then, the H-C failure surface was developed by taking the coordinate transformation and the isotropic hardening law. It has four parameters that can be determined by three test point data, such as uniaxial tension (SG1), plane strain tension (SG11), and pure shear (LR3).

Another theoretical failure surface was proposed by Basaran [D3]. Three bound curves at Lode parameter = 1.0, 0.0, and -1.0 are defined as the reduced form of the Johnson-Cook equation. Then, the Basaran failure surface is generated by quadratic interpolation through three bound curves. It has seven parameters, which can be determined by five test point data, such as uniaxial tensions (SG1 and SG10), plane strain tension (SG11), pure shear (LR3), and biaxial tension (unbacked punch test).

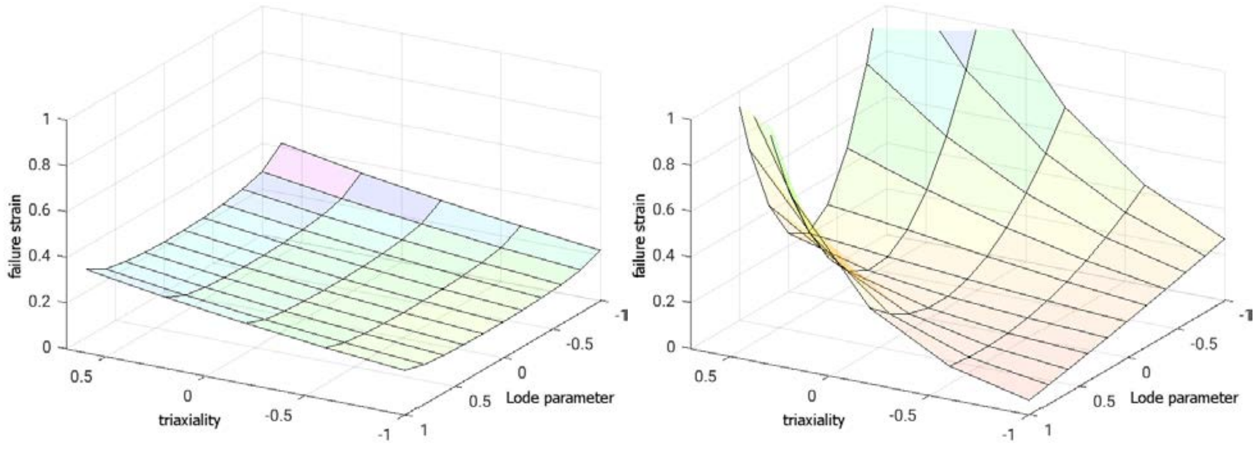

(a) (b)

Figure D-1. Theoretical LCF of *MAT_224: (a) LCF (H-C) and (b) LCF (Basaran)

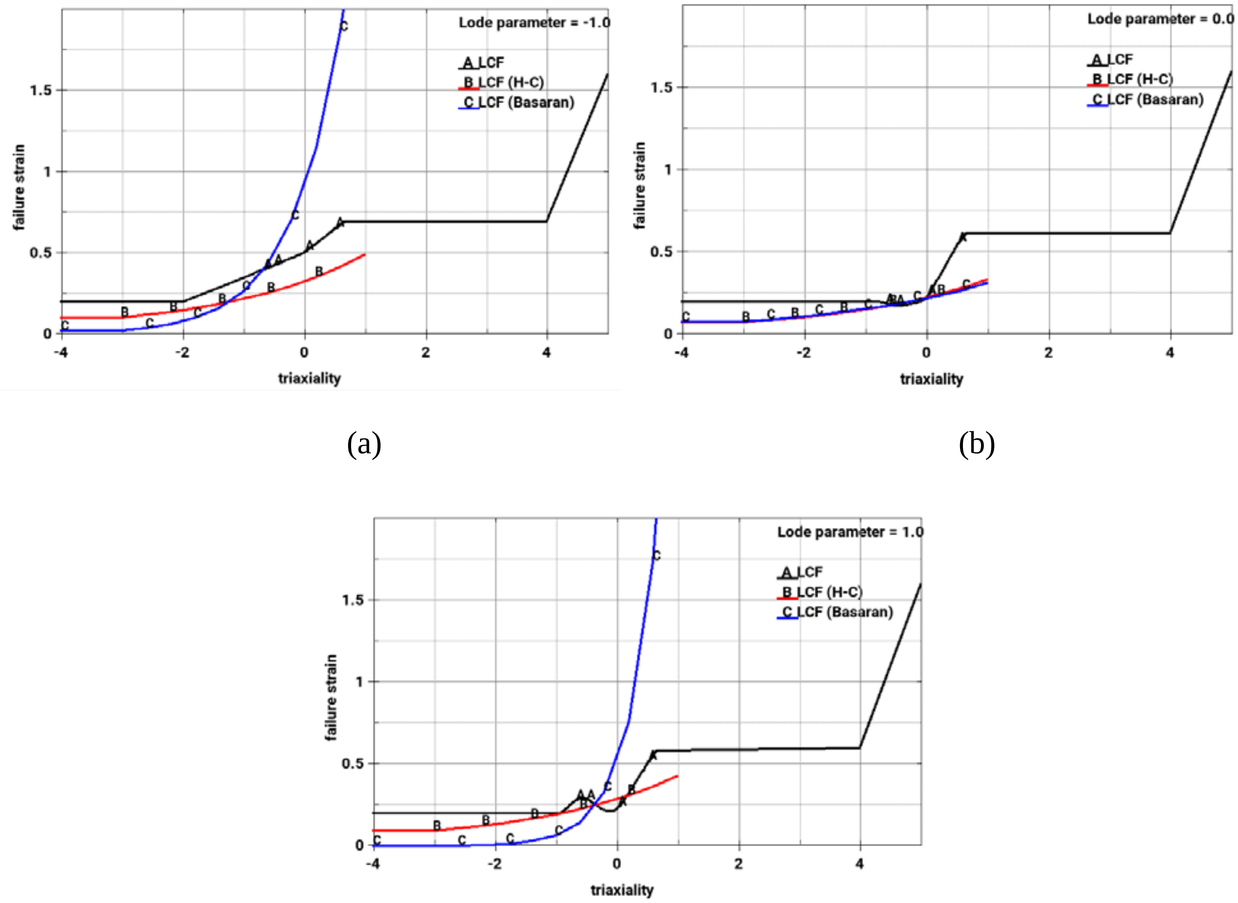

(a)

(b)

(c)

Figure D-2. Comparison of the cross sections of three LCFs of *MAT_224: (a) at Lode parameter = -1.0, (b) at Lode parameter = 0.0, and (c) at Lode parameter = 1.0

The results of the impact simulations using the theoretical failure surfaces are shown in figures D.3–D.4. Only the LCF in *MAT_224 was replaced in the impact simulations, using the baseline (Mesh-3) mesh. Figure D-3(a) shows the results of the sphere impact simulations with the H-C failure surface. It shows a good match in the thin (0.063 inch) plate case, but underestimates the exit velocities of the sphere projectile in the intermediate (0.125 inch) and thick (0.25 inch) plate cases. Figure D-3 (b) shows the results with the Basaran failure surface. It shows a good match in the intermediate (0.125 inch) plate case, but overestimates a bit in the thin (0.063 inch) plate cases and underestimates in the thick (0.25 inch) plate cases.

Figure D-4(a) shows the results of the cylinder impact simulations with the H-C failure surface. It underestimates the exit velocities of the cylinder projectile in all three thickness plate cases. Figure D-4(b) shows the results using the Basaran failure surface. It shows relatively good matches in all three thickness plate cases.

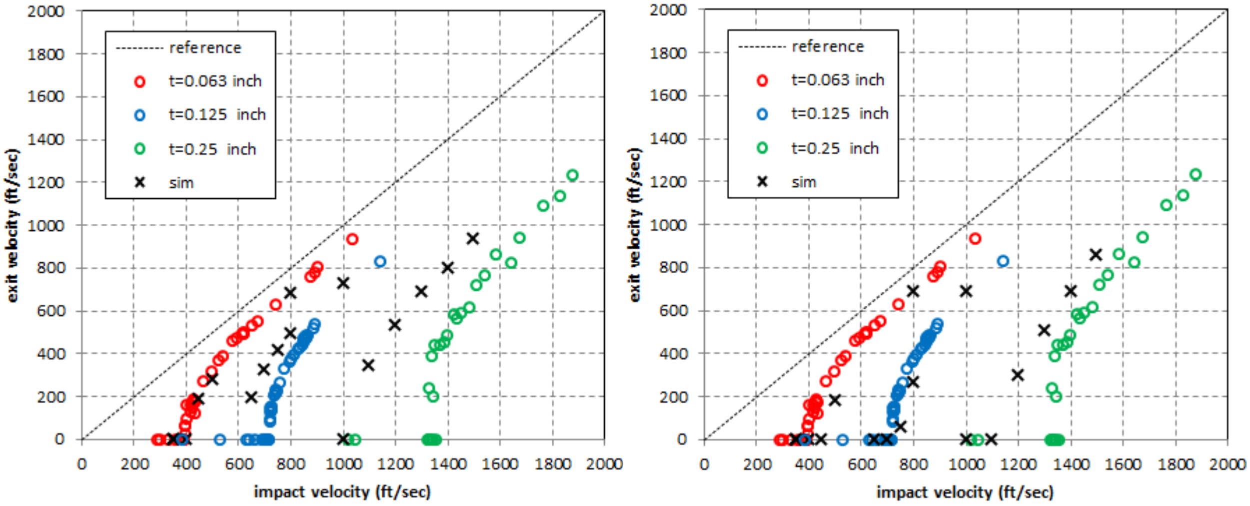

(a) (b)

Figure D-3. Results of ballistic impact tests with the sphere projectile to three different thickness plates of Aluminum 2024 alloy and the results of their simulations using the updated material model of *MAT_224: (a) LCF (H-C) and (b) LCF (Basaran)

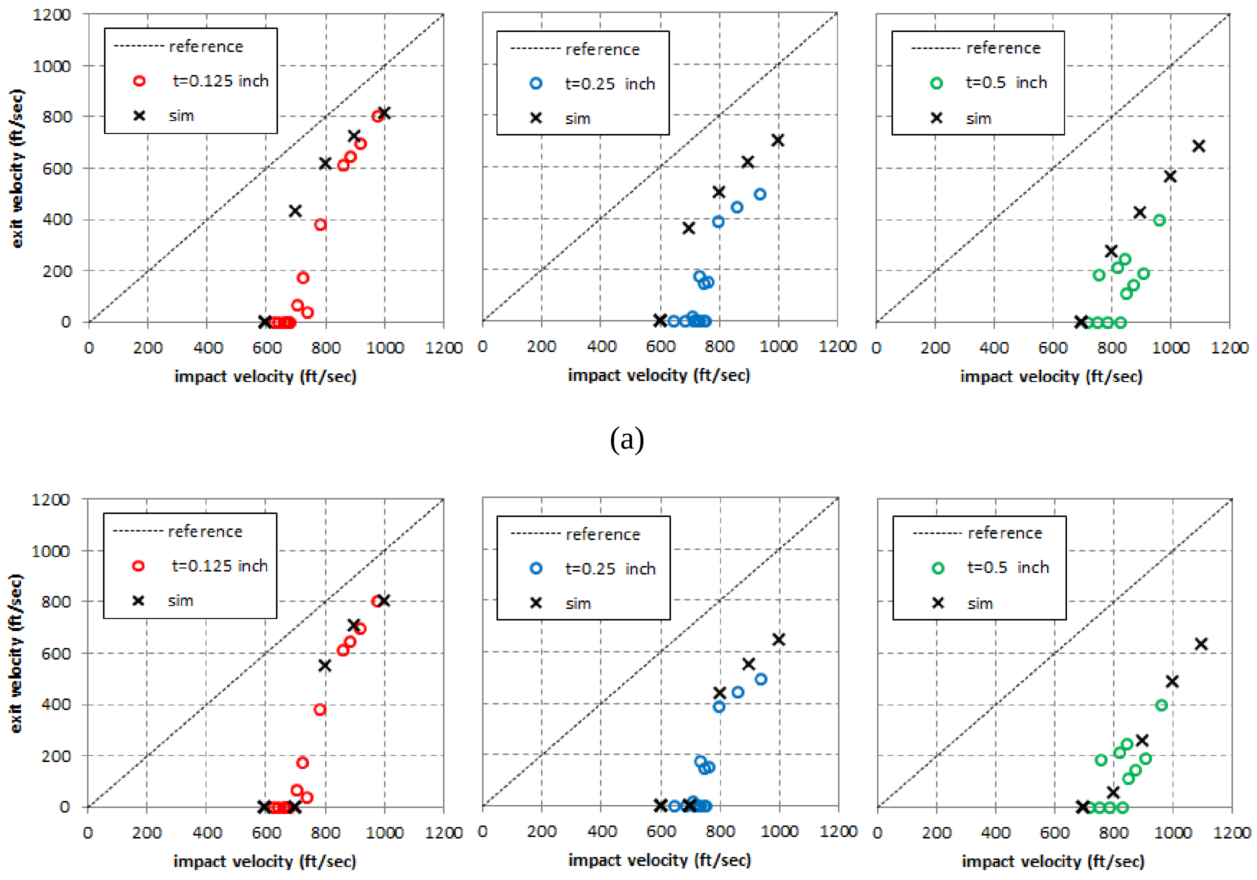

(a)

(b)

Figure D-4. Results of ballistic impact tests with the cylinder projectile to three different thickness plates of Aluminum 2024 alloy and the results of their simulations using the updated material model of *MAT_224: (a) LCF (H-C) and (b) LCF (Basaran)

Figures D.5–D.6 show the failure shapes at the center of the aluminum plate in the simulations, with the two different theoretical failure surfaces. In the sphere impacts shown in figure D-5, the simulation with the LCF (Basaran) shows the larger plug and petals than those in the approximate test-based LCF shown in figure 54, but the LCF (H-C) shows an entirely eroded plug in the thick plate and all broken petals in intermediate plate

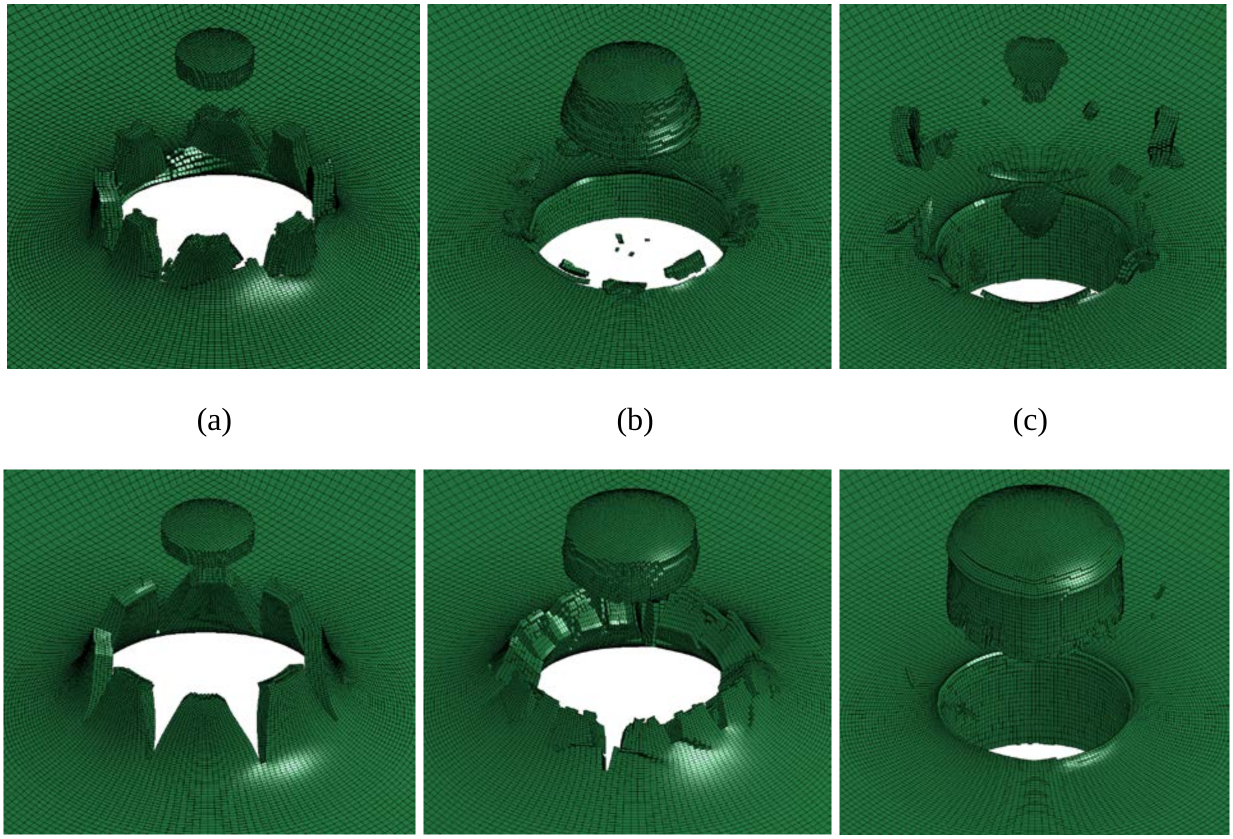

(a) (b) (c)

(d) (e) (f)

Figure D-5. Failure views of the aluminum plate in the sphere impact simulations with the theoretical failure surfaces: (a) LCF (H-C), plate thickness = 0.063 inch and projectile impact speed = 450 ft/sec; (b) LCF (H-C), plate thickness = 0.125 inch and projectile impact speed = 750 ft/sec; (c) LCF (H-C), plate thickness = 0.25 inch and projectile impact speed = 1,400 ft/sec; (d) LCF (Basaran), plate thickness = 0.063 inch and projectile impact speed = 450 ft/sec; (e) LCF (Basaran), plate thickness = 0.125 inch and projectile impact speed = 750 ft/sec; and (f) LCF (Basaran), plate thickness = 0.25 inch and projectile impact speed = 1,400 ft/sec

In the cylinder impact simulation shown in figure D-6, there are some differences in the plug shapes and size compared to the baseline shown in figure 57. Especially, the plug shapes in the intermediate plate using the theoretical failure surfaces in figures D.6(b) and D.6(e) are different from the one in the baseline, which used the approximate test-based failure surface. This is because the lower failure strain curve at Lode parameter = 0.0, shown in figure D-2(b), makes the shear band failure dominant in the intermediate plate.

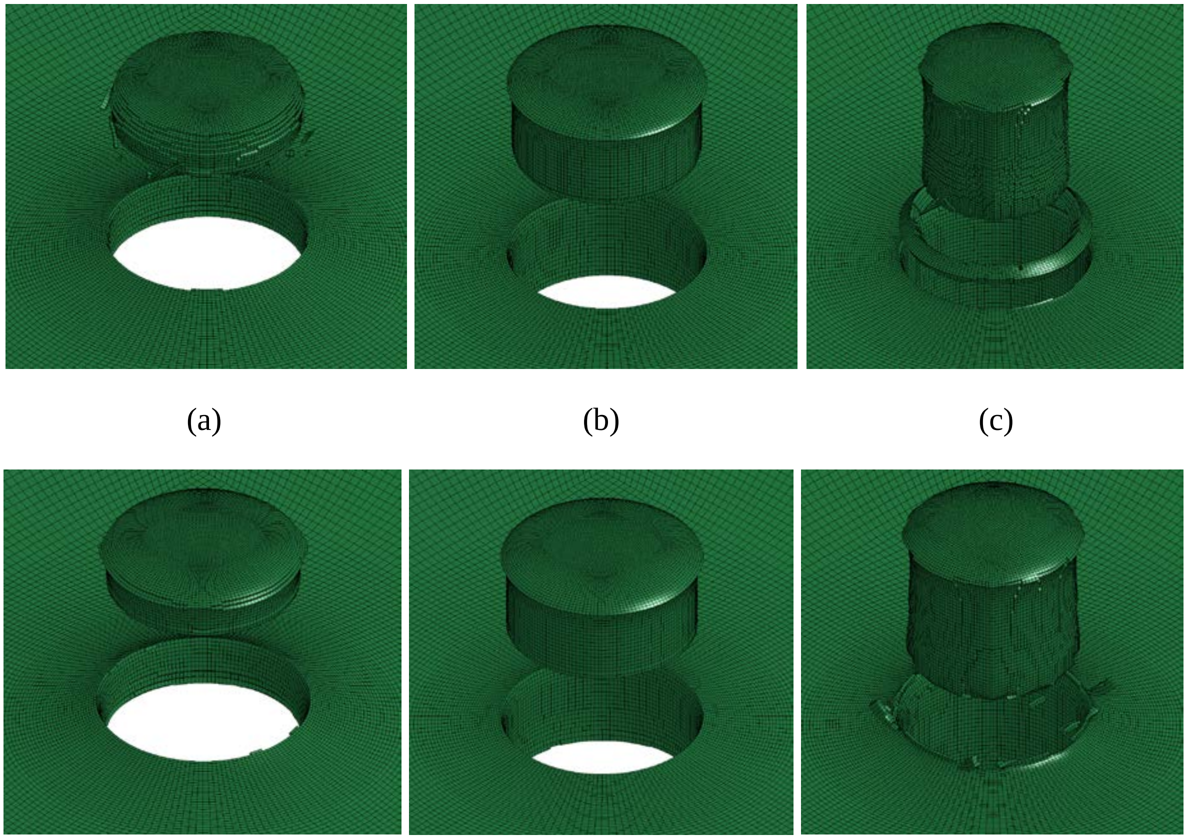

(a) (b) (c)

(d) (e) (f)

Figure D-6. Failure views of the aluminum plate in the cylinder impact simulations with the theoretical failure surfaces: (a) LCF (H-C), plate thickness = 0.125 inch and projectile impact speed = 800 ft/sec; (b) LCF (H-C), plate thickness = 0.25 inch and projectile impact speed = 900 ft/sec; (c) LCF (H-C), plate thickness = 0.5 inch and projectile impact speed = 900 ft/sec; (d) LCF (Basaran), plate thickness = 0.125 inch and projectile impact speed = 800 ft/sec; (e) LCF (Basaran), plate thickness = 0.25 inch and projectile impact speed = 900 ft/sec; and (f) LCF (Basaran), plate thickness = 0.5 inch and projectile impact speed = 900 ft/sec

In summary, the ballistic impact simulations using the H-C failure surface were able to predict one out of six exit velocities, and the simulations using the Basaran failure surface could predict four out of six exit velocities, as shown in table D-1. Using a well-constructed LCF in *MAT_224 is critical to simulate ballistic impact tests accurately. It shows that using more material test point data provides a better-constructed LCF.

Table D-1. Summary of ballistic limit velocities of a projectile with using different LCFs

	Plate thickness (inch)	Ballistic limit velocity (ft/sec)			
		Test	Simulation		
			LCF (Baseline)	LCF (H-C)	LCF (Basaran)
Sphere impact	0.063	391	440	410	475
	0.125	717	710	620	750
	0.25	1,327	1,300	1,050	1,150
Cylinder impact	0.125	710	740	650	700
	0.25	750	850	650	750
	0.5	840	900	750	780

REFERENCES

D1. Roth, C.C., and Mohr, D. (2014). Effect of strain rate on ductile fracture initiation in advanced high strength steel sheets: Experiments and modeling. *International Journal of Plasticity, 56*, 19–44.

D2. Mohr, D., and Marcadet, S.J. (2015). Micromechanically-motivated phenomenological Hosford–Coulomb model for predicting ductile fracture initiation at low stress triaxialities. *International Journal of Solids and Structures*, *67–68*(15), 40–55.

D3. Basaran, M. (2011). *Stress state dependent damage modeling with a focus on the Lode angle influence.* (PhD Dissertation). RWTH Aachen.